UNIVERSITÉ DE MONTRÉAL

EMERGING MICROSTRUCTURED FIBERS FOR LINEAR AND NONLINEAR OPTICAL APPLICATIONS IN THE MID-INFRARED AND TERAHERTZ SPECTRUM

BORA UNG

DÉPARTEMENT DE GÉNIE PHYSIQUE

ÉCOLE POLYTECHNIQUE DE MONTRÉAL

THÈSE PRÉSENTÉE EN VUE DE L'OBTENTION DU DIPLÔME DE

PHILOSOPHIAE DOCTOR

(GÉNIE PHYSIQUE)

MAI 2012

UNIVERSITÉ DE MONTRÉAL

ÉCOLE POLYTECHNIQUE DE MONTRÉAL

Cette thèse intitulée :

EMERGING MICROSTRUCTURED FIBERS FOR LINEAR AND NONLINEAR OPTICAL APPLICATIONS IN THE MID-INFRARED AND TERAHERTZ SPECTRUM

présentée par : UNG Bora

en vue de l'obtention du diplôme de : Philosophiæ Doctor

a été dûment accepté par le jury d'examen constitué de :

M. MEUNIER Michel, Ph.D, président

M. SKOROBOGATIY Maksim A., Ph.D, membre et directeur de recherche

M. AZAÑA José, Ph.D, membre

M. PICHÉ Michel, Ph.D, membre

DÉDICACE

à Marie-Hélène et la famille.

REMERCIEMENTS

J'aimerais tout d'abord remercier mon directeur de thèse Maksim Skorobogatiy qui m'a offert une place au sein d'une équipe de recherche dynamique et m'a poussé à dépasser mes limites.

Aux cotés de tout théoricien se tiennent plusieurs collègues beaucoup plus habiles dans le labo que ce dernier: merci infiniment à Alexandre Dupuis, Anna Mazhorova, Mathieu Rozé, et Hang Qu, ainsi qu'au technicien Francis Boismenu. Merci aussi à Andrey Markov pour son aide avec certaines simulations numériques. Je remercie pour leur aide et les nombreuses interactions constructives mes collègues: Frédéric Désévédavy, Stephan Gorgutsa, Bertrand Gauvreau, Alireza Hassani, Ning Guo, Niyaz Madhar, Yang Liu et Imran Syed. Je remercie le Prof. Markus Walther de la Freiburg University qui nous a assisté dans la caractérisation par champ proche térahertz de certaines fibres optiques, et dans l'interprétation de ces données.

Je remercie également mes amis du Groupe des Couches Minces pour leurs remarques instructives, scientifiques ou amusantes qui ont ponctuées nos discussions du midi.

Une mention très spéciale à mon épouse Marie-Hélène pour sa patience et son support infaillible durant ces belles années, ainsi qu'à mes parents et frères, et ma nouvelle famille Thibault. Vos mots d'encouragement ont été précieux, je vous en suis sincèrement reconnaissant.

Grâce à vous tous, je ressors de mon expérience doctorale bien vivant, plus sage et mature, et plus curieux qu'auparavant.

RÉSUMÉ

Les régions spectrales des ondes térahertz (THz) et de l'infrarouge moyen (mIR) représentent les frontières immédiates nous séparant du but d'exploiter le spectre électromagnétique dans son intégralité pour les applications technologiques du futur.

La bande spectrale de l'infrarouge moyen couvre les longueurs d'ondes entre 2 et 20 microns du spectre infrarouge. Diverses applications tirant profit du mIR sont envisagées dans de nombreux domaines d'intérêts tels: spectroscopie, imagerie infrarouge, chirurgie laser et bio-diagnostic. Malgré les nombreux avantages immédiats pouvant être tirés des applications du spectre mIR, sa pleine exploitation demeure à ce jour limitée en raison, d'une part, par le manque de sources laser mIR couvrant une large portion de ce domaine spectral. En effet, la majorité des sources cohérentes mIR actuellement disponibles (oscillateurs paramétriques optiques, lasers à cascades quantiques, lasers à électrons libres) sont discrètes et restreignent ainsi les applications à une seule longueur d'onde spécifique à la fois. Il existe actuellement une forte demande au sein de l'industrie et la communauté scientifique pour la création d'une source lumineuse cohérente à large bande spectrale émettant dans le mIR, et sous une forme compacte.

Le premier sujet de recherche de cette thèse se rapporte au design de nouvelles *fibres hautement nonlinéaires* (FHNL) pour leur utilisation dans la génération de lumière mIR (e.g. génération d'un supercontinuum), et au sein de dispositifs de conversion en longueurs d'onde mIR basés sur des effets optiques nonlinéaires. À cet effet, l'efficacité de génération/conversion de la lumière mIR dépend intimement du contrôle des propriétés optiques linéaires et nonlinéaires du guide d'onde employé dans le système. Au cours de mes travaux, j'ai étudié différents designs de guides d'ondes microstructurés (ou nanostructurés) hautement nonlinéaires et possédant un potentiel pour des applications à impact concret. Plus particulièrement, nous avons démontré deux nouveaux types de FHNL: la *fibre optique nanostructurée hybride en chalcogénures-métal* qui supporte un mode plasmonique permettant un confinement du champ à des dimensions profondément sous-longueur d'ondes, ainsi que la *fibre microporeuse en verres de chalcogénures* offrant des possibilités étendues pour le contrôle de la dispersion chromatique dans les fibres optiques nonlinéaires. Par ailleurs, des simulations numériques basées sur l'équation de Schrodinger nonlinéaire, et assumant cette dernière FHNL comme guide d'onde, ont été effectuées et ont démontré leur potentiel pour la génération d'un large supercontinuum mIR dans

une fibre microporeuse en chalcogénures excitée à de larges longueur d'ondes (i.e. 10.5 μm) par des impulsions picosecondes.

De plus, une étude sur la fibre optique nanostructurée hybride chalcogénures-métal a démontré sa capacité à confiner un mode guidé à des dimensions sous-longueur d'ondes, en deçà des limites classiques de diffraction de la lumière. Cet exploit est rendu possible en tirant profit des plasmons polaritons de surface guidés par la matrice de nanofils métalliques insérés dans le coeur de la FHNL. Ce confinement modal sous-longueur d'onde se traduit par une exaltation considérable du coefficient nonlinéaire qui constitue la pièce maîtresse dans la réalisation d'une source mIR large bande à fibre via la génération d'un supercontinuum, ainsi que pour la conception de composants photoniques intégrés hautement nonlinéaires.

D'autre part, les ondes térahertz (comprenant les longueurs d'ondes entre 80 et 3000 μm) procurent une radiation à basse énergie non-ionisante et faiblement pénétrante, possédant un immense potentiel pour des applications en détection non-destructive et en imagerie dans plusieurs domaines dont la médecine et en défense. Toutefois, la majorité des matériaux testés à ce jour sont soit opaques ou très atténuants à l'intérieur du spectre THz. Par conséquent, un des défis technologiques important à l'heure actuelle en science du térahertz, consiste au développement de guides d'ondes THz à faibles pertes. Ce deuxième sujet de recherche fut exploré dans cette thèse: nous avons effectué le design, la fabrication et la caractérisation de plusieurs types de guides d'ondes THz basés sur des matériaux en polymères. Les résultats obtenus ont démontré un impact pratique dans l'acheminement efficace de signaux THz. A cet égard, notons que les fibres optiques à base de polymères offrent une plate-forme versatile pour le développement de guides d'ondes térahertz. Les principaux avantages des polymères inclus: l'abondance et le bas coût des différentes compositions chimiques offrant des pertes optiques relativement basses; la facilité à concevoir les préformes des fibres microstructurées via des techniques conventionnelles de moulage, fraisage et par empillement; et finalement, la simplicité et la commodité de la méthode de fabrication des fibres par étirage à des températures de mise en forme relativement basses.

Nous avons étudié les performances de fibres de Bragg à coeur creux fabriquées à partir d'une matrice de polymère dopée (à différents degrés de dopage) avec des microparticules de titane possédant un fort indice de réfraction et de fortes pertes optiques. Notre analyse a révélé

que les hautes pertes par absorption générées par une haute concentration de dopants peuvent effectivement annihiler le mécanisme de guidage par bande photonique interdite des fibres de Bragg. Nous en déduisons donc qu'un *compromis* entre le fort contraste d'indice de réfraction (le "bénéfice") et les fortes pertes optiques ("l'inconvénient") qui subsistent à hautes concentrations de dopants, est nécessaire. Cette découverte est particulièrement utile au design de composants THz basés sur le principe de bandes photoniques interdites et fabriqués avec des matériaux composites en polymères.

Plusieurs designs récents de guides d'ondes térahertz ont opté pour l'approche d'une réduction de la fraction de puissance guidée dans les sections de matériaux à grandes pertes, dans le but de mitiger les pertes de guidage des signaux THz. Toutefois, les champs hautement délocalisés qui émanent de la plupart de ces designs "poreux" entravent leur adoption en pratique. La raison étant qu'un champ modal délocalisé s'accompagne généralement d'une sensibilité modale accrue à toute perturbation dans le milieu ambiant, incluant la simple manipulation des fibres par un utilisateur. Une solution décrite dans cette thèse consiste en une *fibre diélectrique à coeur suspendu*, qui procure une propagation guidée dans un coeur complètement cloisonné à l'intérieur d'un tube de polymère ayant la double fonction d'isoler le mode guidé des perturbations externes, et de protéger la surface du coeur de l'accumulation de contaminants indésirables tels des poussières. Des mesures expérimentales du profil du mode de sortie, tirées d'imagerie THz par champ-proche (et confirmé avec des simulations par éléments finis), indiquent que la fibre diélectrique à coeur suspendu permet un guidage "monomode effectif" à l'intérieur de sa fenêtre de transmission principale. Grâce à la grande fraction de puissance guidée dans la section de gaine poreuse entourant le coeur suspendu, des pertes en propagation aussi basses que 0.02 cm^{-1} ont été mesurées expérimentalement avec une telle fibre fabriquée dans nos labs.

Finalement, les limites physiques et les seuils de performance des différents designs de fibres proposés pour le mIR et le THz sont discutés, et des directions de recherches futures sont suggérées afin de résoudre ou réduire certaines de ces limites, avec l'intention de faire progresser le savoir sur les sujets traités dans cette thèse.

ABSTRACT

The terahertz (THz) and middle-infrared spectrum (mIR) represent the next frontiers in the goal of harnessing the whole electromagnetic spectrum in future technological applications.

The middle-infrared spectral band covers the wavelengths between 2 and 20 microns in the infrared. A myriad of applications that take advantage of the mIR spectrum are envisioned in several fields of interest such as: spectroscopy, infrared imagery, laser surgery and bio-diagnostic. Despite the numerous immediate benefits that may be reaped from applications of mIR technology, its full exploitation remains limited by the lack of bright and coherent optical sources of mIR light. In fact, the majority of current mIR coherent sources (optical parametric oscillators, quantum cascade lasers, free electron lasers) are discrete and thus restrict applications to a single specific wavelength at a time. Thus there is presently a strong demand within the industrial and academic communities for the creation of a broad bandwidth coherent mIR light source in a compact form factor.

The first research topic of my thesis was to design novel *highly-nonlinear fibers* (HNLFs) to be used in mIR light generation (e.g. supercontinuum generation) and mIR wavelength conversion schemes based on nonlinear optical effects. The efficiency of mIR light generation/conversion depends intimately on the precise control of the linear and nonlinear optical properties of the waveguide used in the optical setup. During the course of this work, we investigated various designs of both microstructured and nanostructured highly-nonlinear waveguides with great potential for end-user applications. In particular, we demonstrated two novel types of HNLFs: the *hybrid chalcogenide-metal nanostructured optical fiber* that supports a plasmonic mode enabling deep-subwavelength field confinement capabilities, and the *chalcogenide microporous fiber* that provides extensive design freedom for engineering the chromatic dispersion of nonlinear fibers. Furthermore, simulations of the nonlinear Schrodinger equation, assuming the latter type of HLNF, were performed and showed the potential for generating a broad mIR supercontinuum inside a chalcogenide microporous fiber seeded at long wavelengths (i.e. 10.5 μm) using short picosecond pulses.

Furthermore, the study of the hybrid chalcogenide-metal nanostructured optical fiber demonstrated subwavelength-size optical mode confinement beyond the classical diffraction limit. This feat was made possible by harnessing surface plasmon polaritons guided by the

metallic nanowire arrays integrated within the core of the HNLF. This subwavelength-size modal confinement translates into an extremely large nonlinear optical enhancement that provides the key component towards the realisation of broadband mIR sources via supercontinuum generation, and highly-nonlinear and highly-integrated photonic components in general.

Terahertz waves (comprising wavelengths between 80 and 3000 μm), on the other hand, provide a low-energy, non-ionizing and slightly penetrating radiation with immense potential for non-destructive sensing and imaging applications in medicine and security, among others. However most materials are opaque or very absorbant in the THz range. Therefore an important technological challenge resides in guiding THz waves to a remote location with low signal losses. This second topic of research was studied in my thesis: we designed, fabricated and characterized various types of THz waveguides based on polymer materials, and which demonstrated a high practical impact for the efficient delivery of terahertz radiation. In this regard, polymer optical fibers provide a versatile platform for guiding THz radiation. The key benefits of this technology include: the abundance of the low-cost and relatively low-absorption-loss polymers; the ease of fiber preform fabrication by molding, drilling, stacking and the use of other standard polymer processing techniques; and finally the convenience of simple fabrication method by fiber drawing at relatively low-forming temperatures.

We studied the performance of *hollow-core Bragg fibers* fabricated using a host polymer matrix with varying doping levels of high-index and high-loss titania microparticles. Our analysis revealed that the large absorption losses induced by the high concentration of dopants can effectively destroy the photonic bandgap guiding mechanism of Bragg fibers such that an appropriate trade-off between the high-refractive-index contrast and the large associated material losses is necessary. This finding is relevant to the design of THz optical components based on polymeric composite materials.

Several recent designs of terahertz waveguides have taken the approach of reducing the fraction of guided optical power in lossy materials regions so as to minimize the modal propagation losses of the THz signal. However the highly-delocalized modal fields in many of these designs hinders their practical use for THz waveguiding, because of their significant modal sensibility to external perturbations like simple hand manipulation of the fiber. A solution was proposed in this thesis via the *suspended core dielectric fiber* which enables a fully-encapsulated

core-guided modal propagation inside an outer polymer tube cladding that provides protection against external pertubations and the accumulation of surface contaminants on the suspended core's surface. Experimental measurements of the output mode profiles, performed with THz near-field imaging (and confirmed by finite-element simulations), have indicated that the suspended core dielectric fiber guides in an effectively single-mode regime inside its main low-loss window. Owing to the large fraction of modal power that is guided in the holey cladding, experimental fiber propagation losses as low as 0.02 cm^{-1} have been demonstrated with the fabricated fiber.

Finally, the performance and physical limitations of the proposed designs of fibers for the mIR and THz spectrum are discussed, and potential future research directions are suggested to solve or alleviate some of these limitations and gain new grounds on the subjects covered therein.

TABLE OF CONTENTS

DÉDICACE III

REMERCIEMENTS IV

RÉSUMÉ V

ABSTRACT VIII

TABLE OF CONTENTS XI

LIST OF FIGURES XIV

LIST OF APPENDICES XXI

LIST OF SYMBOLS AND ABBREVIATIONS XXII

INTRODUCTION 1

CHAPTER 1 : LITERATURE REVIEW 4

1.1 Nonlinear microstructured optical fibers for the middle-infrared 4

1.2 Microstructured optical fibers for terahertz waveguiding 14

CHAPTER 2 : EMERGING MICROSTRUCTURED CHALCOGENIDE FIBERS FOR LINEAR AND NONLINEAR OPTICAL APPLICATIONS IN THE MIDDLE-INFRARED SPECTRUM 23

2.1 Chalcogenide microporous fibers for linear and nonlinear applications in the mid-infrared 24

2.1.1 Introduction 24

2.1.2 Optical properties of the chosen nonlinear glass 26

2.1.3 Geometry of proposed design 26

2.1.4 Results and discussion of the finite-element method simulations 28

2.1.5 Simulation of the nonlinear Schrodinger equation for pulse propagation in nonlinear optical media 32

2.1.6 Simulations of supercontinuum generation 34

2.1.7 Conclusions 36

2.2 Extreme nonlinear optical enhancement in chalcogenide glass fibers with deep-subwavelength metallic nanowires 37

2.2.1 Introduction 37

2.2.2 Motivations and geometry of proposed design 37

2.2.3 Simulations of the subwavelength field confinement and the extreme nonlinear optical enhancement 41

2.2.4 Characterization of the modal propagation losses and discussion 42

2.2.5 Conclusions 43

CHAPTER 3 : EMERGING MICROSTRUCTURED POLYMER FIBERS FOR TERAHERTZ WAVEGUIDING 45

3.1 High-refractive-index composite materials for terahertz waveguides: trade-off between index contrast and absorption loss 45

3.1.1 Introduction 45

3.1.2 Geometry of the hollow-core Bragg fibers 46

3.1.3 Optical characterization of the titania-doped polymer composites 47

3.1.4 Vectorial simulations of the modal properties in doped Bragg fibers 49

3.1.5 Discussion on the trade-off between index contrast and absorption losses in doped Bragg fibers 50

3.1.6 Conclusions 54

3.2 Suspended core subwavelength fibers: towards practical designs for low-loss terahertz guidance 55

3.2.1 Introduction 55

3.2.2 Geometry of proposed design 55

3.2.3 Optical characterization of the polyethylene polymer, and fabrication of the suspended core dielectric fibers 56

3.2.4 Terahertz near-field imaging setup for the characterization of the modal properties in the suspended core dielectric fibers 57

3.2.5 Comparison between the experiments and simulations of the output modal field distributions 58

3.2.6 Fiber output transmission and propagation losses: results and discussions 63

3.2.7 Conclusions 68

CHAPTER 4 : GENERAL DISCUSSION, CONCLUSIONS AND PERSPECTIVES 69

4.1 Nonlinear emerging microstructured fibers for the middle-infrared 69

4.2 Emerging microstructured fibers for terahertz waveguiding 73

REFERENCES 78

APPENDICES 105

LIST OF FIGURES

Figure 1.1 Cross-sections of (a) conventional step-index fiber (the core has a slightly higher refractive index than the cladding), and of two specific examples of emerging microstructured fibers: (b) a photonic crystal fiber, and (c) a suspended small core "wagon-wheel" fiber. 2

Figure 1.2 (a) Multiphonon absorption limits, and (b) absorption loss curves showing the multiphonon edge for various types of glasses. Reproduced from [14] with permission of Taylor & Francis Group LLC; permission conveyed through Copyright Clearance Center Inc. 5

Figure 1.3 Variation of the group velocity chromatic dispersion (solid and long-dash lines) of plane waves propagating in bulk fused silica (data extracted from Chapter 1.2.3 in [4]).....11

Figure 1.4 (a) Example of a typical open-cage fitted with a terahertz scanner for stand-off full-body THz imaging, and (b) false-color representation of the extracted THz signal absorption from a full-body THz scan. Images obtained from [116]. 15

Figure 1.5 (a) Refractive index and (b) bulk absorption coefficient in (cm^{-1}) of common polymers used in the fabrication of THz waveguides. Legend: low-density polyethylene (LDPE), cyclic olefin copolymer (TOPAS®), high-density polyethylene (HDPE), Poly-tetrafluoroethylene (PTFE) a.k.a Teflon®, polycarbonate (PC), polymethyl-methacrylate (PMMA), polyimide (Kapton®), polystyrene (PS), Polypropylene (PP). Data compiled from references [122-124]. 16

Figure 1.6 (a) Schematic of the cross-section of a porous fiber with N = 3 layers of holes. (b) Fundamental HE_{11} mode S_z-profile at 1 THz frequency in a subwavelength porous core PE fiber (d_{fiber} = 120 μm, d_{hole} = 9 μm), and (c) in a subwavelength solid core PE fiber (d_{fiber} = 120 μm). Calculations performed using the full-vector finite-element method.....17

Figure 1.7 (a) Schematic of hollow Bragg fiber with N = 5 bilayers of high-index layers (dark fringes) and low-index layers (pale fringes). (b) Fabricated Bragg fiber with high-index TiO_2 doped layers and low-index PE layers. (c) Fabricated Bragg fiber with high-index PE layers separated by PMMA particles from the low-index air layers. (d) Fundamental HE_{11} mode profile at 1 THz inside the TiO_2-doped Bragg fiber of sub-figure (b) with d_{core} =6.63 mm, d_H

=135 μm, and d_L =100 μm. Sub-figures (b) and (c) are reprinted from [151] and [152] respectively, with permission from The Optical Society of America. 21

Figure 2.1 Total chromatic dispersion (D) in sulfide As_2S_3-glass suspended small-core fibers with varying core sizes. The strong *anomalous* waveguide dispersion (D_{wvg}) enables to partly compensate for the *normal* dispersion of the material (D_{mat}) thus allowing to blue-shift the zero-dispersion wavelength of the waveguide from that of the material dispersion. Reprinted from [93] with permission from The Optical Society of America. 25

Figure 2.2 Refractive index (solid red line) and absorption coefficient (dotted blue line) of bulk selenide (As_2Se_3) glass as a function of excitation wavelength. The material zero-dispersion wavelength (ZDM) is located at 7.225 μm. Reprinted from [99] with permission from The Optical Society of America. 26

Figure 2.3 (a) Refractive index distribution (red: As_2Se_3-glass, blue: air) in a N=4 ($\Lambda = 0.50$ μm, $d_{hole} = 0.42$ μm) chalcogenide microporous fiber, and (b) S_z-power distribution (in a.u.) of the fundamental HE_{11} mode at the 10.5 μm input wavelength. Reprinted from [99] with permission from The Optical Society of America. 27

Figure 2.4 (a) Cross-sectional density f_m of solid material in N=4 layers microporous fiber and (b) fraction of modal absorption f_α over bulk As_2Se_3 absorption at λ=10.5 μm, as a function of parameters (Λ, d_{hole}). The dotted line identifies the regions of f_α = 0.5 (Reprinted from [99]). 28

Figure 2.5 (a) Real effective refractive index and (b) effective mode area of the fundamental mode in N = 4 layers As_2Se_3 microporous fiber at λ = 10.5 μm, as a function of parameters (Λ, d_{hole}). Reprinted from [99] with permission from The Optical Society of America. 29

Figure 2.6 (a) Dispersion parameter (D) and (b) dispersion slope ($dD/d\lambda$) in N = 4 layers As_2Se_3 microporous fiber at λ = 10.5 μm, as a function of parameters (Λ, d_{hole}). Reprinted from [99]. 30

Figure 2.7 (a) Chromatic dispersion curves ($ps/(km \cdot nm)$) showing near-zero and flattened dispersion at λ=10.5 μm for parameters (a) (Λ=0.50, d_{hole}=0.38)μm, and (b) Λ=0.70, d_{hole}=0.62)μm. The blue curve plots the As_2Se_3-glass material dispersion. Reprinted from [99]. 30

Figure 2.8 Contribution to the nonlinear parameter γ ($W^{-1}m^{-1}$) due to (a) As_2Se_3 glass, and (b) Argon gas-filled holes at λ=10.5 μm as a function of (Λ, d_{hole}) for a N = 4 layers microporous fiber. Gas nonlinearities are multiplied by a factor 10^6, for scaling reasons. Reprinted from [99].....31

Figure 2.9 (a) Raman response function $h_R(t)$ of bulk As_2Se_3 glass, and (b) the corresponding Raman gain spectrum ($g_R(\Delta\omega)$) measured at pump wavelength λ=1.54 μm. Adapted from [99]. 33

Figure 2.10 Output supercontinuum spectra calculated via SSFM in a microporous fiber with parameters (Λ=0.40, d_{hole}=0.24)μm, L=10 cm and for (a) E_0=0.9 nJ fixed seed energy with varying FWHM pulse durations (0.1, 1, 10) ps, and (b) for fixed pulse duration $T_{FWHM} = 1$ ps and varying seed energies (0.2, 2.0, 5.0) nJ. The peak power (P_1) of the first ejected fundamental soliton created by the fission of the N_{sol}-th order soliton, is shown alongside its corresponding curve. Reprinted from [99] with permission from The Optical Society of America. 35

Figure 2.11 Micrographs of the cross-sections of (a) a chalcogenide Te-As-Se glass photonic crystal fiber with structural parameters (Λ=13.77, d_{hole}=6.14)μm (image adapted from [39]), and (b) a chalcogenide $Sb_{20}S_{65}Ge_{15}$ glass photonic crystal fiber with structural parameters (Λ=11.1, d_{hole}=4.7)μm (image adapted from [46]). We note the small empty interstices between the holes. Both images reprinted with permission from The Optical Society of America. 38

Figure 2.12 (a) Schematic of a gold bowtie nanoantenna on top of a transparent PMMA substrate (black arrows denote fluorescent molecules in suspension). (b) Vectorial finite-difference time-domain calculation of the local intensity enhancement at λ=780 nm. Adapted by permission from Macmillan Publishers Ltd: Nature Photonics (Ref.[200]), copyright (2009). 38

Figure 2.13 (a) Triangular lattice configuration of overlapping rods and small interstices with (b) a close-up view of the unit-cell geometry along with the relevant structural parameters. (c) S_z-power flux distribution of the fundamental plasmonic mode in the chalcometallic nanostructured fiber (r_{fiber} = 0.450 μm, f_δ = 0.03) at λ=3.0 μm, and (d) close-up view of a

bowtie pair of nanowires showing the enhanced local fields in a.u. (arrows denote the vector *E*-fields). Reprinted from [100] with permission from The Optical Society of America. 39

Figure 2.14 (a) Triangular lattice configuration of three tangent circular rods of identical radii (r_{rod}) and (b) a close-up view of the enclosed deltoid-shaped nanowire, along with the inscribed circle of radius (r_{del}).....40

Figure 2.15 (a) Optical nonlinearity (γ) and (b) effective mode area (A_{eff}) of a bare chalcogenide nanowire and a hybrid chalco-metallic NOF at λ=3.0 μm as a function of the fiber radius. Reprinted from [100] with permission from The Optical Society of America. 41

Figure 2.16 (a) Real effective refractive index (n_{eff}) and (b) effective propagation length (L_{eff}) of a bare chalcogenide nanowire and a hybrid chalco-metallic nanofiber at λ=3.0 μm as a function of the fiber radius. Inset in (a): fraction of power guided inside metallic regions for the chalco-metallic fiber (solid curve) and inside chalcogenide glass, for the nanowire (dashed curve). The n_{eff} and L_{eff} of a classical SPP on the gold–As_2Se_3 planar interface is also shown (green dot–dashed curve) for reference in (a) and (b) respectively. Reprinted from [100] with permission.....42

Figure 3.1 Hollow-core Bragg fiber with the reflector made of alternating hRI TiO_2-doped PE layers and low-index pure PE layers. (a) Structure with 14 bilayers used in the T-matrix calcula- tions. (b) Bragg fiber with five bilayers fabricated using a combination of film extrusion, hot pressing, and subsequent coiling. Reprinted from [151] with permission from The Optical Society of America.....46

Figure 3.2 Refractive index of a PE-based polymer compound as a function of weight concentration of TiO_2 particles: Bruggeman model fit (solid curve) [see Eq. (3.1)] and measurements at 1 THz frequency (circles). Inset: THz-TDS measurements of the refractive index for pure PE (dashed curve), 40 wt.% (dotted curve), and 80 wt.% (solid curve) TiO_2 doping. Reprinted from [151] with permission from The Optical Society of America. 47

Figure 3.3 Power absorption loss of the doped PE-based polymer compound as a function of frequency (THz) for various levels of TiO_2 doping concentrations: 0 wt.% (pure PE), 40 wt.%, and 80 wt.%. Squares, circles, and triangles denote THz-TDS measurements, while the dashed, dotted and solid curves represent the corresponding polynomial fits [see Eq. (3.2)]. Reprinted from [151] with permission from The Optical Society of America. 48

Figure 3.4 Fundamental mode loss in doped-PE/PE hollow-core polymer Bragg fibers (14 bilayers) as a function of input frequency and for various levels of fractional nominal loss (f_{loss}) inside the dielectric layers. Inset: calculated fundamental mode power profile at 1 THz. Reprinted from [151] with permission from The Optical Society of America. 49

Figure 3.5 Fundamental mode loss (dB/m) as a function of TiO_2 doping concentration of high-index layers and frequency, for an ideal Bragg fiber (five bilayers) whose reflector layer thicknesses are tuned to obey the quarter-wave condition near the center frequency 1 THz. Reprinted from [151] with permission from The Optical Society of America. 52

Figure 3.6 Fundamental mode loss (dB/m) in 80 wt.% doped Bragg fiber (five bilayers) computed by the T-matrix method (dashed curve) with perfect circular symmetry, and via the FEM (dotted curve) with the spiral shape defect (shown inset). THz-TDS measurements of total attenuation (open circles), and theoretical calculations including coupling losses and intermodal interference effects (solid curve). Reprinted from [151] with permission from The Optical Society of America. 53

Figure 3.7 (a) Cross-section of the suspended solid core fiber (OD = 5.1 mm), and (b) close-up view of the suspended solid core region ($d_{core} \sim 150$ μm). (c) Cross-section of the suspended porous core fiber (OD = 3 mm), and (d) close-up view of the suspended large porous core (d_{core} = 900 μm). Reprinted from [139] with permission from The Optical Society of America. 55

Figure 3.8 (a) Refractive index and (b) bulk material losses of polyethylene (PE) in the frequency range 0.10 – 1 THz as measured by THz-TDS. The inset picture in Fig.(a) shows the PE slab used for the measurements. Reprinted from [139] with permission from The Optical Society of America. 56

Figure 3.9 Schematic of the THz near-field microscopy setup used for fiber mode profiling. ...58

Figure 3.10 Near-field microscopy images (top row) and corresponding simulations (bottom row) of the output $|E_x|$-field profile of the suspended small solid core fiber at 0.16, 0.30 and 0.48 THz. Reprinted from [139] with permission from The Optical Society of America. 59

Figure 3.11 Near-field microscopy images (top row) and corresponding simulations (bottom row) of the output $|E_x|$-field profile of the suspended large porous core fiber at 0.10, 0.16 and 0.30 THz. Reprinted from [139] with permission from The Optical Society of America. 60

Figure 3.12 Gaussian beam waist parameter (σ) as a function of input wavelength, as measured with the THz near-field microscopy setup (dots), and modeled by a linear fit (solid line). Reprinted from [139] with permission from The Optical Society of America. 62

Figure 3.13 Transmitted $|E_x|$-field as measured by the near-field THz-TDS probe between 0.01 and 0.80 THz for various lengths of (a) suspended small solid core fiber, and (b) suspended large porous core fiber. Corresponding numerical simulations of the amplitude transmission through the (c) suspended solid core fiber, and (d) the suspended porous core fiber. Reprinted from [139].....64

Figure 3.14 (a) Power propagation losses (measured by the cutback method) of the suspended solid core fiber, and of the (b) suspended porous core fiber, as a function of frequency. Dashed line corresponds to quadratic fit of the bulk material losses. Reprinted from [139] with permission from The Optical Society of America. 66

Figure 3.15 Near-field microscopy images of the output $|E_x|$-field profile at (a) 0.67 THz and (b) 0.72 THz, that indicate the presence of a higher-order guided mode in the suspended small solid core fiber.....67

Figure 4.1 Schematic of the tapering of a multimoded nonlinear optical fiber into a single-mode fiber (along with enhanced optical nonlinearities inside the tapered section). 70

Figure 4.2 Finite element method simulations of optical heat generation at a silver nanowire junction during the nanowelding process in the 2 nm gap between silver nanowires with a 100 nm diameter and circular cross-section. The illumination source is a plane wave with a wavelength of 800 nm, incident from the top and polarized perpendicular to the top nanowire. Reprinted by permission from Macmillan Publishers Ltd: Nature Materials (Ref.[227]), copyright (2012).....72

Figure B. 1 Convergence study for the fundamental mode guided in a specific microporous chalcogenide fiber geometry at $\lambda = 10.5\ \mu m$ and for polynomial order $n = 2$. FEM calculations conducted with RSoft FemSIM® software. 108

Figure B. 2 Triangular mesh generated by COMSOL® at different zoom scales, starting from farthest (a) to closest (d), for modelling a hybrid chalco-metallic nanofiber [see Chapter 2.2]. 109

Figure B. 3 (a) Partial zoom image of the mesh generated by COMSOL® and (b) corresponding partial image of the fundamental mode in the hybrid chalco-metallic nanofiber at $\lambda = 3.0\ \mu m$ and for polynomial order $n = 3$. 110

Figure C. 1 Schematic of the procedural implementation of the symmetrized split-step Fourier method. 112

Figure D. 1 Schematic of the cutback technique procedure for measuring the optical propagation losses in an optical fiber. 114

LIST OF APPENDICES

APPENDIX A : LIST OF PUBLICATIONS 105

APPENDIX B : PRINCIPLES OF THE FINITE-ELEMENT METHOD 107

APPENDIX C : PRINCIPLES OF THE SPLIT-STEP FOURIER METHOD 111

APPENDIX D : ERROR ANALYSIS OF THE CUTBACK TECHNIQUE 114

LIST OF SYMBOLS AND ABBREVIATIONS

α	Absorption loss coefficient
A_{eff}	Effective mode area
β	Mode propagation constant
β_2	Group velocity dispersion coefficient
c	Speed of light in vacuum
D	Dispersion parameter
ε	Dielectric constant (relative permittivity) of a material
γ	Nonlinear parameter (or nonlinear optical coefficient, or effective nonlinearity)
$\chi^{(3)}$	Third-order (nonlinear) susceptibility
λ	Wavelength of light
Λ	Caracteristic length scale (i.e. period) of a periodic pattern
L	Fiber length
L_{eff}	Effective fiber length
L_{D}	Dispersion length
L_{NL}	Nonlinear length
n	(Linear) index of refraction of a material
n_2	Nonlinear index of refraction of a material
n_{eff}	Effective index of refraction of a guided mode
N_{sol}	Soliton order
ν	Frequency of light
ϕ_{NL}	Nonlinear phase shift

v_g	Group velocity
v_p	Phase velocity
ω	Angular frequency of light
ARROW	Anti-resonant reflecting optical waveguide
ASE	Anomalous skin effect
CVD	Chemical vapour deposition
CW	Continuous wave (excitation source)
EMF	Emerging microstructured fiber
FEM	Finite-element method
FWHM	Full width at half maximum
GVD	Group velocity dispersion
HNLF	Highly-nonlinear fiber
HDPE	High-density polyethylene (polymer)
hRI	high-refractive-index
ID	Inner diameter (of a capillary)
LDPE	Low-density polyethylene (polymer)
LIDAR	Light Detection And Ranging
LMA	Large mode area (fiber)
mIR	middle-infrared (spectrum)
MOF	Microstructured optical fiber
NLSE	Nonlinear Schrodinger equation
NOF	Nanostructured optical fiber
OD	Outside diameter (of a capillary)
PCF	Photonic crystal fiber

PE	Polyethylene (polymer)
PMMA	Polymethyl-methacrylate (polymer)
SC	Supercontinuum
SCG	Supercontinuum generation
SP(P)	Surface plasmon (polariton)
SPM	Self-phase modulation
SPP	Surface plasmon polariton
SSFM	Split-step Fourier method
THz	Terahertz
THz-TDS	Terahertz Time-Domain Spectroscopy
TIR	Total internal reflection
TOPAS®	Proprietary grade of amorphous cyclic-olefin-copolymer
TPA	Two-photon absorption
ZDM	Zero-dispersion wavelength of the material
ZDP	Zero-dispersion point
ZDW	Zero-dispersion wavelength

INTRODUCTION

Since their discovery in 1966 by Charles Kuen Kao (Nobel laureate, 2009), the adoption of low-loss silica (SiO_2) optical fibers for data delivery has rapidly increased to become the backbone of modern global telecommunication networks. Other contemporary and equally important applications of optical fibers are as sensors, illumination sources, and in light collecting devices, to name a few. Fibers sensors in particular have blossomed into a dynamic field of research with technologies developed for remote sensing of key physical parameters (temperature, pressure, strain, orientation, etc.) in hostile environments (e.g. for the mining, metallurgical and aerospace industries) and free from electromagnetic interference, as well as fiber probes and fiber endoscopes for biomedical applications. The host material of optical fibers can also be doped with rare-earth elements (e.g. Erbium, Ytterbium, Neodymium, Thulium) that provide signal gain, thus enabling active devices such as fiber amplifiers, optical switches and fiber lasers to be designed. Moreover, a periodic modulation of the refractive index, which runs in the length of the fiber, can be inscribed into the (photosensitive) core of an optical fiber. Such fiber Bragg gratings constitute a vital component in many fiber-based devices: in-fiber dielectric mirror, linear and ring resonators (as used in some fiber lasers), optical filters, fiber Bragg grating based sensors, and for chromatic dispersion management. Furthermore, by making use of the nonlinear optical effects (Raman scattering, four-wave mixing, self-phase modulation, etc.) in optical fibers, one further broadens the scope of fiber-based applications that is possible to design: Raman fiber amplifiers, wavelength conversion devices, and supercontinuum light sources, to name a few.

In retrospect, it is quite remarkable that these little strands of silica glass have allowed legions of scientists and engineers to achieve all of the above by primarily espousing a very simple form: the *conventional* step-index silica fiber [see Fig. 1.1(a)]. Here the term *conventional fiber* generally refers to optical fibers that possess mostly homogeneous cross-section geometry, and are fabricated with low-refractive-index materials ($n < 1.8$). In contrast, we define an *emerging microstructured fiber*, a microstructured optical fiber whose cross-section is characterized by an inhomogeneous and complex micro(nano-)structured geometry, often comprising subwavelength features, and which is in part or fully, fabricated either with high-refractive-index materials, composite or exotic materials [1, 2]. The cross-sections of two specific examples of emerging microstructured fibers are illustrated in Fig. 1.1(b)-(c).

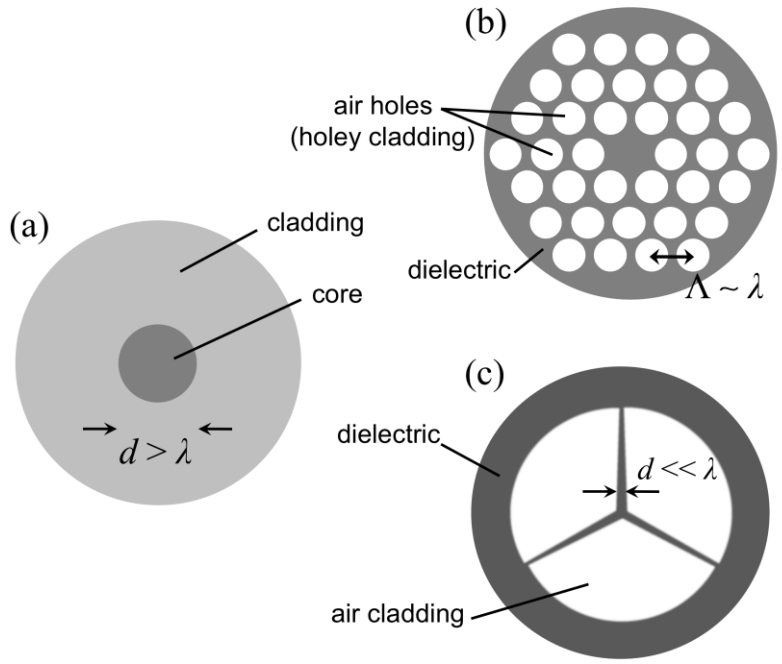

Figure 1.1 Cross-sections of (a) conventional step-index fiber (the core has a slightly higher refractive index than the cladding), and of two specific examples of emerging microstructured fibers: (b) a photonic crystal fiber, and (c) a suspended small core "wagon-wheel" fiber.

Yet for all their success, there are definite fundamental limitations to the use of conventional fibers. Pertaining first to linear optical properties: while silica-based optical fibers provide exceptionally low propagation losses ($\alpha \sim 0.2$ dB/km at $\lambda = 1.55$ μm); their range of operation is restricted to excitation wavelengths in the visible and near-infrared spectral regions ($\lambda \approx 0.4 - 1.9$ μm), and offer relatively low values of the refractive index ($n < 1.7$) even when dopants are added [3]. Access to higher refractive index materials would allow tighter optical mode confinement (and therefore larger optical nonlinearities) and the possibility of achieving a higher degree of miniaturization and integration. Moreover, the nonlinear refractive index of silica is intrinsically low ($n_2 \sim 2 \times 10^{-20}$ m^2/W), which entails the use of long light-matter interaction lengths (i.e. long fiber lengths) in order to observe significant nonlinear optical phenomena [4].

This is where *emerging microstructured fibers* (EMFs), and emerging waveguides in general, come into play. For one, the use of alternative and novel materials (e.g. fluorides, chalcogenides, and polymers) in EMFs allows to extend the operating range of optical fibers beyond the near-infrared region, towards the middle-infrared (mIR), far-infrared and terahertz (THz) spectral domains. In addition, the use of soft glasses (such as chalcogenides in this work)

and polymers, which both have low-forming-temperatures, makes possible the thermo-mechanical processing of almost arbitrary and highly complex structures. Hence, the freedom to precisely control the micro or nano-structuring of an EMF's cross-section, as well as the incorporation of hybrid materials in the EMF's composition, enable to expand the basic functionality of optical fibers, and as we will demonstrate later, to access novel regimes of modal propagation and reach unprecedented levels of optical nonlinearities.

The goal of this thesis was to explore various designs of EMFs, and to assess their performance via theoretical calculations and numerical simulations, for two main purposes:

1) The engineering of the chromatic dispersion and the enhancement of optical nonlinearities, for nonlinear applications in the mIR (supercontinuum generation in particular).

2) The efficient (low-loss) waveguiding of terahertz radiation; a purely linear application.

This thesis is delineated as follows: Chapter 1 provides an up-to-date review of the scientific literature relevant to microstructured optical fibers (MOFs) for nonlinear optical applications in the mIR spectrum [Chapter 1.1], and takes a look at the recent history of MOFs for low-loss THz waveguiding [Chapter 1.2]. Chapters 2 and 3 summarize the theoretical and numerical work undertaken to design and characterize the 4 distinct types of emerging microstructured fibers that were proposed and analyzed during my studies (Refs. [99], [100], [139] and [151]). In particular, we established that the waveguiding mechanisms prevalent in the proposed EMFs, significantly differ from the well-known total internal reflection guiding in conventional fibers. For example, in Chapter 2.2 we demonstrate a hybrid chalcogenide-metal nanofiber that supports a plasmonic mode enabling deep-subwavelength field confinement capabilities. And in Chapter 3.1, we show that the dominant waveguiding mechanism in a hollow Bragg fiber can shift from photonic bandgap guiding to anti-resonant capillary guiding, depending on the THz frequency region. Moreover, we demonstrate in Chapter 3.2 that a suspended core fiber [e.g. Fig. 1.1(c)] may predominantly support a Gaussian-like core-guided mode via total internal reflection (TIR) when the fiber is excited at higher THz frequencies; but this modal channel may be supplanted at lower THz frequencies by anti-resonant modes guided by the tubular cladding of finite thickness. Finally in Chapter 4, we discuss the scope and limitations of the work, summarize the contributions to new knowledge and techniques, and suggest future directions of research where new grounds can be gained on the topics covered therein.

CHAPTER 1 : LITERATURE REVIEW

1.1 Nonlinear microstructured optical fibers for the middle-infrared

Infrared light covers a large part of the electromagnetic spectrum, and is commonly divided into three spectral bands: near, middle and far-infrared. The middle-infrared band (mIR) covers the wavelengths between 2 and 20 microns. Since this region comprises several atmospheric transmission windows, it is of particular interest for LIDAR and remote sensing applications. Moreover, several molecules exhibit sharp resonant absorption lines in the mIR such that this spectral domain is especially relevant in the area of spectroscopy for the detection of gaseous analytes and suspended particles. The mIR is also widely used for thermal and hyperspectral imaging in surveillance applications, as well as in astronomy for characterizing celestial bodies. Finally, mIR light is an important tool for performing medical tasks such as laser surgery and bio-diagnostics.

Despite the numerous immediate benefits that may be reaped from applications of the mIR, its full exploitation remains limited by the lack of sources covering a large portion of this spectral domain. In fact, the majority of current mIR coherent sources (optical parametric oscillators, quantum cascade lasers, free electron lasers) are discrete and thus restrict applications to some specific wavelength at a single time. There is currently a strong demand within the industrial and academic communities for the creation of a compact and broad bandwidth mIR light source [5-7].

One of the most promising schemes pursued for achieving this objective is by pumping into a nonlinear microstructured optical fiber (MOF), very short and powerful optical pulses whose initial spectrum is stretched to a considerable extent by the nonlinear optical effects so as to generate a broad supercontinuum (SC) spectrum [8-11]. While this approach, using silica glass photonic crystal fibers (PCFs), has proven highly effective for the generation of a SC inside the visible and near-infrared spectrum within the last decade [12, 13]; research groups around the world have yet to replicate the same level of success inside the mIR spectrum.

There are a number of challenges that need to be addressed in order for mIR supercontinuum generation (SCG) in a nonlinear fiber to be achieved. First of all, alternative glasses must be found or compound glasses have to be developed, so as to replace silica glass, which becomes opaque for wavelengths beyond $\lambda > 2\,\mu\text{m}$ due to the onset of multiphonon absorption. The addition of heavy metals (Pb, Bi, Te, Zn) in oxide glasses enables to lower the multiphonon

excitation energy, thus extending the transmission window further towards the infrared [14]. However, all oxide-based glasses are fundamentally limited to wavelengths below 8 μm (see Fig. 1.2) [15, 16]. Thus in order to transmit at longer wavelengths – including at the technologically-important 10.6 μm CO_2 laser wavelength – infrared-transparent compound glasses such as fluoride and chalcogenide based glasses must be used for fabricating optical fibers.

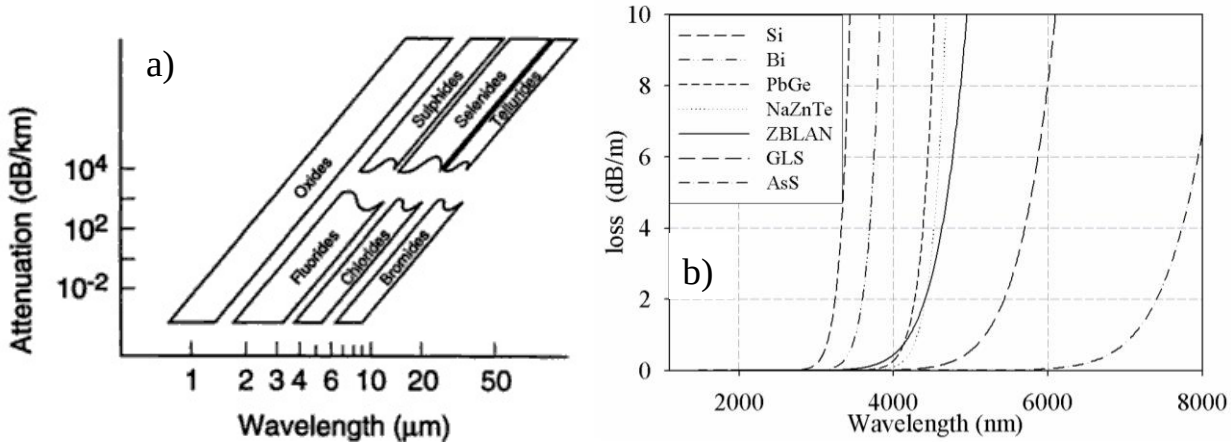

Figure 1.2 (a) Multiphonon absorption limits, and (b) absorption loss curves showing the multiphonon edge for various types of glasses. Reproduced from [14] with permission of Taylor & Francis Group LLC; permission conveyed through Copyright Clearance Center Inc.

Compound glass MOFs for the mIR may be classified into three broad categories: solid-core-guided amorphous glass fibers, crystal-based fibers, and hollow-core-guided fibers [17-19]. For each category of MOF, we now present a literature review focusing on fiber-based transmission at 10.6 μm, i.e. the design wavelength at which the first published paper [99] was based on. The rationale for this choice of design wavelength will be given shortly afterward.

Crystalline silver halides ($AgCl_xBr_{1-x}$ where $0 \le x \le 1$) have been used to fabricate, through extrusion, single-moded microstructured fibers and step-index fibers exhibiting total attenuation losses of ~ 2 dB/m [20, 21], 8 dB/m [22], 15 dB/m [23], and 16 dB/m [24] at the 10.6 μm wavelength. Fibers based on silver halides offer a number of advantages: good mechanical flexibility, high mIR transparency between 3−17 μm wavelength, non toxic, non hygroscopic and biocompatible material [23, 24]. However, this type of fiber is exclusively fabricated through extrusion which severely limits the control over the formation of structural defects. Moreover, it is still not possible to directly fabricate holey MOFs (i.e. fibers with running air holes) with this crystalline glass [22], and fiber lengths remain limited to a few meters ($L \le 15$ m) [23].

Hollow-core fibers transmit the optical power primarily within the low-loss gaseous core (filled with air or other gases) thus conferring hollow-core fibers a number of properties that sets them apart from their solid-core counterparts: lower theoretical losses, minimal nonlinear optical effects and high power threshold (in the gaseous core), lower material dispersion, small thermo-optic coefficient and negligible Fresnel reflexions at the facets [18, 19, 25]. In contrast to solid-core fibers whose guiding is via TIR; *leaky* hollow-core fibers confine the optical power within the core through specular reflexion on the inner walls. Typically, several metal and/or dielectric layers of reflective thin films are deposited on the inner walls of a tube made of polymers such as poly-ether-sulfone [25], polycarbonate [26], or silica. Given the relation $\alpha \sim 1/a^3$ between the optical losses (α) and the inner radius (a), it is not uncommon to find reports of relatively large hollow-core fibers with inner radii between 200-6000 μm [18, 19, 26]. A 2000 μm radius hollow-core fiber has been used to transmit 18 W of CO_2 laser ($\lambda = 10.6\,\mu m$) power over 2 meters distance with 0.02 dB/m losses [26]. A high-temperature-resistant germanium/silver-coated hollow-core fiber (a = 0.85 mm) demonstrated the ability to deliver kilowatts of power (>2.6 kW) from a CO_2 laser with losses of 0.1 dB/m [27]. However, hollow-core fibers generally guides light in an incoherent multimode regime. This is why they are mainly used for optical power delivery in medical and industrial applications. Moreover, hollow-core fibers are sensitive to bending losses: $\alpha \sim 1/R$ where R denotes the bending radius [18]. On other hand, bending losses incurred by the fundamental mode can be significantly mitigated if the inner reflective coatings are replaced with a multilayered dielectric mirror, in other words a Bragg fiber [28, 29]. The periodic low/high-index layers of the Bragg fiber create a photonic bandgap (PBG) that enables strong light confinement within the gaseous core within a certain frequency range [30, 31]. A chalcogenide/PES Bragg fiber, now commercialized by OmniGuide®, has demonstrated CO_2 laser waveguiding with 1 dB/m losses [25].

Solid-core optical fibers based on compound glasses confine light through the TIR principle. Fluoride based fibers, particularly the ZBLAN composition (ZrF_4-BaF_2-LaF_3-AlF_3-NaF) [32], provides the lowest attenuation (~ 1 dB/km) known in the wavelength range between 2 et 5 μm [33], low optical nonlinearities ($n_2 \sim 3\times10^{-20}$ m^2/W) and good chemical and mechanical stability [34]. Therefore, fluoride fibers constitute the best solution for linear optical applications inside the wavelength range 2−5 μm [14]. However as shown in Fig. 1.2, in order to guide light in the upper part (5−20 μm) of the mIR spectrum, chalcogenide glasses, i.e. compound glasses based on

the cations: Sulfur (S), Selenium (Se), and Tellurium (Te), represent the only amorphous-form solution (in opposition to the polycrystalline form of bromide and chloride glasses) [35, 36]. Typical stable compositions of chalcogenide glasses are As_2S_3 et le As_2Se_3 which respectively offer transparent windows in the mIR: 3−12 μm and 3−17 μm [35, 37, 38]. The incorporation of a heavier element such as Te in the $Te_xAs_ySe_z$ composition ("TAS" glasses) enables to enlarge the transmission window within 1−3 microns towards the far-infrared, depending on the exact chemical recipe [39]. Moreover, we note that a slight change in the chemical composition of a compound generally result in a corresponding change in the bulk refractive index of the obtained glass. The latter physico-chemical property can be exploited to fabricate single-mode step-index fibers. Accordingly, a single-mode fiber $As_2Se_3/Ge_2SeTe_{1.4}$ (core/cladding) was jointly developed by a French team (LESIA and *Le Verre Fluoré*) that demonstrated ~ 20 dB/m losses at 10.6 μm [40]. Similar fibers made from TAS glass ($Te_2As_3Se_5$) have reported losses of 10 dB/m [41] and ~ 5 dB/m [42] at 10.6 μm wavelength. The Quebec City based company *CorActive High-Tech Inc.*, produces a single-mode As-Se based step-index fiber offering comparable losses (~ 5 dB/m) [43] at 10.6 μm.

The second challenge towards achieving mIR supercontinuum generation (SCG) in an infrared fiber, is to adapt and refine the standard fabrication techniques of MOFs for these new compound glasses (also known as "soft glasses") which exhibit radically different thermo-mechanical properties. One of the most commonly used method of fabricating soft glass MOFs is via the *stack-and-draw* technique where millimeter-sized rods or capillaries of glasses are stacked together for creating the preform (i.e. a macroscopic version of the intended fiber) which is subsequently drawn into a fiber inside a draw tower heated near the solid-liquid transition temperature and under controlled pressurization [17; 44-46]. Alternative methods for fabricating the complex preforms include the *casting* method in which the silica/metallic mould is removed after preform fabrication [47-49], the *extrusion* technique where the preform is fabricated by passing a bulk glass billet through a structured steel die [50-52], and the *chemical vapour deposition* (CVD) method which promises the fabrication of highly-reproducible few-defect high-purity low-loss chalcogenide MOFs in the near future [53, 54].

The third challenge lies in the careful evaluation of the principal optical interactions for the efficient generation of a SC. This crucial step, in which this thesis is primarily concerned with, relates to the precise selection of an EMF's design parameters (materials, geometry, excitation

wavelength, etc.) towards engineering the chromatic dispersion profile, lowering the absorption losses, and optimizing the nonlinear light-matter interactions in the fiber. Since the first goal of this thesis was the design of chalcogenide-glass-based EMFs for the mIR possessing enhanced optical nonlinearities and suitable chromatic dispersion properties inside the 2 − 12 μm spectral range, we provide below a review of the state-of-the-art for the SCG in the mIR using nonlinear MOFs; starting with the early achievements and complemented with some elements of theory.

The complex process of supercontinuum (SC) occurs when an incident narrow-band pulse experiences an extreme spectral broadening leading to the creation of a large continuous band of frequencies in the output spectrum. In particular, when sufficiently intense ultrashort pulses propagate through a medium with significant third-order nonlinearity $\chi^{(3)}$, where $n_2 = 3\mathrm{Re}(\chi^{(3)})/8n$, they produce a sudden change in the local refractive index (known as the Kerr effect) that in turn modifies the phase, amplitude and frequency content of the pulse. Therefore, in the phenomenon of SCG it is the nonlinear interaction between the powerful incident light pulses with matter (e.g. solid core of a fiber) that drives the mechanisms which produces spectral broadening [55]. The first observation in 1969 of the generation of a SC was performed using picosecond pulses propagating in a sample of bulk silica glass [56]. The properties of a SC source combine the high coherence and power of a conventional laser, with a large spectral band. Microstructured fibers, and in particular dispersion-engineered PCFs, have extensively been used to generate supercontinua in the visible and near-infrared for a number of scientific, industrial and medical applications, and have most notably contributed to the field of *optical frequency comb* metrology. The first SC generated in a nonlinear waveguide was performed in 1976 using a silica optical fiber [57]. Subsequent research in SCG was performed using solid-state lasers in the near-infrared around 1310 nm or 1550 nm: the two main driving wavelengths for silica-fiber-based telecommunications [58-62]. The first demonstration of SCG inside a PCF was performed in the year 2000 using 800 nm femtosecond pump pulses that generated a SC covering the wavelength range from 400 nm to 1600 nm [63]. The advent of MOFs (in particular PCFs) has opened a new era in SCG research in which MOFs enable both strong optical mode confinement in the nonlinear medium, as well as exquisite control over the chromatic dispersion of the waveguide, thus allowing enhanced light-matter interaction [8-10].

Now to better appreciate the complex physical phenomenon of supercontinuum generation (SCG), we first outline the theory of *self-phase modulation* (SPM) which constitutes the leading

nonlinear optical effect that results in the spectral broadening of an optical pulse. In its simplest form (neglecting polarization effects and *group velocity dispersion* (GVD) in order to single out the role of SPM) the +*z*-directed propagation of a pulse, of normalized amplitude $U(z,T)$ and peak power P_0, in an optical fiber may be described by the following equation [4]:

$$\frac{\partial U}{\partial z} = \frac{ie^{-\alpha z}}{L_{\mathrm{NL}}}|U|^2 U \tag{1.1}$$

where α denotes the propagation losses, and the *nonlinear length* is defined as $L_{\mathrm{NL}} = 1/(\gamma P_0)$, where the *nonlinear parameter* (γ) is a figure of merit for the optical nonlinearity in the system:

$$\gamma = \frac{2\pi n_2}{\lambda A_{\mathrm{eff}}} \tag{1.2}$$

As its name suggests, the *effective mode area* (A_{eff}) provides a measure of the modal transverse spatial confinement [64, 65]:

$$A_{\mathrm{eff}} = \frac{\left|\int_{\mathrm{total}} dA\left(\mathbf{E}\times\mathbf{H}^*\right)\cdot\hat{z}\right|^2}{\int_{\mathrm{total}} dA\left|\left(\mathbf{E}\times\mathbf{H}^*\right)\cdot\hat{z}\right|^2} \tag{1.3}$$

A general solution to Eq. (1.1) is given by $U(z,T) = U(0,T)\cdot\exp\left[i\phi_{\mathrm{NL}}(z,T)\right]$, where the *nonlinear phase shift* is defined as:

$$\phi_{\mathrm{NL}}(L,T) = \left(\gamma P_0 L_{\mathrm{eff}}\right)|U(0,T)|^2 \tag{1.4}$$

The term $L_{\mathrm{eff}} = \left[1-\exp(-\alpha L)\right]/\alpha$ denotes the *effective length* of a fiber of actual length *L*. One notes that in the limit of no loss ($\alpha \to 0$) one has $L_{\mathrm{eff}} = L$. The SPM-induced spectral shift ($\delta\omega$) about the pulse of center frequency ω_0 and initial temporal form $U(0,T)$, is given simply by:

$$\delta\omega(T) \equiv -\frac{\partial\phi_{\mathrm{NL}}}{\partial T} = -\gamma P_0 L_{\mathrm{eff}}\frac{\partial}{\partial T}|U(0,T)|^2 \tag{1.5}$$

Equation (1.5) indicates that the frequency chirp induced by the SPM (in other words, the new frequencies generated via SPM) increases linearly in magnitude with the optical nonlinearity (γ), the input peak power (P_0) and the propagation distance (z) along the fiber of length *L*. In the case of Gaussian input pulses of temporal form $U(0,T) = \exp\left[-T^2/(2T_0^2)\right]$, the SPM-induced frequency chirp acquired during propagation produces a spectral broadening of the pulse, whose maximal extent is predicted by [4]:

$$\delta\omega_{\max} = 0.86\left(\frac{\gamma P_0 L_{\text{eff}}}{T_0}\right) = 0.86\left(\frac{2\pi n_2 P_0 L_{\text{eff}}}{\lambda A_{\text{eff}} T_0}\right) \tag{1.6}$$

where the input pulse's temporal half-width at 1/*e* (T_0) is related to the full width at half maximum (T_{FWHM}) via $T_{\text{FWHM}} = 2T_0\sqrt{\ln 2}$. Equation (1.6) thus reveals that the magnitude of SPM-induced spectral broadening depends directly on the value of the nonlinear index (n_2) intrinsic to the chosen material, and the pulse peak power (P_0); and is inversely proportional to the effective mode area (A_{eff}) and the input pulse width (T_0). In cases where $\delta\omega_{\max}/\Delta\omega_0 >> 100$ (where $\Delta\omega_0 = 1/T_0$ is the input pulse's spectral width), SPM leads to extreme spectral broadening, a phenomenon known as *supercontinuum generation* (SCG). Therefore in order to maximize the bandwidth of a SC, one typically selects very short pulse widths (e.g. femtosecond, picosecond, etc.), and designs a waveguide made from a highly-nonlinear material with a large n_2 value, inside of which the propagating mode's effective area (A_{eff}) is strongly confined at the given excitation wavelength.

Chromatic dispersion of the propagating mode also plays a crucial role in nonlinear fiber optics. In this regard, the mode propagation constant β (where the amplitude takes the form $U(z,T) \sim \exp\left[i(\beta z - \omega_0 t)\right]$) is expanded in a Taylor series about the pulse's center frequency ω_0:

$$\beta(\omega) = \beta_0 + \beta_1(\omega - \omega_0) + \frac{\beta_2}{2}(\omega - \omega_0)^2 + \frac{\beta_3}{6}(\omega - \omega_0)^3 + \ldots \tag{1.7}$$

where the expansion coefficients are given by:

$$\beta_m = \left.\frac{d^m \beta}{d\omega^m}\right|_{\omega=\omega_0} \tag{1.8}$$

In particular, the zero-order coefficient is related to the *effective refractive index* $n_{\text{eff}} = \beta_0/k_0$ of the mode, while the first-order coefficient is associated with the *group velocity* of the pulse envelope $v_g = 1/\beta_1$. The second-order coefficient (β_2) specifies the *chromatic dispersion of the group velocity* (GVD). The role of this last term is made more clearly in the definition of the *dispersion parameter* (*D*), which is alternatively used to describe the GVD in optical fibers:

$$D \equiv \frac{d\beta_1}{d\lambda} \approx -\frac{2\pi c}{\lambda^2}\beta_2 \tag{1.9}$$

Moreover, it is common practice to distinguish and separate the contributions of the chromatic dispersion intrinsic to the fiber material of refraction index $n_{\text{mat}}(\lambda)$, with that stemming from the waveguide (i.e. due to the spatial confinement of the mode in a waveguide):

$$D = D_{\text{mat}} + D_{\text{wvg}} \tag{1.10}$$

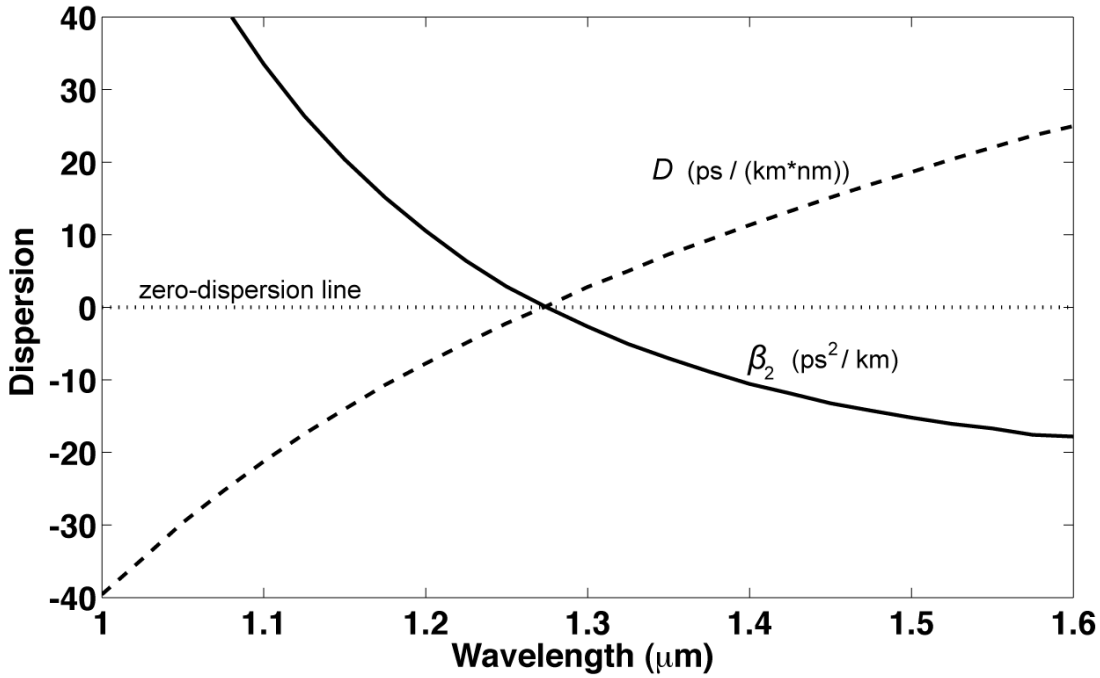

Figure 1.3 Variation of the group velocity chromatic dispersion (solid and long-dash lines) of plane waves propagating in bulk fused silica (data extracted from Chapter 1.2.3 in [4]).

In Fig. 1.3, the meeting point where $\beta_2 = D = 0$ is called the *zero-dispersion wavelength of the material* (ZDM) which in the case of bulk silica is $\lambda_{\text{ZDM}} = 1.27\,\mu\text{m}$. However in the case of waveguides (i.e. optical fibers and MOFs), the waveguide dispersion (D_{wvg}) often provides a strong contribution to the total dispersion (D) that effectively shifts the location of the *zero-dispersion wavelength* (ZDW), also known as a *zero-dispersion point* (ZDP). In principle, if one excites an optical fiber at the ZDW with a narrowband pulse, the pulse will subsequently propagate along the fiber without experiencing any distortion − except gradual amplitude loss − such as broadening or compression of its spectrum. But in practice, this is only true for short fiber lengths of negligible optical nonlinearity; otherwise one needs to take into account *third-order dispersion* effects (β_3 term in Eq. (1.7)) as well as the nonlinear effects. The pulse propagation regime where the sign of the dispersion in the waveguide is $\beta_2 > 0$ (or $D < 0$) is called the

normal dispersion regime; while the region $\beta_2 < 0$ (or $D > 0$) is named the *anomalous dispersion* regime of the waveguide. The anomalous dispersion regime is of fundamental importance in nonlinear fiber optics since it supports pulse-like solutions called *solitons* that are created through the balance of dispersive and nonlinear optical effects. Solitons can be found in other areas of physics including fluid mechanics, where their discovery is credited to the Scottish scientist John S. Russell who in 1834 observed that some water waves, created by the sudden stopping of boats in a narrow and shallow canal (i.e. a "fluid waveguide"), appeared to travel far along the canal while preserving their initial shape and speed. Similarly in guided optics, optical solitons represent special types of wave packets that propagate undistorted over considerable distances in an optical waveguide − despite the latter being dispersive ($|\beta_2| > 0$) and nonlinear ($\gamma > 0$) − due to the interplay between the effects of anomalous-GVD and SPM.

To characterize this relationship, we define the dimensionless parameter (*N*) based on the *dispersion length* ($L_D = T_0^2/|\beta_2|$) and the *nonlinear length* ($L_{NL} = 1/(\gamma P_0)$) [4]:

$$N^2 = \frac{L_D}{L_{NL}} = \frac{\gamma P_0 T_0^2}{|\beta_2|} \tag{1.11}$$

When $N << 1$, the role of GVD-dispersion dominates over nonlinear SPM effects in the evolution of the pulse propagation. Conversely when $N >> 1$, the role of SPM takes precedence over GVD. For anomalous-GVD ($\beta_2 < 0$) the creation of solitonic waves is admitted, in which case Eq. (1.11) defines the *soliton order* where N_{sol} =1 corresponds to the fundamental soliton wave. Therefore, pulses of high peak powers propagating inside a nonlinear waveguide can produce higher-order solitons ($N_{sol} > 5$) that generate new frequencies in a process called *soliton fission* where a high-amplitude N_{sol}-th-order soliton breaks up into N_{sol} lower-amplitude fundamental solitons [66-68]. A more detailed discussion regarding the generation of new optical frequencies through soliton fission, and nonsolitonic dispersive waves generation, is provided in Chapter 2.1 and Refs. [8-10]. It suffices to say here that the process of SCG in an optical fiber typically involves seeding with powerful pulses a MOF designed such that its nonlinearity (γ) is large, and for which the waveguide dispersion (D_{wvg}) is engineered at the laser seed wavelength in order for the sign of the GVD to be anomalous ($\beta_2 < 0$) and its magnitude small, thus giving access to high-order solitons [Eq. (1.11)]. Another criterion in the design of highly-nonlinear EMFs is that the GVD should not only be anomalous and small at the seed wavelength; but also

the GVD profile of the fiber should be engineered *as flat as possible* in the vicinity of the seed wavelength. The rationale behind this requirement is because: as the pulse propagates in the fiber, new frequencies are continuously being created on either side of the seed wavelength, first through SPM and subsequently via soliton fission and other nonlinear optical effects. Hence, if the magnitude or slope of the GVD is too large for these newly created frequencies, the corresponding optical waves will quickly die out (via chromatic dispersion) thus hindering the progression of the spectral broadening.

The last decade has seen the scientific discovery of the visible-near-infrared SCG in dispersion-engineered silica-MOFs, and the rapid adoption of this technology towards commercial applications in fully-packaged, robust and compact devices enabling high-precision measurements. However as alluded earlier, this technology still remains in its infancy when it comes to a nonlinear-MOF-based supercontinuum source in the mid-infrared (mIR) spectrum. Towards this goal, a step-index ZBLAN fiber demonstrated a SC with 0.7 W of average power between 0.9 and 3.6 μm wavelength [69]. The same authors later improved their experimental setup and reported an average of 10.5 W between 0.8 and 4.0 μm [70]. Chalcogenide-glass-based fibers are currently the subject of active research in the field of infrared fiber optics and mIR-SCG [71-78]. In that regard, chalcogenide glasses possess key advantages: they have a large transmission window in the mIR ($\lambda \approx 2-20\,\mu$m depending on the exact chemical composition), have large values of the refractive index (n) enabling strong modal field confinement, and possess very large values of the nonlinear refractive index (n_2) [79-83]. These properties make chalcogenide glasses excellent candidates as highly-nonlinear fibers (HNLFs) for SCG in the mIR. In particular, the use of MOF-technology enables to fabricate HNLFs made from a single material (e.g. chalcogenide glass) thus eliminating manufacturing problems (e.g. different heating T°, crystallization issues, and interfacial defects) related to the use of dissimilar materials for the core/cladding, and also enables to tailor the waveguide dispersion almost at will [84-88]. To that effect, a chalcogenide arsenic-selenide (As_2Se_3 glass) fiber was tapered down to a 1.2 μm waist diameter to yield an enhanced nonlinearity $\gamma \approx 68$ $W^{-1}m^{-1}$ (about 62 000 times larger than in a standard SMF-28 silica fiber) at the 1550 nm pump wavelength, and demonstrated a SPM-broadened spectrum between 1535 nm and 1565 nm [89]. Similar As_2Se_3-glass fiber tapers of 0.95 μm diameter demonstrated SC between 1200 nm and 1650 nm [90], and a As_2Se_3-taper of 0.80 μm diameter showed a SC from 1200 nm and 1700 nm [91], both using femtosecond pulse

lasers at 1550 nm center wavelength. A chalcogenide arsenic-sulphide (As_2S_3) taper of 1.3 μm diameter, and seeded by 1550 nm femtosecond pulses, demonstrated a SC between 1000 nm and 2000 nm [92]. A multinational research team fabricated an As_2S_3-glass-MOF with a suspended core (similar to Figure 1.1c) and subsequently measured a SC extending from 1500 nm to 1700 nm using picosecond laser pulses at 1550 nm [93]; and a SC from 1100 nm to 2400 nm using femtosecond pulses [94]. A tellurite-glass suspended-core MOF, with a tapered mid-section having 1.3 μm core diameter, was pumped with 1064 nm picosecond pulses and demonstrated a SC covering the region 730−1700 nm [95]. The widest yet reported mIR-SC generated in a soft-glass MOF was performed in a tellurite suspended-core fiber (2.5 μm core diameter) pumped by 1550 nm femtosecond pulses, producing a SC spectrum spanning the wavelength range between 800 nm and 4080 nm [96]. However no groups so far have been able to experimentally demonstrate a mIR-SC in a MOF inside the 5−12 μm wavelength range. Recent numerical studies have suggested that the use of pump wavelengths in the mid-infrared ($\lambda \geq 2$ μm), instead of the conventional lasers with wavelengths in the telecom window (1360−1625 nm), should enable SCG farther in the mIR using chalcogenide-glass MOFs [97, 98]. A similar numerical study was performed for this thesis, whose results were published in [99]. In that study we proposed a change in paradigm for mIR-SCG in MOFs, by taking the radical approach of using a CO_2 laser wavelength ($\lambda = 10.6$ μm) for seeding a chalcogenide As_2Se_3-MOF. Our numerical simulations demonstrated that SCG between 8.5 μm and 11.6 μm could be theoretically obtained via this approach using picosecond pulses. The results of this study are summarized in Chapter 2.1. This chapter also summarizes the results of a novel type of hybrid (chalcogenide-metal) nanostructured optical fiber (NOF) which suggests that giant optical nonlinearities could be achieved in such a EMF, thanks to the extremely strong modal field confinement enabled by the fundamental plasmonic mode. Results of this last study were published in [100] and a full description is given in Chapter 2.2.

1.2 Microstructured optical fibers for terahertz waveguiding

The terahertz frequency region (0.1 − 10 THz) is bounded on the blue side by the far-infrared region and on the red side by the microwave region [101]. In the last decade, technological advances in the generation [102-105] and the detection [106-109] of terahertz (THz) waves (also known as "T-rays") have come a long way. Both pulsed and continuous-wave (CW) terahertz

sources are now commercially available, along with complete THz imaging setups and THz spectroscopy turnkey systems based on free-space optics that are getting close to market introduction [110-113]. Terahertz-based systems have found new applications in several areas of science and engineering, especially for non-destructive testing in the manufacturing, security, and food industries [110, 111], as well as in biology and medicine [114], and many other areas where contrary to X-rays, the non-ionizing and slightly penetrating terahertz radiation can be exploited [115]. One of the most prominent commercial applications of THz imaging is in body scanners at airport security checkpoints (example shown in Fig. 1.4).

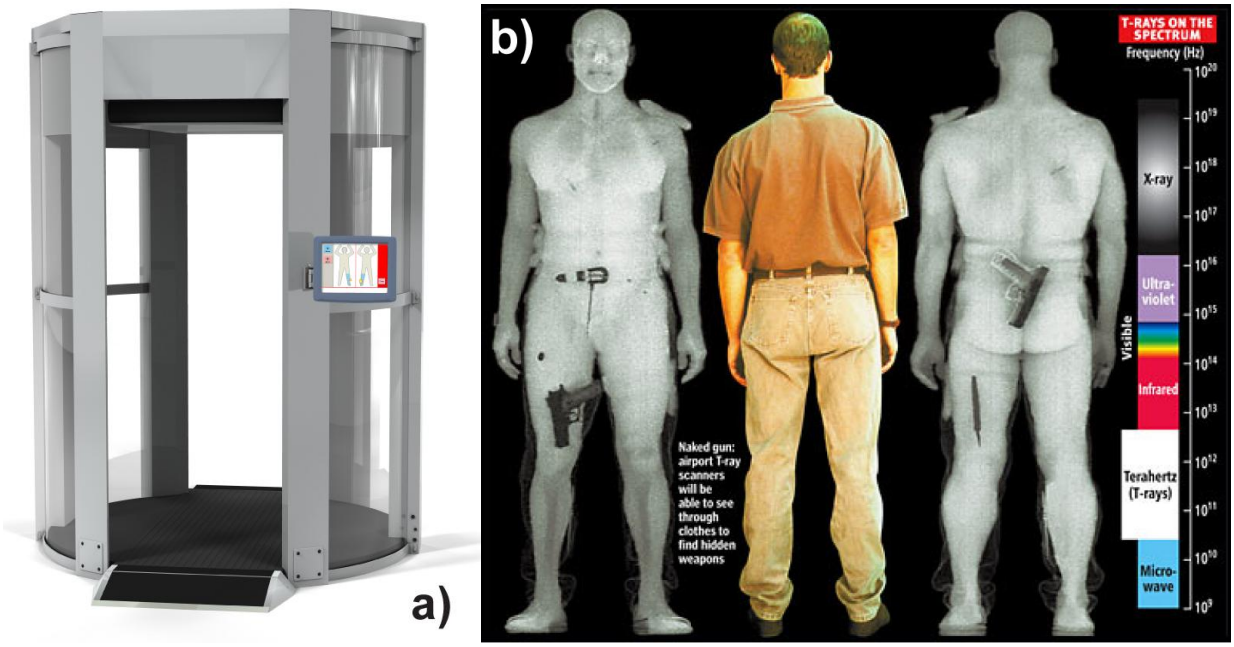

Figure 1.4 (a) Example of a typical open-cage fitted with a terahertz scanner for stand-off full-body THz imaging, and (b) false-color representation of the extracted THz signal absorption from a full-body THz scan. Images obtained from [116].

Furthermore, the potential for terahertz spectroscopy in the petrochemical [117, 118] and pharmaceutical [119] industries, as well as in biochemistry [120] and remote gas sensing [121], has been identified. However, the majority of current THz systems rely primarily on the bulky free-space optics together with a large nitrogen-purged cage to minimize the effects of resonant absorption from ambient water vapor, all of which severely limits the practical reach of these systems, and lead to additional overhead costs. As it is the case with most free-space-optics-based systems, their size is large and the constituent optical subcomponents require careful alignment, hence rendering such systems to be bulky and difficult to service and reconfigure. In the near-

infrared spectrum, the use of flexible optical fibers as links between individual optical components has resulted in the dramatic increase in systems' performance and reliability, a reduction in hardware footprint, and a higher level of integration. In constrast to both the near-infrared and mid-infrared regions, the history of dielectric fibers for the terahertz region is a very young one, with most technological breakthroughs occuring within the last decade. Therefore the development of the low-loss, low-dispersion, broadband THz fibers is currently a topic of active research, as it constitutes a decisive component for the next generation of THz-based technological applications. The reasons for using plastics in making THz waveguides are many: they represent cost-effective and widely accessible materials, offer a facile low-temperature processing, and exhibit relatively low losses when compared to other dielectrics in the terahertz spectral range. In the following, I provide a review of the latest technological progress in the design, fabrication and characterization of polymer microstructured optical fibers (MOFs) and polymer photonic bandgap (PBG) fibers for the guiding of terahertz waves. I will start by first outlining the main challenges in THz waveguiding and then present a selection of plastic MOFs and PBG fibers that have demonstrated promising results.

Currently the main obstacle in the design of THz dielectric waveguides lies in the large intrinsic material losses that significantly limit the effective propagation lengths of THz signals inside the waveguides. Plastic materials (i.e. polymers) offer some of the lowest losses in the THz; however as shown in Fig. 1.5(b), polymers still show significant losses in the terahertz frequency range [122-124].

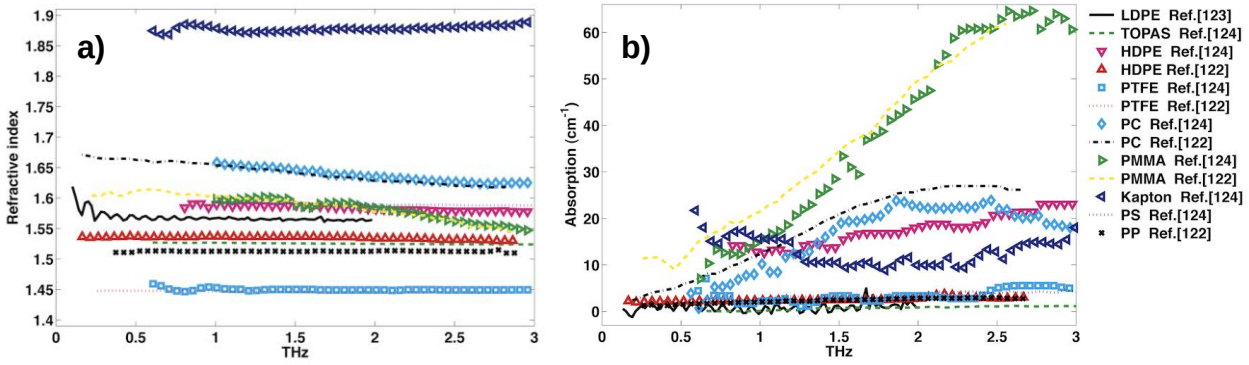

Figure 1.5 (a) Refractive index and (b) bulk absorption coefficient in (cm^{-1}) of common polymers used in the fabrication of THz waveguides. Legend: low-density polyethylene (LDPE), cyclic olefin copolymer (TOPAS®), high-density polyethylene (HDPE), Poly-tetrafluoroethylene (PTFE) a.k.a Teflon®, polycarbonate (PC), polymethyl-methacrylate (PMMA), polyimide (Kapton®), polystyrene (PS), Polypropylene (PP). Data compiled from references [122-124].

In fact, bulk polymers exhibit THz losses of at least $\alpha \geq 0.1\,\mathrm{cm}^{-1}$ corresponding to $\alpha \geq 43.4$ dB/m using the conversion formula: $\alpha(\mathrm{dB/m}) \cong 434 \cdot \alpha(\mathrm{cm}^{-1})$. The latter indicates that THz waves typically propagate just a few centimeters into a bulk plastic sample before becoming completely attenuated. Therefore, the first challenge in designing THz dielectric waveguides relates to the mitigation of the propagation losses. Because dry air (and a few other dry gases) exhibits negligible THz absorption, one simple and successful strategy for reducing the total propagation losses (α) is to maximize the fraction of optical power that is guided *outside* the lossy material, and *inside* the low-loss gaseous regions. The ratio of the modal losses (α_{mode}) to the bulk material losses (α_{mat}) can be evaluated to first-order approximation using the following expression [125]:

$$f_{\alpha} = \frac{\alpha_{\mathrm{mode}}}{\alpha_{\mathrm{mat}}} = \varepsilon_0 c \cdot \frac{\mathrm{Re}(n_{\mathrm{mat}}) \cdot \int_{\mathrm{mat}} |\mathbf{E}|^2 dA}{2 \int_{\mathrm{total}} S_z dA} \tag{1.12}$$

where the modal optical power in the *z*-direction of propagation is given by: $S_z = \frac{1}{2}\mathrm{Re}(\mathbf{E} \times \mathbf{H}^*) \cdot \hat{z}$.

One of the simplest plastic fibers that provide for a high fraction of power inside the low-loss gaseous regions is the solid core *subwavelength fiber* first introduced in 2006 by a National Taiwan University research group [126] and used extensively in THz signal delivery and imaging applications [127-130] as well as in THz evanescent-field sensing [131, 132]. The subwavelength fiber is a simple plastic wire having a circular cross-section of subwavelength-size diameter. This step-index fiber allows Gaussian-like single-mode HE_{11} operation via the total internal reflection (TIR) guiding mechanism. Due to the subwavelength diameter of the solid core, the fundamental guided mode has a strong presence in the low-loss air cladding [see example in Fig. 1.6 (c)].

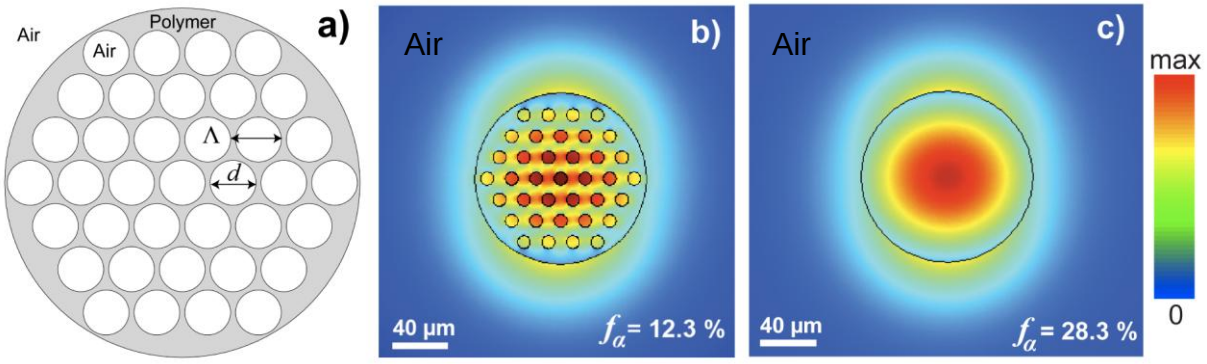

Figure 1.6 (a) Schematic of the cross-section of a porous fiber with N = 3 layers of holes. (b) Fundamental HE_{11} mode S_z-profile at 1 THz frequency in a subwavelength porous core PE fiber (d_{fiber} = 120 μm, d_{hole} = 9 μm), and (c) in a subwavelength solid core PE fiber (d_{fiber} = 120 μm). Calculations performed using the full-vector finite-element method.

Also in 2006, a group at Aachen University (Germany) made the important finding that inserting a single subwavelength-sized hole in the middle of an otherwise solid dielectric core, leads to a significant enhancement of the modal fields inside the (low-loss gas-filled) hole, thus resulting in a diminution of the propagation losses [133]. Taking one step further, it was theoretically proposed in 2008 by Hassani *et al*. [134, 135] of the Ecole Polytechnique de Montréal, and later experimentally demonstrated [136-138], that the incorporation of a periodic array (where the period $\Lambda < \lambda$) of deeply-subwavelength holes ($d_{\text{hole}} << \lambda$) within the core of a subwavelength fiber [Fig. 1.6(a)] allows to further reduce the propagation losses compared to that of a solid core fiber of identical diameter. To demonstrate this principle, Figs. 1.6(b)-(c) respectively present the distribution of the energy flux (S_z) in the propagation direction inside a *porous subwavelength fiber* made of polyethylene (PE), compared to the distribution inside a solid core PE fiber of the same outer diameter (d_{fiber} = 120 μm). A full-vector finite-element method was used (COMSOL Multiphysics® version 3.5a) to compute the fiber modes at 1 THz. In the case of the porous fiber we observe a strong presence of the modal fields with peak intensities residing in the low-loss holes [Fig. 1.6(b)]; while in the case of the solid-core fiber the peak modal fields are concentrated in the lossy dielectric core [Fig. 1.6(c)]. More specifically, we calculated with Eq. (1.12) that the fraction of modal power inside the lossy PE material is around $f_\alpha = 28.3\%$ in the case of the solid core fiber; while it is less than half that value ($f_\alpha = 12.3\%$) for the porous fiber. Consequently, the *porous subwavelength fiber* enables to significantly lower the modal propagation losses (α_{mode}) of dielectric fibers for THz waveguiding, compared to the non-porous solid core fiber (i.e. a bare microwire) of identical diameter. The last statement was confirmed experimentally in cutback measurements [137], which demonstrated losses as low as $\alpha \sim 0.02\,\text{cm}^{-1}$ (inside the range 0.16−0.31 THz) in porous subwavelength fibers even though the PE bulk losses were around $\alpha_{\text{mat}} \approx 0.2\,\text{cm}^{-1}$. The same study [137] also concluded that porous fibers allows to both broaden and shift the transmission window of the fiber towards higher THz frequencies, compared to non-porous fibers of equal diameter. Moreover, it is expected that porous fibers exhibit greater resilience to bending losses compared to the non-porous fibers of comparable diameters; which is explained by the stronger modal confinement inside the air holes of the porous core [135].

While the highly delocalized field in *subwavelength fibers* is favorable for lowering absorption losses incurred in the material; on the other hand, it represents a major inconvenience for handling the fiber during normal operation because of the strong perturbation induced to the mode through direct manipulation of the fiber, or via holders (such as strings and other apparatuses) used for maintaining the fiber into position. Therefore the issue of core encapsulation is crucial for subwavelength dielectric fibers. In the course of completing this thesis, I have participated in the design and characterization of all-polymer *suspended core subwavelength fibers* which solve the above-mentioned problems. First, by encapsulating the (solid/porous) core of a fiber within a polymer tube [as shown in Fig. 1.1(c)], the outer tube cladding prevents the highly delocalized core-guided mode from interacting with the surrounding environment, thus eliminating perturbation-induced losses incurred by direct manipulation of the fibers or due to fiber holders. Second, the solid tubular cladding confers greater mechanical stability and shielding for the subwavelength-sized core, thus allowing smaller bending radii and protection against the accumulation of undesirable surface contaminants. The results of this study were published in [139] and a discussion of these results is provided in Chapter 3.2.

Another type of polymer-MOF (fabricated with PMMA plastic) was proposed in 2008, where a large hollow core (670 μm average diameter) was surrounded by a periodic holey cladding [140]. This last type of polymer-MOF demonstrated minimum losses of $\alpha \approx 0.2\,\mathrm{cm}^{-1}$ at 1.3 THz. A very similar type of PMMA hollow-core fiber with a kagome-lattice holey cladding, showed minimum losses of $\alpha \sim 0.6\,\mathrm{cm}^{-1}$ inside the range 0.65−1.00 THz [141]. Other recently experimented cross-sections of MOFs for THz waveguiding include two different types of TOPAS®-polymer MOFs: one having a porous-core and a honeycomb holey cladding presenting minimum losses of $\alpha \sim 0.06\,\mathrm{cm}^{-1}$ inside the 0.95−1.10 THz range, and the other having a hollow-core and a honeycomb holey cladding with minimum losses of $\alpha \sim 0.09\,\mathrm{cm}^{-1}$ at 0.96 THz [142]. The first PCF [see Fig. 1.1(b)] for the terahertz, reported as early as 2002, was made with HDPE plastic and demonstrated $\alpha \sim 0.5\,\mathrm{cm}^{-1}$ at 0.6 THz [143]. Subsequently in 2004, a Teflon®-based PCF showed $\alpha \sim 0.12\,\mathrm{cm}^{-1}$ in the 0.1−0.4 THz range [144]. Another PCF made with TOPAS® polymer was reported in 2009 and demonstrated minimum propagation losses of $\alpha \sim 0.035\,\mathrm{cm}^{-1}$ in the range 0.5−0.6 THz [145].

Hollow-core fibers possess a major fundamental advantage towards the mitigation of material-induced absorption losses, compared to their solid/porous core counterparts, since

propagating modes are primarily guided within the low-loss gaseous core. Moreover, the propagation losses scale as $\alpha \propto \lambda^2/a^3$ with the hollow-core radius (a). Hence, losses could in principle be lowered to arbitrarily low levels simply by enlarging the core size. However, the downside of increasing the core diameter is in increased bending losses and in the highly multimode guidance, resulting in the low spatial quality of the guided modes. The most straightforward type of hollow-core fiber is created by a thin tube which guides, *not* via the TIR mechanism as in solid-core fibers; but instead through anti-resonant reflections from its walls of finite thickness (t). Such fibers are typically referred as ARROW waveguides for *anti-resonant reflecting optical waveguide* [146, 147]. Based on a simple Fabry-Pérot étalon framework, one can predict the periodic spectral spacing between two adjacent resonant frequencies in the fiber transmission spectrum [148]:

$$\Delta\nu = \frac{c}{2t\sqrt{n_{\text{clad}}^2 - n_{\text{core}}^2}} \tag{1.13}$$

where n_{core} and n_{clad} correspond respectively to the refractive indices of the gaseous core (usually air) and of the polymer tube cladding, while c represents the speed of light in vacuum. Equation (1.13) indicates that the periodic spacing between two resonant frequencies is inversely proportional to the thickness (t) of the capillary walls. Consequently in ARROW fibers, to achieve the widest spectral separation between two resonant frequencies − hence the widest transmission windows − it is necessary to have the thinnest possible walls (often below sub-millimeter dimensions) as well as a low-refractive-index-contrast for the core and cladding. A Teflon-based ARROW fiber of 0.5 mm thickness achieved $\alpha \sim 0.016\,\text{cm}^{-1}$ average losses in the 0.35−0.50 THz range [147]. A comparable PTFE-polymer, 0.3 mm thick, ARROW fiber demonstrated average losses of $\alpha \sim 0.04\,\text{cm}^{-1}$ between 0.57 THz and 0.75 THz [149]. The main drawbacks of thin-walled ARROW fibers are that they are challenging to fabricate, highly fragile and their performance is very sensitive to external perturbations such as direct handling.

Another type of hollow-core fiber, named *Bragg fibers*, provides an alternative and more robust solution to light confinement in the hollow core. Bragg fibers exploit resonant reflections from a periodic multilayered dielectric reflector surrounding the hollow core region. The periodic reflectors in Bragg fibers are composed of two alternating dielectrics featuring a high-refractive-index contrast [schematic in Fig. 1.7(a)] in order to maximize the fiber transmission bandwidth

[28]. The potential of all-polymer Bragg fibers for the transmission of terahertz light was first identified in 2007 [150] and later achieved in 2011 [151, 152].

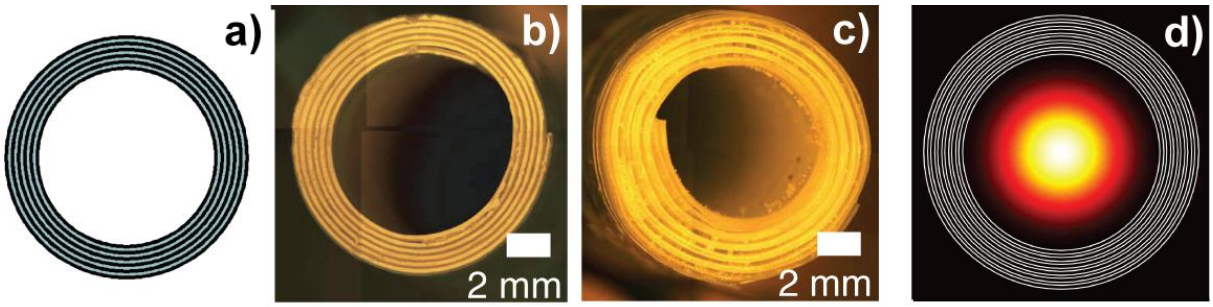

Figure 1.7 (a) Schematic of hollow Bragg fiber with N = 5 bilayers of high-index layers (dark fringes) and low-index layers (pale fringes). (b) Fabricated Bragg fiber with high-index TiO_2 doped layers and low-index PE layers. (c) Fabricated Bragg fiber with high-index PE layers separated by PMMA particles from the low-index air layers. (d) Fundamental HE_{11} mode profile at 1 THz inside the TiO_2-doped Bragg fiber of sub-figure (b) with d_{core} =6.63 mm, d_H =135 μm, and d_L =100 μm. Sub-figures (b) and (c) are reprinted from [151] and [152] respectively, with permission from The Optical Society of America.

The transmission characteristics of Bragg fibers are largely determined by the first few layers of the reflector adjacent to the hollow core. The design of Bragg fibers can thus incorporate a thick cladding that confers greater mechanical stability and lower sensitivity to the environment compared to thin-walled ARROW fibers. Two types of Bragg fibers were fabricated and characterized in [152]. The first type of Bragg fiber [cross-section in Fig. 1.7(b)] comprises a reflector made from low-refractive-index (n_L = 1.567) pure PE layers and high-refractive-index (n_H = 2.985) 80 wt.% (weight percentage) of TiO_2-doped PE layers. This composite TiO_2-PE Bragg fiber demonstrated minimum losses of $\alpha \sim 0.04\,\mathrm{cm}^{-1}$ at 0.69 THz. For this thesis, the effects of losses in the composite material on the fiber bandgaps were studied in detail. Our results reported in [151] and discussed in Chapter 3.1, indicated that there is a trade-off in doping a host polymer with high-refractive-index and high-loss additives (e.g. TiO_2 microparticles) for building periodic reflectors.

Pertaining to the fabrication of polymer-based fibers for THz waveguiding, subwavelength dielectric fibers are readily fabricated by drawing the macroscopic polymer rod into a micro-fiber. On the other hand, the complex microstructure of polymer-MOFs requires special techniques in order to be accurately executed. Similarly to soft-glasses used in the mid-infrared spectrum, such as chalcogenide glasses, the low-temperature-forming polymers are amenable to a wide variety of processing techniques [153]. The well-known "stacking" technique is commonly

used for the fabrication of polymer preforms of MOFs comprising a periodic pattern of holes, which must be prevented from collapsing during drawing of the fiber by internally pressurizing the holes [141, 143, 144]. Alternatively, a relatively simple "drill-and-draw" approach has also shown to be effective; although achievable preform lengths are somewhat limited by the length of the drill bits [139, 140, 145, 154].

In the case of *porous subwavelength fibers* comprising deep-subwavelength holes, three different fabrication methods have been demonstrated at this point. The first method is the *sacrifical polymer technique* where several rods of the sacrificial polymer (PMMA plastic in [137]) are first stacked inside a polymer tube (PTFE plastic in [137]). All the remaining empty interstices in the tube preform are then filled with granules of the fiber core polymer (e.g. low-density PE). In this process, it is important that the sacrificial polymer (PMMA) possess a higher glass transition temperature than the fiber core polymer (i.e. PE) in order for the PE granules to melt and fill out the interstitial space between the PMMA rods. The ensuing all-polymer preform is drawn into a fiber, which is then placed into a solvent bath to dissolve all the PMMA from the fiber and reveal the holes. Drawing of the porous fibers is considerably simplified in the sacrificial polymer technique since the resultant perform is fully solid and therefore the issues of hole collapse, uncontrolled blowing or bursting (due to improper pressure, for example), are virtually eliminated. The second fabrication technique of porous polymer fibers is through the *casting method* where the fiber preform is cast using a microstructured mold [137, 155]. For example, a mold made from silica capillaries (or rods) is filled with polymer granules, and is subsequently heated in a furnace to melt the polymer. After cooling, the silica mold is removed and etched away using hydrofloric acid, and the ensuing all-polymer preform − featuring air holes − is then drawn under gas pressure [137]. The last technique for fabricating porous fibers is through the extrusion method [138]. In addition this last method provides the ability to fabricate preforms with a highly complex and almost arbitrary cross-sectional microstructure since the extrusion die, usually made from steel, can be micromachined to the designer's will [51, 156, 157].

CHAPTER 2 : EMERGING MICROSTRUCTURED CHALCOGENIDE FIBERS FOR LINEAR AND NONLINEAR OPTICAL APPLICATIONS IN THE MIDDLE-INFRARED SPECTRUM

In this Chapter, I outline the approach taken to design two proposed types of highly-nonlinear fibers for the mid-infrared (mIR) spectrum, the *microporous chalcogenide fiber* [Chapter 2.1] and the *nanostructured chalcogenide-metallic hybrid fiber* [Chapter 2.2]; and also present the results of numerical simulations that demonstrated their potential for nonlinear optical applications.

Lately, there has been substantial interest in the design and fabrication of emerging microstructured fibers (EMFs) [1, 2] − incorporating subwavelength features [158, 159] using high-refractive-index [160-162] or hybrid materials [163-166] − towards finding new ways of interacting light with matter. Such EMFs have opened the access to novel regimes of wave guiding [167-169], including *subwavelength confinement of light* and *extreme optical nonlinearity*, both of which were of specific interest for this thesis.

Pertaining to the fiber's nonlinear parameter (γ), its standard definition [in Eq. (1.2)] is a perfectly valid expression for the conventional fibers with homogeneous cross-sections and low-refractive-index contrast. But its validity breaks down in EMFs possessing inhomegeneous cross-sections and fabricated with *high-refractive-index* (hRI) or exotic materials such as metals.

The first reason stems from the longitudinal component E_z of the *E*-field − which is duly neglected in Eq. (1.2) (i.e. only transverse field components are accounted for) − but becomes significant ($\geq 15\%$) for EMFs operating in the strong guiding regime owing to a hRI-contrast, and for EMFs incorporating subwavelength-sized features.

The second reason originates from the simple fact that the standard definition [Eq. (1.2)] is only suitable for waveguides in which the nonlinear refractive index (n_2) can be assumed homogeneous across the whole cross-section of the fiber [as in Fig. 1.1(a)]. Therefore a novel full-vectorial definition of the nonlinear parameter (γ^V, where the "V" superscript indicates the vectorial nature), which is also appropriate for inhomogeneous cross-sections, is required for the accurate evaluation of optical nonlinearities in EMFs [64]:

$$\gamma^V = \frac{2\pi \bar{n}_2}{\lambda A_{\text{eff}}} \tag{2.1}$$

where $$\bar{n}_2 = \frac{\varepsilon_0}{\mu_0} \cdot \frac{\omega}{c} \cdot \frac{\int_{\text{total}} n^2(x,y) \cdot n_2(x,y) \cdot \left[2|\mathbf{E}|^4 + |\mathbf{E}^2|^2 \right] \cdot dA}{3 \int_{\text{total}} \left| (\mathbf{E} \times \mathbf{H}^*) \cdot \hat{z} \right|^2 dA} . \quad (2.2)$$

The term $\bar{n}_2$ defines the *average nonlinear refractive index* over the inhomogeneous cross-section, weighted with respect to the field intensity distribution inside regions filled with nonlinear material(s) of spatial distribution $n_2(x,y)$.

We now turn our attention to the design of EMFs for nonlinear optical applications in the mIR − whose effective optical nonlinearities are evaluated with Eq. (2.1) − towards the development of high brightness and coherent sources of mIR, via supercontinuum generation (SCG). The efficiency and bandwidth of SCG intimately depends on the maximization of the *nonlinear parameter* (γ') and on the *engineering of the group velocity chromatic dispersion* (GVD). Solutions to implement these two key aspects are proposed and explained in the next Sub-sections: 2.1 and 2.2.

2.1 Chalcogenide microporous fibers for linear and nonlinear applications in the mid-infrared

2.1.1 Introduction

The process of supercontinuum generation (SCG) is strongly dependent on the phase-matching conditions between the nonlinear optical processes and the input pulses. Therefore the importance of engineering the group velocity dispersion (GVD) was shown to be critical for optimizing the nonlinear effects and maximizing the corresponding SC bandwidth and its power [8-10]. Towards this end, we proposed a new type of MOF: the *microporous chalcogenide fiber*, which enables to engineer the GVD and the propagation losses of the fiber, thus optimizing the SCG and enhancing the output spectral broadening [99, 170, 171].

As highlighted in Chapter 1.1, previously published studies of fiber-based mIR-SCG have largely focused on fiber designs featuring a *small solid core* either in a freestanding or tapered configuration (e.g. nanowires and nanotapers), or suspended in the air through thin bridges in the so-called “wagon wheel” geometry [see Fig. 1.1(c)], and with pump laser wavelengths located in the near-infrared telecommunication window. While *small-core* designs greatly enhance the optical nonlinearities by lowering the A_{eff} value in Eq. (2.1), they offer limited freedom for

engineering the GVD. Typically in small-core fibers, the strong waveguide dispersion (D_{wvg}) enables to *blue-shift* the first zero-dispersion point (ZDP) – with respect to the material zero-dispersion wavelength (ZDM) of the compound glass – towards the near-infrared range (1.0 – 2.5 μm) as clearly demonstrated in the example of Fig. 2.1 below.

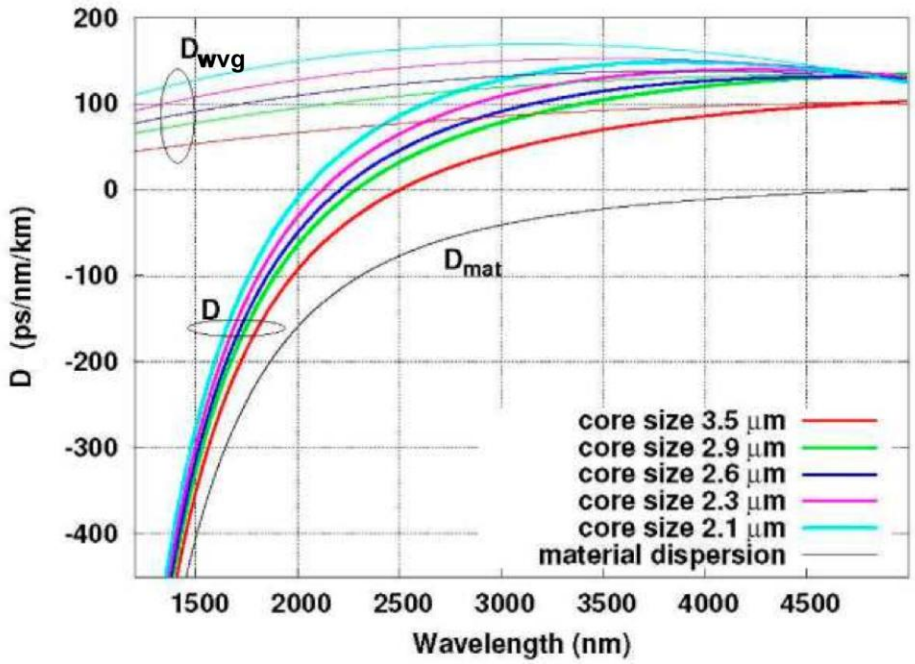

Figure 2.1 Total chromatic dispersion (D) in sulfide As_2S_3-glass suspended small-core fibers with varying core sizes. The strong *anomalous* waveguide dispersion (D_{wvg}) enables to partly compensate for the *normal* dispersion of the material (D_{mat}) thus allowing to blue-shift the zero-dispersion wavelength of the waveguide from that of the material dispersion. Reprinted from [93] with permission from The Optical Society of America.

In the contribution summarized in this sub-section (and reported in [99, 170, 171]), I demonstrate that with proper engineering of the core microporosity one can create zero-dispersion points inside the mIR, and most notably, *red-shifted* from the ZDM.

The benefit of using a porous core with deep-subwavelength holes for reducing the absorption losses of the fundamental mode was first proposed for terahertz (THz) polymer waveguides [134, 135]. These earlier studies demonstrated that mode propagation in porous polymer fibers – whose guiding mechanism is total internal reflection (TIR) between a higher average-refractive-index porous core and a lower refractive-index cladding – compares favorably over the corresponding small solid-core designs in terms of modal absorption losses and macrobending losses. In the early stages of the project, we noticed that this ability of porous fibers for lowering propagation losses is also desirable for nonlinear mIR applications. Moreover,

it was hypothesized that the core porosity would introduce an additional design parameter which one could exploit to engineer the waveguide GVD.

2.1.2 Optical properties of the chosen nonlinear glass

For this project, arsenic-selenide (As_2Se_3) chalcogenide glass was chosen as the dielectric material because of its broad bulk transparency (2 – 14 μm) and its high refractive index [see Fig. 2.2], along with a large nonlinearity ($n_2 = 1.1 \times 10^{-17}$ m^2/W) in the mIR spectrum. Although As_2Se_3 typically exhibits relatively large losses (~ 5 dB/m) at 10.6 μm, it remains one of the low-loss glasses currently available for mIR optics. We note in Fig. 2.2 that $n_{mat} = 2.768$ and $\alpha_{mat} = 1.4$ m^{-1} (or 4.81 dB/m) for As_2Se_3 at $\lambda = 10.5\ \mu m$, and the material zero-dispersion wavelength (ZDM) is located at $\lambda_{ZDM} = 7.225\ \mu m$.

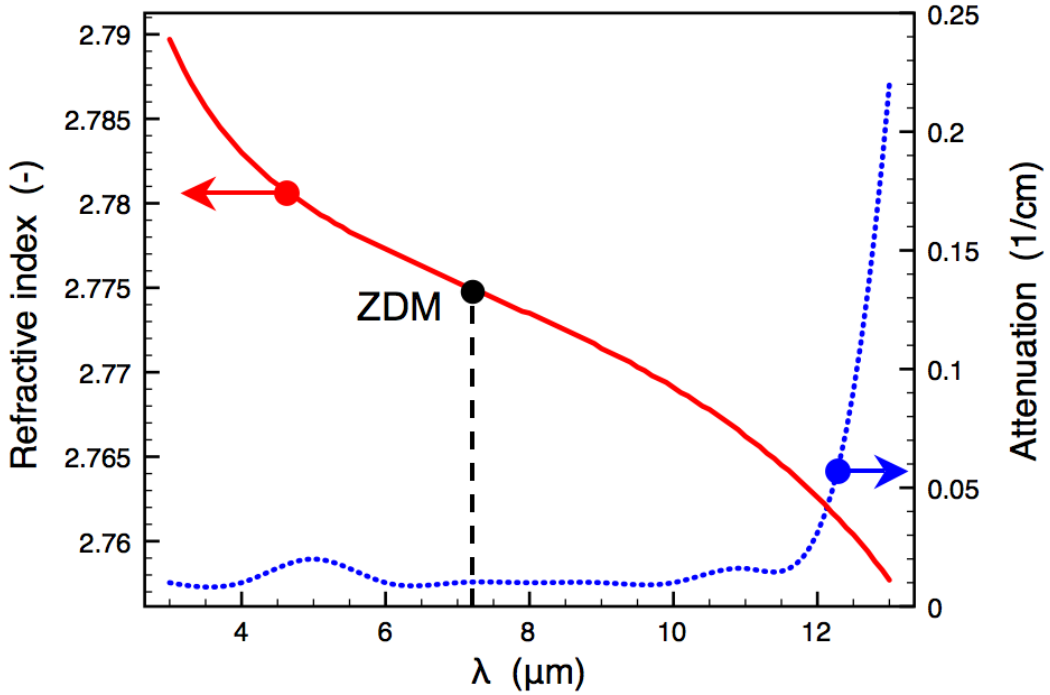

Figure 2.2 Refractive index (solid red line) and absorption coefficient (dotted blue line) of bulk selenide (As_2Se_3) glass as a function of excitation wavelength. The material zero-dispersion wavelength (ZDM) is located at 7.225 μm. Reprinted from [99] with permission from The Optical Society of America.

2.1.3 Geometry of proposed design

The basic geometry of a microporous fiber – depicted schematically in Fig. 2.3(a) – incorporates N layers of deep-subwavelength-sized air holes of diameter d_{hole} in a triangular

lattice of pitch Λ (also of subwavelength dimensions: $\Lambda < \lambda$). The total outer diameter of the core is given by $d_{\text{fiber}} = (2N+1)\cdot\Lambda$ and an infinite air cladding is assumed, thus simulating a freestanding dielectric micro-(nano-)porous core fiber. Moreover, in order to simplify the analysis this theoretical investigation focuses on the case of N = 4 layers of subwavelength holes; but the results and the related discussion remain valid with scaling to more complex (N > 4) and larger microporous fibers. We note that strict periodicity is not a requirement for TIR guiding in porous fibers. In fact, the main requirement pertains to the refractive index' spatial distribution within the porous core – due to a random distribution of deep-subwavelength holes ($d_{\text{hole}} << \lambda$) – which must be homogeneous on average.

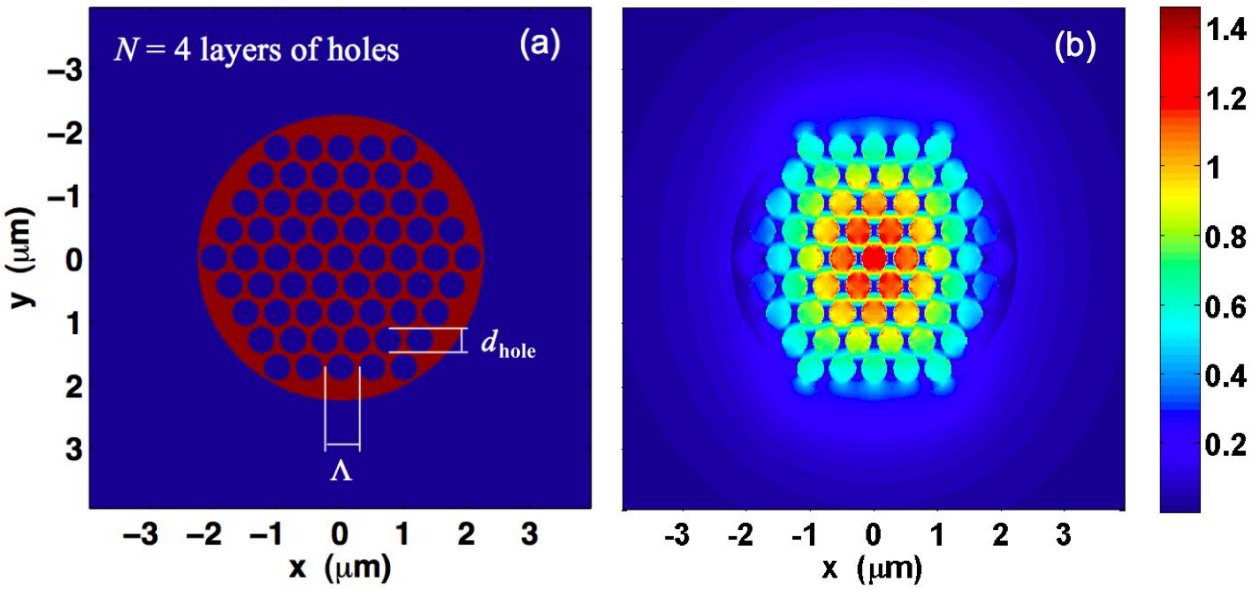

Figure 2.3 (a) Refractive index distribution (red: As_2Se_3-glass, blue: air) in a N=4 ($\Lambda = 0.50\,\mu$m, $d_{\text{hole}} = 0.42\,\mu$m) chalcogenide microporous fiber, and (b) S_z-power distribution (in a.u.) of the fundamental HE_{11} mode at the 10.5 μm input wavelength. Reprinted from [99] with permission from The Optical Society of America.

For the vectorial finite-element study of this EMF's modal properties, I kept the number of layers of holes fixed at N=4, and then systematically scanned the geometrical parameters ($\Lambda = [0.20,\ 0.25, ...,\ 1.00]\ \mu m$ and $d_{\text{hole}} = [0.12,\ 0.14, ...,\ 0.90]\ \mu m$) inside a broad range of excitation wavelengths in the mIR spectrum ($\lambda = [3.0,\ 3.5, ...,\ 16.0]\ \mu m$) in order to evaluate the GVD in the vicinity of the principal wavelength of interest ($\lambda = 10.5\ \mu m$) as accurately as possible. More specifically, the GVD was evaluated using the expression $D = -(\lambda/c)\cdot d^2 n_{\text{eff}}/d\lambda^2$, where the wavelength dependence of the computed real effective refractive index (n_{eff}) of the fundamental

HE_{11} mode was interpolated via cubic spline interpolation and then fitted to a polynomial function of degree 11. It is also instructive to calculate the cross-sectional areal density of air holes in the fiber, in other words its *porosity* (*p*), which can be expressed directly for our periodic triangular configuration:

$$p = \frac{A_{\text{holes}}}{A_{\text{tot}}} = \frac{\left[3\left(N^2+N\right)+1\right]}{\left[4\left(N^2+N\right)+1\right]} \cdot \left(\frac{d_{\text{hole}}}{\Lambda}\right)^2 \tag{2.3}$$

where A_{hole} denotes the cross-sectional area occupied by all the holes, and A_{tot} is the total cross-section area of the MOF.

It also follows that the fraction of glass material (f_{m}) in the microporous fiber is given by: $f_{\text{m}} = 1 - p$. Another important property of the EMF is the fraction of modal propagation loss to bulk material absorption (f_{α}) defined in Eq. (1.12).

2.1.4 Results and discussion of the finite-element method simulations

Intuitively, one expects that f_{α} be proportional to f_{m} since the magnitude of the modal losses should scale linearly with the amount of optically absorbing materials inside the core. The latter statement is clearly confirmed by the density plots of Fig. 2.4 where the magnitudes of f_{m} and f_{α} are respectively plotted as a function of MOF geometrical parameters Λ and d_{hole}. As expected, lowest propagation losses are achieved in designs with the largest porosity, i.e. near the limit $d_{\text{hole}}/\Lambda \to 1$.

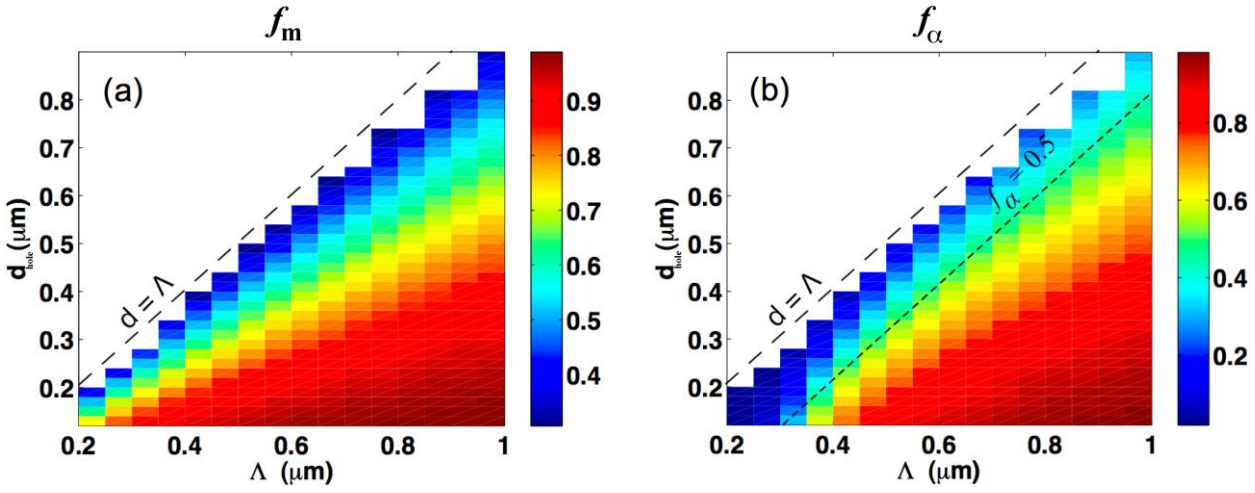

Figure 2.4 (a) Cross-sectional density f_{m} of solid material in *N*=4 layers microporous fiber and (b) fraction of modal absorption f_{α} over bulk As_2Se_3 absorption at λ=10.5 μm, as a function of parameters (Λ, d_{hole}). The dotted line identifies the regions of f_{α} = 0.5 (Reprinted from [99]).

In particular, Fig. 2.4(b) indicates that modal propagation losses in a porous fiber can be lowered by half the bulk material absorption value for a hole diameter-to-pitch ratio of $d_{\text{hole}}/\Lambda \approx 0.70$, which corresponds to a $p \approx 37$ % porosity. Similarly, the magnitude of the real part of the modal effective refractive index ($\text{Re}(n_{\text{eff}})$) scales almost linearly with f_{m} and f_{α} as shown in Fig. 2.5(a). On the other hand, in Fig. 2.5(b) the density plot of the effective mode area (A_{eff}) – definition in Eq. (1.3) – indicates a region in the (Λ, d_{hole}) parameter space where minimization of A_{eff} can be achieved. In the case of As_2Se_3-glass microporous fibers, minimization of A_{eff} at λ=10.5 μm is achieved for Λ=0.40 μm and $d_{\text{hole}} \to 0$, i.e. in the limit of the solid-core microwire.

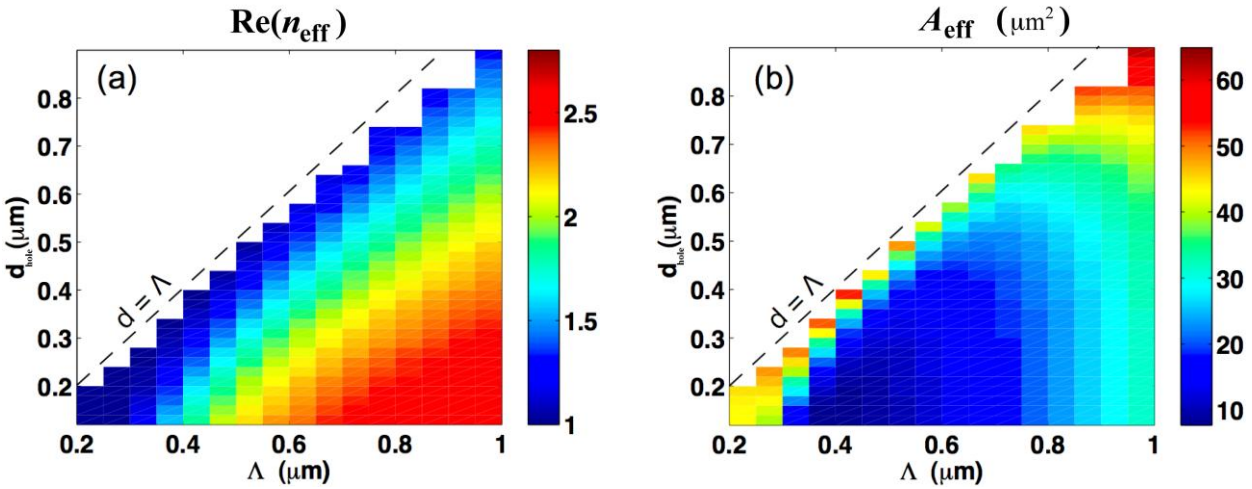

Figure 2.5 (a) Real effective refractive index and (b) effective mode area of the fundamental mode in N = 4 layers As_2Se_3 microporous fiber at λ = 10.5 μm, as a function of parameters (Λ, d_{hole}). Reprinted from [99] with permission from The Optical Society of America.

The value of the chromatic dispersion parameter (D) and the dispersion slope ($dD/d\lambda$) at the pump wavelength λ = 10.5 μm are respectively plotted, as a function of the structural parameters (Λ, d_{hole}), in Fig. 2.6(a) and Fig. 2.6(b).

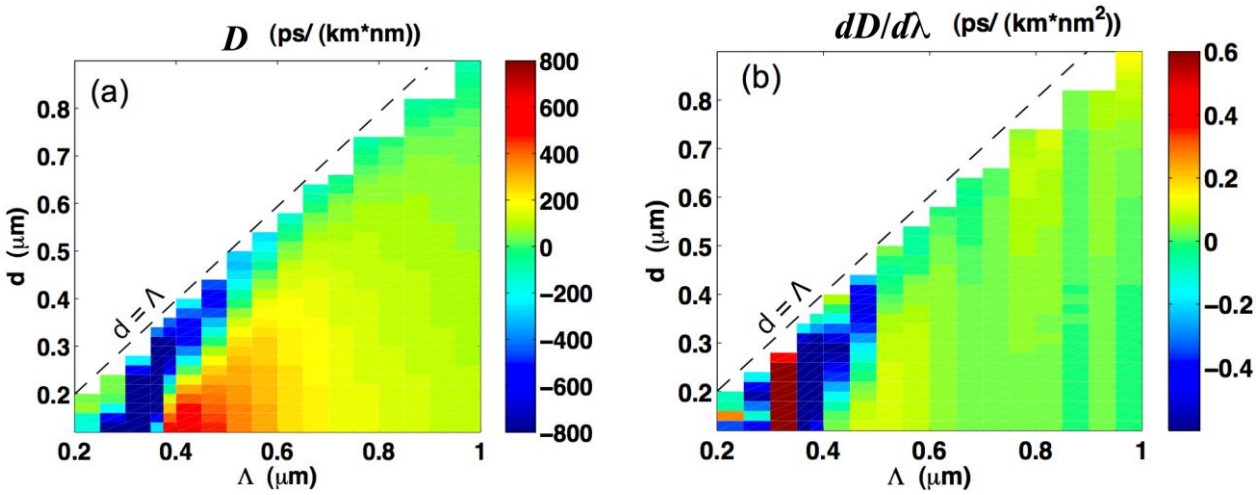

Figure 2.6 (a) Dispersion parameter (D) and (b) dispersion slope ($dD/d\lambda$) in N = 4 layers As_2Se_3 microporous fiber at λ = 10.5 μm, as a function of parameters (Λ, d_{hole}). Reprinted from [99].

In these dispersion plots we can identify several ("green") regions of low ($D \to 0$) and flat ($dD/d\lambda \to 0$) chromatic dispersion for λ = 10.5 μm. Two such examples of low and flat GVD-engineering in microporous fibers occur for structural parameters (Λ=0.5, d_{hole}=0.38)μm and (Λ=0.7, d_{hole}=0.62)μm, for which the detailed dispersion curves are presented respectively in Fig. 2.7(a) and Fig. 2.7(b). In these figures, the material dispersion curve (D_{mat}) is also plotted (blue curve) in order to appreciate the strong contribution of the waveguide dispersion (D_{wvg}) to the total dispersion (D).

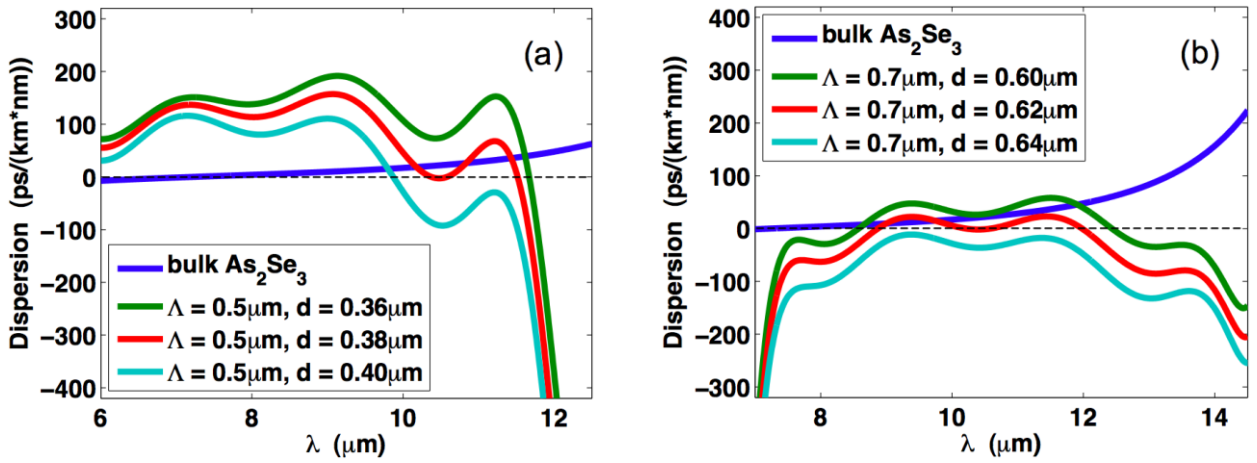

Figure 2.7 (a) Chromatic dispersion curves ($ps/km\,nm$) showing near-zero and flattened dispersion at λ=10.5 μm for parameters (a) (Λ=0.50, d_{hole}=0.38)μm, and (b) Λ=0.70, d_{hole}=0.62)μm. The blue curve plots the As_2Se_3-glass material dispersion. Reprinted from [99].

As shown in Fig. 2.6(a)-(b), the magnitude of the waveguide dispersion [defined in Eq. (1.9)] grows larger as the core diameter gets smaller which can result in very steep dispersion slopes. Knowing that the effective mode area (A_{eff}) directly depends on the core diameter, the steep dispersion slopes are predicted from the inverse relation between A_{eff} and the absolute GVD ($|\beta_2|$) [172]:

$$|\beta_2| \approx \frac{\lambda^3}{4\pi^2 c^2 n_{\text{mat}} A_{\text{eff}}} \tag{2.4}$$

This last relation also helps to explain the sharp transition from positive to negative dispersion regimes near Λ=0.40 μm in Fig. 2.6(a). The most significant feature, shown in Fig. 2.7(a)-(b), is the formation of several zero-dispersion points (ZDPs), and most importantly, the creation of a ZDP at the pump wavelength (λ = 10.5 μm), which is *red-shifted* from the ZDM of As_2Se_3 glass. The ability to engineer the GVD so as to create ZDPs that are red-shifted from the ZDM, is a distinctive feature of the microporous fiber design that separates it from standard small-core designs. This feature of microporous fibers can be exploited for nonlinear phase-matching at long wavelengths (5 – 12 μm) in the mid-IR. In the next part of this project, we numerically investigate the possibility of exploiting the latter dispersive feature for seeding a mIR-SC at the λ=10.5 μm pump wavelength, close to a red-shifted ZDP.

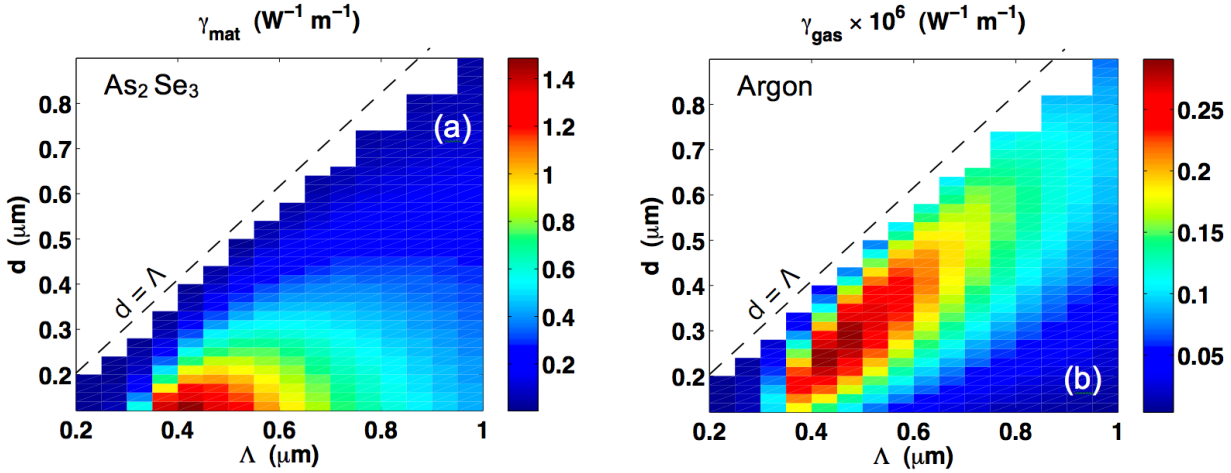

Figure 2.8 Contribution to the nonlinear parameter γ ($W^{-1}m^{-1}$) due to (a) As_2Se_3 glass, and (b) Argon gas-filled holes at λ=10.5 μm as a function of (Λ, d_{hole}) for a N = 4 layers microporous fiber. Gas nonlinearities are multiplied by a factor 10^6, for scaling reasons. Reprinted from [99].

The definition of the effective nonlinearity in Eqs. (2.1)-(2.2) takes into account the precise spatial distribution of nonlinear material(s) present in the EMF: $n_2(x,y)$. Hence it opens up the

possibility of incorporating a nonlinear gas inside the subwavelength holes, and to investigate the corresponding nonlinear light-gas interactions occuring within the holes. Therefore the value of the nonlinear parameter (γ) was evaluated in both As_2Se_3-glass [Fig. 2.8(a)] and inside the gas-filled holes [Fig. 2.8(b)] where Argon served as the exemplar nonlinear gas (with nonlinear refractive index of $n_2^{\text{Argon}} = 9.8 \times 10^{-24}\ \text{m}^2/\text{W}$ [173]).

In the case of solid As_2Se_3-glass, it is expected from the definition $\gamma^{V} = 2\pi\bar{n}_2/(\lambda A_{\text{eff}})$ in Eq. (2.1), that the nonlinear parameter (γ) is maximized for values of the structural parameters (Λ, d_{hole}) for which the effective mode area (A_{eff}) is minimized [see Fig. 2.5], as confirmed in Fig. 2.8(a). On the other hand, Fig. 2.8(b) indicates that optimization of the nonlinear light-gas interaction in microporous fibers occur in an ellipsoidal region of the (Λ-d_{hole}) parameter space, with nonzero hole diameters ($d_{\text{hole}} > 0$). Of greater interest for nonlinear fiber optics applications, is the recognition that not only is it possible to achieve relatively large effective nonlinearities in matter (γ_{mat}) or in gases (γ_{gas}), but one can also elect to operate in a (Λ-d_{hole}) parameter region of low and flattened chromatic dispersion [see Fig. 2.6(a)-(b)] for which phase-matching with a given nonlinear optical process is optimized. And combined with the lower attenuation due to the core porosity [see Fig. 2.4(b)], one realizes that microporous fibers enable long interaction lengths in nonlinear media.

2.1.5 Simulation of the nonlinear Schrodinger equation for pulse propagation in nonlinear optical media

In what follows, we describe numerical simulations of the nonlinear optical interactions in chalcogenide microporous fibers, based on the scalar nonlinear Schrodinger equation (NLSE) [4]:

$$\frac{\partial A}{\partial z} + \frac{\alpha}{2}A - i\sum_{m\geq 2}\frac{i^m \beta_m}{m!}\frac{\partial^m A}{\partial t^m} = i\gamma\left[\,|A|^2 A + \frac{i}{\omega_0}\frac{\partial}{\partial t}\left(|A|^2 A\right) - T_R A\frac{\partial |A|^2}{\partial t}\right] \qquad (2.5)$$

where $A = A(z,t)$ designates the slowly-varying pulse envelope. The first term on the right-hand side accounts for the optical *Kerr effect*, while the second and third terms use first-order approximations to respectively include the *self-steepening* effects and the delayed ionic *Raman response*. Assuming a Lorentzian profile for the Raman gain spectrum, the Raman response function may be expressed in a mathematically practical form [4]:

$$h_R(t) = \frac{\tau_1^2 + \tau_2^2}{\tau_1 \tau_2^2} \exp\left(-\frac{t}{\tau_2}\right) \cdot \sin\left(\frac{t}{\tau_1}\right) \tag{2.6}$$

where the parameter τ_1 relates to the phonon oscillation frequency, while τ_2 defines the characteristic damping time of the network of vibrating atoms. The values $\tau_1 = 23.1$ fs and $\tau_2 = 195$ fs were found to yield the best fit [solid line in Fig. 2.9(a)] with measurements of the Raman gain spectrum [Fig. 2.9(b)] [174].

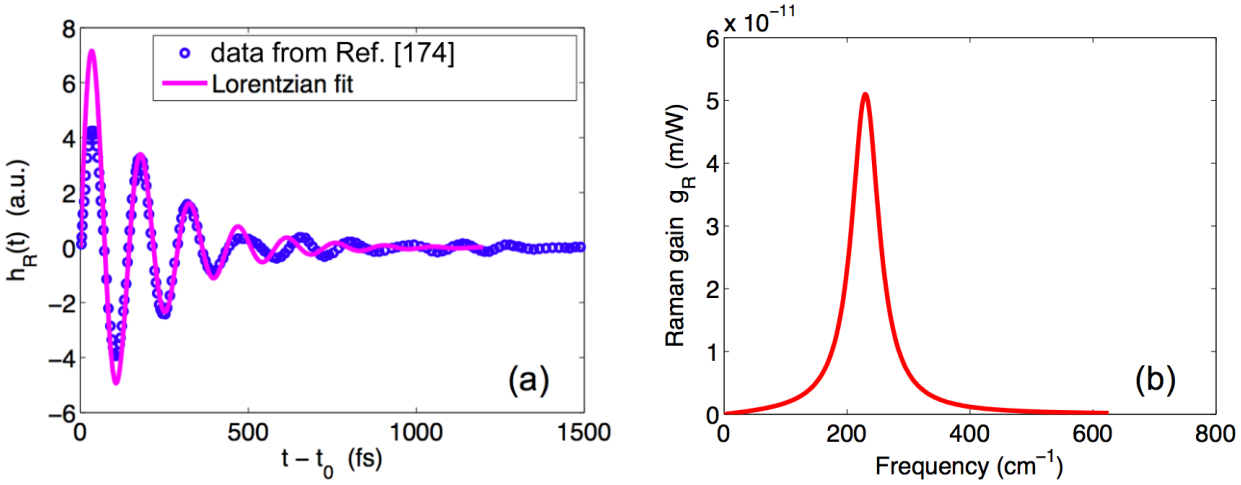

Figure 2.9 (a) Raman response function $h_R(t)$ of bulk As_2Se_3 glass, and (b) the corresponding Raman gain spectrum ($g_R(\Delta\omega)$) measured at pump wavelength λ=1.54 μm. Adapted from [99].

The Raman gain spectrum $g_R(\Delta\omega)$ [shown in Fig. 2.9(b)] was calculated from the definition $g_R(\Delta\omega) = 8\omega_0 n_2 f_R \,\mathrm{Im}[\tilde{h}_R(\Delta\omega)]/(3c)$ where $\mathrm{Im}[\tilde{h}_R(\Delta\omega)]$ is the imaginary part of the Fourier transform of $h_R(t)$. The scalar value f_R represents the fractional contribution of the Raman response to the total nonlinear response defined as: $R(t) = (1 - f_R)\cdot\delta(t) + f_R \cdot h_R(t)$, where the first term accounts for the instantaneous electronic response. We note in Fig. 2.9(b) that the peak gain coefficient ($g_R^{\max} = 5.1\times10^{-11}$ m/W) is located at the frequency shift of 229.3 cm^{-1} which is in quantitative accord with experimental measurements [82]. Moreover, we calculated a fractional contribution of $f_R = 0.115$, which is in close agreement with the value $f_R = 0.1$ reported in [174]. The characteristic Raman time constant T_R in Eq. (2.5), is defined as the first moment of the nonlinear response function, and is approximated as [4]:

$$T_R \equiv \int_0^\infty t \cdot R(t)\,dt \approx f_R \int_0^\infty t \cdot h_R(t)\,dt \tag{2.7}$$

On substituting Eq. (2.6), along with the relevant parameters, into Eq. (2.7) we found a value of $T_R = 5.40$ fs which we implemented in ensuing simulations of the NLSE. In that regard, we performed SC simulations by numerically solving the NLSE [Eq. (2.5)] using the *split-step Fourier method* (SSFM), and implementing the first *m* = 10 Taylor series coefficients (β_m) of the propagation constant $\beta(\omega)$ as defined in Eqs. (1.7)-(1.8). Taking a 10 cm long microporous fiber with (Λ = 0.40, d_{hole} = 0.24)μm as a case example, for which the fundamental mode is guided in a slightly *anomalous* dispersive regime ($D = 5.6$ ps/(km·nm)) has an effective mode area of $A_{\text{eff}} = 11$ μm^2 and a nonlinear parameter of $\gamma = 571$ W^{-1}km^{-1} at the λ=10.5 μm pump wavelength. The simulated temporal widths of the input pulses are restricted to the short pulse regime ($100\text{ fs} \le T_{\text{FWHM}} \le 10\text{ ps}$) in which we excite high-order solitons $N_{\text{sol}} > 5$ [definition of N_{sol} in Eq. (1.11)]. In this regime, the phenomenon of SCG is mainly driven by an initial SPM-driven nonlinear temporal compression of the pulse, accompanied by the creation of higher-order solitons and their successive fission into N_{sol} fundamental solitons via intrapulse Raman scattering. Each N_{sol} fundamental solitons ejected by the fission process have peak powers given by $P_s = P_0\left(2N_{\text{sol}} - 2s + 1\right)^2 / N_{\text{sol}}^2$ where P_0 is the peak input pulse power, and *s* = 1, 2,..., N_{sol} denotes the order in which they are ejected from the higher-order soliton [9]. The parameter P_s is of prime importance since it is the most energetic fundamental soliton which is mainly responsible for the generation of *dispersive waves* – also known as Cherenkov radiation [66] – that produces new frequencies (during the process of SCG).

2.1.6 Simulations of supercontinuum generation

In the first set of SSFM simulations [Fig. 2.10(a)], the input Gaussian pulse energy ($E_0 \cong 0.94 P_0 T_0$) was kept fixed at 0.9 nJ with varying T_{FWHM} pulse durations: 10, 1 and 0.1 ps (where $T_{\text{FWHM}} = T_0 2\sqrt{\ln 2}$). Conversely in the second simulation set [Fig. 2.10(b)], the pulse duration was kept fixed at $T_{\text{FWHM}} = 1$ ps while the seed energy (E_0) was varied: 0.2, 2.0 and 5.0 nJ.

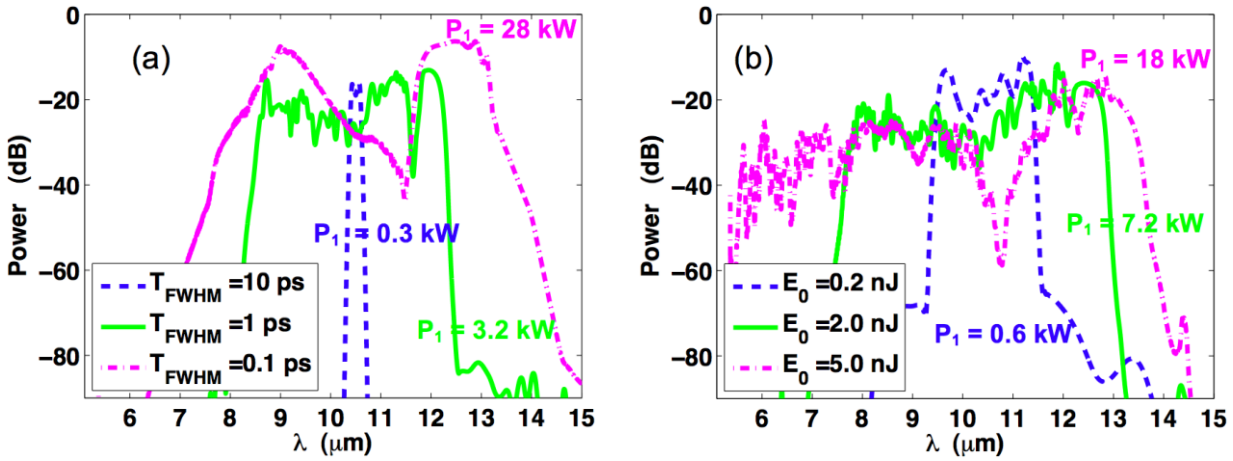

Figure 2.10 Output supercontinuum spectra calculated via SSFM in a microporous fiber with parameters (Λ=0.40, d_{hole}=0.24)μm, L=10 cm and for (a) E_0=0.9 nJ fixed seed energy with varying FWHM pulse durations (0.1, 1, 10) ps, and (b) for fixed pulse duration $T_{FWHM} = 1$ ps and varying seed energies (0.2, 2.0, 5.0) nJ. The peak power (P_1) of the first ejected fundamental soliton created by the fission of the N_{sol}-th order soliton, is shown alongside its corresponding curve. Reprinted from [99] with permission from The Optical Society of America.

In Fig. 2.10(a), for the simulation with pulse energy E_0 = 0.9 nJ and duration T_{FWHM} = 10 ps, the calculated soliton fission length in the fiber is L_{fiss} = 50 cm (where $L_{fiss} = L_D / N_{sol}$, see Eq. (1.11) for definition of dispersion length: L_D) which is significantly longer than the actual length L = 10 cm of the fiber: $L_{fiss} >> L$. Hence for this case, the soliton fission dynamics are minimal, thus resulting in small spectral broadening.

For input pulses of E_0 = 0.2 nJ and duration T_{FWHM} = 1 ps in Fig. 2.10(b), although the fission length is in theory short enough (L_{fiss} = 3.3 cm < L) to excite solitons along the fiber, the reason for the small spectral broadening in this case resides in the peak solitonic power (P_1 = 0.6 kW) which is *too low* to significantly activate the soliton fission process and subsequent dispersive waves generation.

On the other hand the output spectra corresponding to input pulses yielding large peak solitonic powers (P_1 > 2 kW), present considerably broadened spectra showing an intricate multi-peak structure along with a finer structuring related to Raman scattering and soliton fission processes [9, 10]. The broadest and un-segmented SC spectrum (calculated from -20 dB below peak output power) was obtained with the 0.9 nJ pulse of 1 ps duration (yielding L_{fiss} = 1.57 cm and P_1 = 3.2 kW), and had a bandwidth of approximately 3100 nm (between 8.5 and 11.6 μm).

2.1.7 Conclusions

In this contribution, a novel type of microstructured optical fiber for the mid-infrared spectrum was proposed. The *chalcogenide microporous fiber* with subwavelength holes provides extended chromatic dispersion engineering capabilities via precise tuning of its constitutive geometrical parameters (N, Λ and d_{hole}). While the present study concentrates on small-diameter porous-core fibers with $N = 4$ layers of holes, we emphasize that this type of waveguide could also be suited for the design of large mode area fibers (LMA) where typically $N >> 4$. The proposed microporous geometry is a simple design ready to be implemented using current MOF fabrication techniques.

The results presented in this work clearly demonstrated the potential of dispersion-tailored microporous fibers for nonlinear-phase matching applications and for supercontinuum generation. In particular, for geometrical parameters $\Lambda = 0.40$ μm and $d_{hole} = 0.24$ μm, numerical simulations of the nonlinear Schrodinger equation theoretically predicted a broad SC bandwidth of 3100 nm extending from 8.5 μm to 11.6 μm generated in a 10 cm long As_2Se_3 chalcogenide microporous fiber pumped with 0.9 nJ picosecond pulses at 10.5 μm wavelength.

The tunable dispersive and attenuating properties of microporous fibers promise to enhance the design freedom of linear and nonlinear mid-infrared optical devices.

2.2 Extreme nonlinear optical enhancement in chalcogenide glass fibers with deep-subwavelength metallic nanowires

2.2.1 Introduction

The previous Sub-section [2.1] showed how the core porosity of a fiber provides an additional degree of freedom which one can exploit to engineer the chromatic dispersion of the waveguide, towards the creation of a single (or multiple) ZDP(s) suitably located for phase-matching with nonlinear optical processes, including seeding a SCG. In this Sub-section, we explore the benefits as well as the caveats, of incorporating deep-subwavelength metallic features within the solid dielectric core of an emerging microstructured fiber (EMF).

In this regard, recent advances in micro and nanofabrication techniques have sparked vigorous research on EMFs with subwavelength features and using high-refractive-index compound glasses. In parallel, the intersection of plasmonics (i.e. *surface plasmons* [175]) with integrated optics has shown immense potential for sensing [176-180] and for the transmission [181-184] and modulation of optical signals on the subwavelength scale [185-189]. Different types of hybrid metallo-dielectric waveguides have been studied towards the efficient guiding of plasmonic modes [190-193], and more specifically light-guiding mediated by metallic nanowire arrays in optical fibers was investigated [163, 164; 194-196], and their potential for nonlinear plasmonics was mentioned in [194] but not studied in detail.

2.2.2 Motivations and geometry of proposed design

Here we propose a new type of nonlinear metallo-dielectric nanostructured optical fiber (NOF): the chalcogenide fiber with deep-subwavelength metallic inclusions. We demonstrate that the extreme field intensities, obtained at the sharp edges of the subwavelength metallic nanowires, enable giant nonlinear optical enhancements inside this hybrid chalcogenide–metal NOF. We further show that modal propagation losses are comparable to that of classical *surface plasmons polaritons* (SPPs) and thus only limited by the intrinsic absorption losses of the metal.

From a practical point of view, in the fabrication of a MOF comprising several dielectric rods (or capillaries) using the stack-and-draw procedure, the empty interstitial holes that can occur between adjacent rods are usually treated as unwanted defects [see examples in Fig. 2.11].

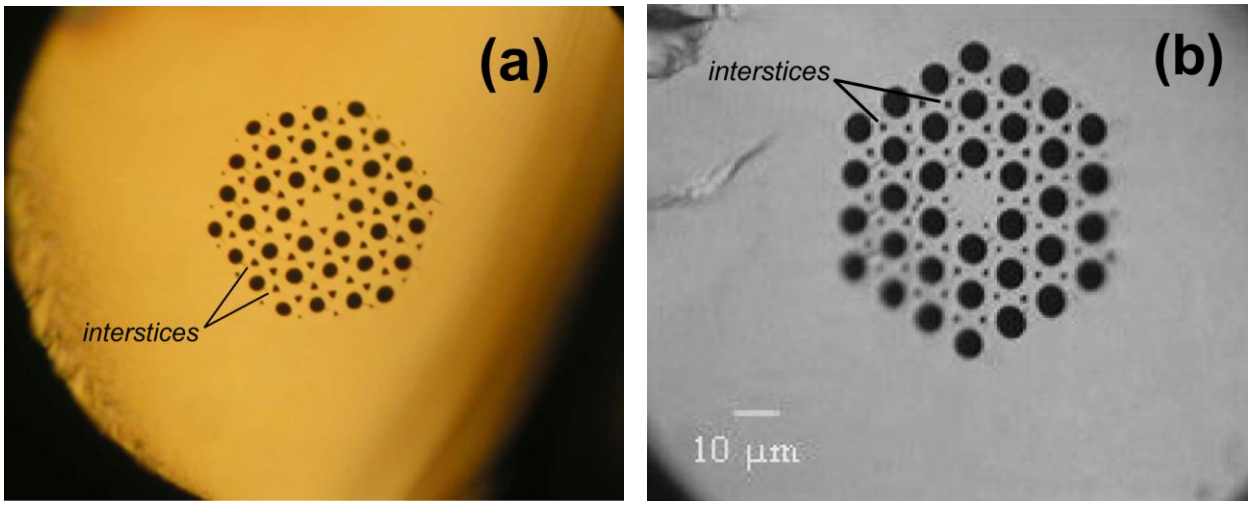

Figure 2.11 Micrographs of the cross-sections of (a) a chalcogenide Te-As-Se glass photonic crystal fiber with structural parameters (Λ=13.77, d_{hole}=6.14)μm (image adapted from [39]), and (b) a chalcogenide $Sb_{20}S_{65}Ge_{15}$ glass photonic crystal fiber with structural parameters (Λ=11.1, d_{hole}=4.7)μm (image adapted from [46]). We note the small empty interstices between the holes. Both images reprinted with permission from The Optical Society of America.

Here instead, we exploit these nanovoids by filling them with metal so as to generate a periodic array of triangle-shaped metallic nanowires, with a geometry analogous to so-called "bowtie" nanoantennas [197-199]. Coincidentally, the bowtie configuration is known to be very effective at yielding a prodigious concentration of electromagnetic fields inside the nanogap between two opposing apexes [200-203] (Example shown in Fig. 2.12).

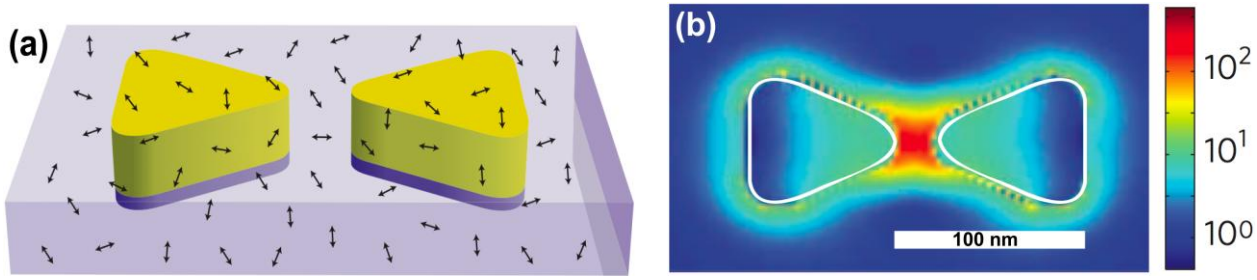

Figure 2.12 (a) Schematic of a gold bowtie nanoantenna on top of a transparent PMMA substrate (black arrows denote fluorescent molecules in suspension). (b) Vectorial finite-difference time-domain calculation of the local intensity enhancement at λ=780 nm. Adapted by permission from Macmillan Publishers Ltd: Nature Photonics (Ref.[200]), copyright (2009).

We thus here propose a radically new NOF design where the intense local fields enabled by metallic bowtie nanowires enhance the nonlinear light-matter interaction within the chalcogenide glass matrix, as shown in Figs. 2.13(c)-(d).

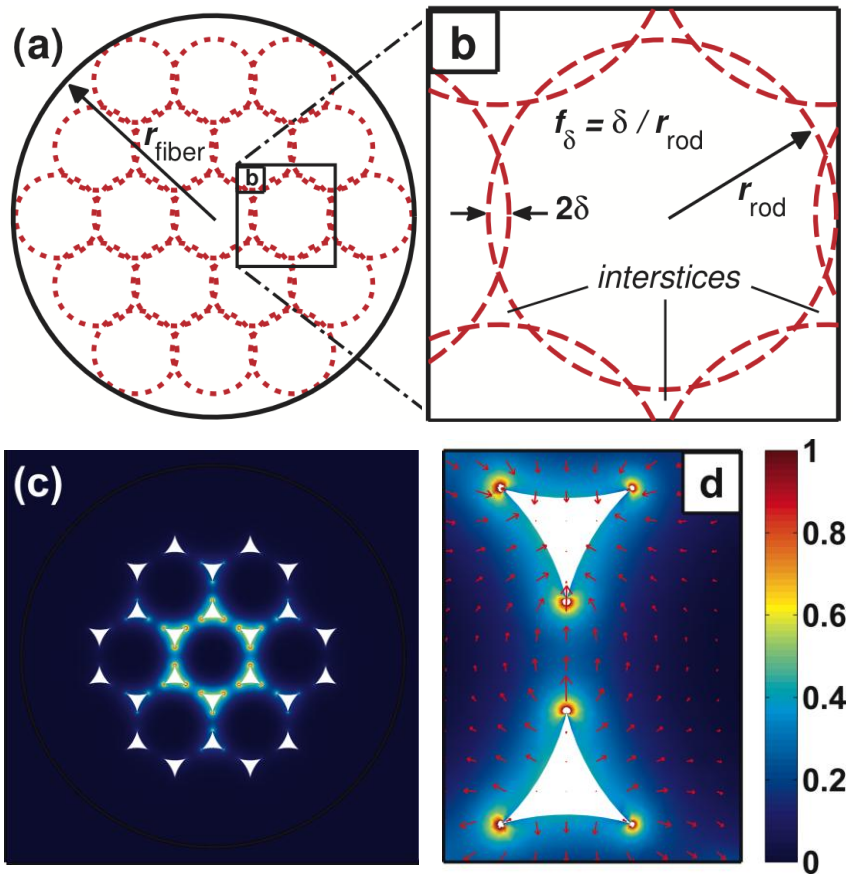

Figure 2.13 (a) Triangular lattice configuration of overlapping rods and small interstices with (b) a close-up view of the unit-cell geometry along with the relevant structural parameters. (c) S_z-power flux distribution of the fundamental plasmonic mode in the chalcometallic nanostructured fiber (r_{fiber} = 0.450 μm, f_δ = 0.03) at λ=3.0 μm, and (d) close-up view of a bowtie pair of nanowires showing the enhanced local fields in a.u. (arrows denote the vector *E*-fields). Reprinted from [100] with permission from The Optical Society of America.

Towards the fabrication of metal nanowires embedded in a dielectric matrix, a practical method was recently demonstrated in [204] (and later in [205]), where the authors used an iterative stack-and-draw technique to produce nanowires of progressively smaller sizes and having extreme aspect ratios. Thus a potential fabrication strategy of the proposed NOF is to first stack identical circular glass rods in a triangular lattice configuration within the preform, and then allow the touching rods to slightly overlap during the thermal softening and drawing process, as shown in Figs. 2.13(a)-(b). The ensuing small air interstices are then filled by pumping molten metal at high pressure, as demonstrated in [164, 194, 206]. This interstice-filling approach allows the precise edge-to-edge alignment of nanowire pairs to be enforced right from the initial macroscopic preform.

To simplify the theoretical analysis, the present investigation focuses on the case of N = 2 layers of rods (of equal radii r_{rod}) with gold-filled interstices. Nevertheless, the results and discussion presented thereafter provide the foundation for more complex chalco-metallic fibers (N > 2). In our model, the overlapping of rods is tuned by the "overlap half-distance" (δ) as defined in Fig. 2.13(b), and in practice, this is accomplished by controlling the injected gas pressure during drawing of the NOF. Here, we use the dimensionless parameter $f_\delta = \delta / r_{\text{rod}}$, where $f_\delta = 0$ denotes the case of tangent circles (i.e. no overlapping) while positive values $0 < f_\delta < f_{\delta,\,\max}$ controls the overlapping of adjacent rods up to a maximal ratio $f_{\delta,\,\max} = 1 - (1+1/3)^{-1/2} \simeq 0.134$ which represents the limit where the small interstices disappear (N.B. the $f_{\delta,\,\max}$ value was obtained by basic trigonometry). The total outer radius of the fiber is set to $r_{\text{fiber}} = 2N(r_{\text{rod}} - \delta) + (r_{\text{rod}} + \delta)$ such that the whole NOF geometry can be specified using only r_{fiber} and the "overlap factor" (f_δ), which was kept fixed at $f_\delta = 0.03$ in this study and corresponding to 2.8% by volume of metal content. We also note that the triangular shape of a nanowire enclosed by three tangent circles closely approximates that of a *deltoid* (i.e. a three-cusped hypocycloid), as depicted in Fig. 2.14 below. The size of the deltoid shape is characterized by the inscribed circle of radius: $r_{\text{del}} = \left(\sqrt{1+1/3} - 1\right) r_{\text{rod}} - \delta\sqrt{1+1/3}$, as defined in Fig. 2.14(b).

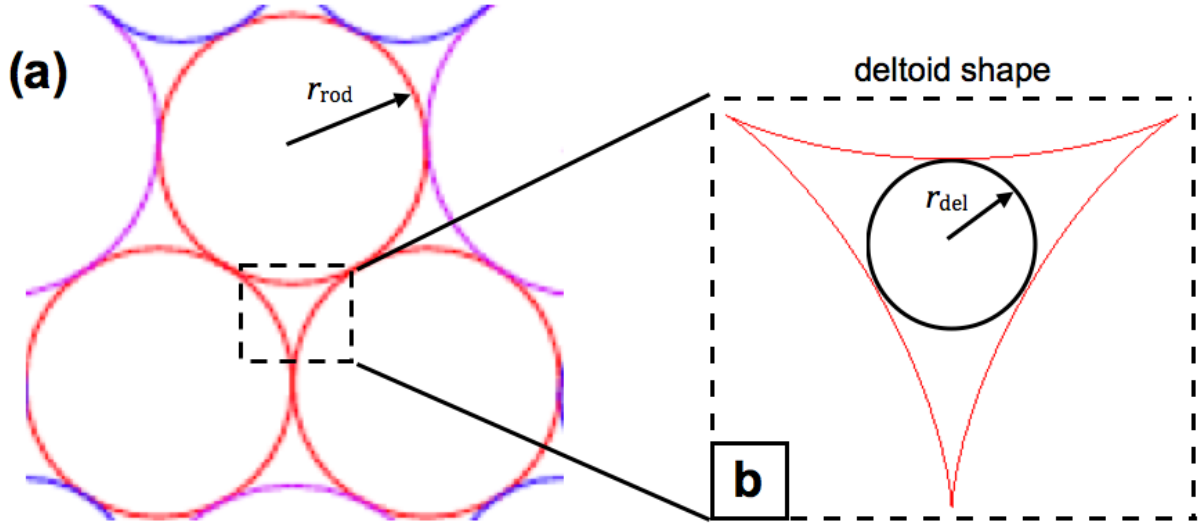

Figure 2.14 (a) Triangular lattice configuration of three tangent circular rods of identical radii (r_{rod}) and (b) a close-up view of the enclosed deltoid-shaped nanowire, along with the inscribed circle of radius (r_{del}).

The wavelength of interest in the present study is λ=3.0 μm, for which the permittivity of the gold metal is $\varepsilon^{\text{Au}} = -474 + i30.64$ and the nonlinear index is $n_2^{\text{Au}} = 1.32 \times 10^{-12}$ m^2/W [207]. The selected dielectric material was again As_2Se_3 chalcogenide glass due to its wide bulk transmission window in the mIR (2–14 μm) and its large nonlinearity: $n_2 = 1.1 \times 10^{-17}$ m^2/W.

2.2.3 Simulations of the subwavelength field confinement and the extreme nonlinear optical enhancement

As discussed in Chapter 1.1, there have been recent demonstrations of large nonlinear optical enhancement in HNLFs, and more specifically, in chalcogenide nanowires [89-92]. Therefore as a benchmark, we now compare the optical properties of our hybrid chalcogenide-metal NOF with the bare chalcogenide nanowire. Using full-vector FEM simulations, we solved for the fundamental HE_{11} mode guided in the bare As_2Se_3 nanowire and for the fundamental plasmonic mode [Fig. 2.13(c)] guided in the hybrid NOF, for various values of fiber radius (r_{fiber}). By comparing the bare nanowire with a hybrid NOF of the same size ($r_{\text{fiber}} = 0.32$ μm), one can appreciate the exceptionally strong transverse field confinement in chalco-metallic fibers [left inset in Fig. 2.15(a)]; while in the nanowire case, there is very significant power leakage into the surroundings [right inset in Fig. 2.15(a)].

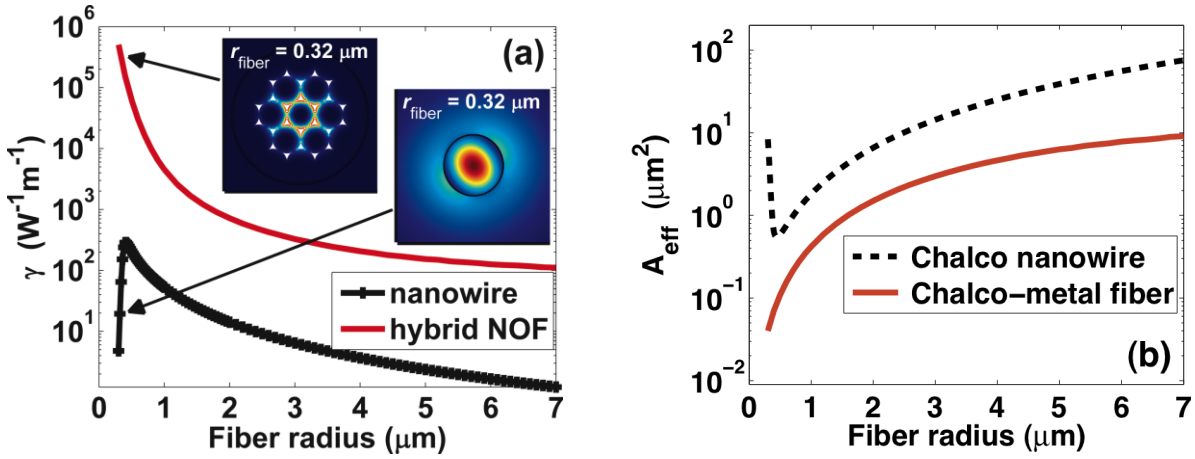

Figure 2.15 (a) Optical nonlinearity (γ) and (b) effective mode area (A_{eff}) of a bare chalcogenide nanowire and a hybrid chalco-metallic NOF at λ=3.0 μm as a function of the fiber radius. Reprinted from [100] with permission from The Optical Society of America.

Figure 2.15(b) plots the effective mode area (A_{eff}) [defined in Eq.(1.3)] and indicates that the chalco-metallic fiber consistently provides better field confinement over a chalcogenide nanowire

of the same size. In particular, one achieves a nearly ten-fold enhancement in field confinement for $r_{\text{fiber}} \geq 0.415\ \mu\text{m}$. In the case of $r_{\text{fiber}} < 0.415\ \mu\text{m}$, while the A_{eff} of a bare nanowire diverges to the entirely unguided limit ($A_{\text{eff}} \to \infty$ for $r_{\text{fiber}} \to 0$), the mode area supported by a hybrid NOF keeps shrinking with smaller radii of fiber [Fig. 2.15(b)]. This nanoscale localization of light beyond the diffraction limit is made possible by the plasmonic guiding in the metallic nanowire array.

The nonlinear parameter was also computed using its vectorial definition of Eqs. (2.1)-(2.2). Figure 2.15(a) indicates that the optical nonlinearity reaches a peak of $\gamma = 286\ \text{W}^{-1}\text{m}^{-1}$ at $r_{\text{fiber}} = 0.415\ \mu\text{m}$ for the bare nanowire; while at the same radius size the hybrid NOF provides $\gamma = 1.34 \times 10^5\ \text{W}^{-1}\text{m}^{-1}$ corresponding to a nonlinear enhancement factor of 468, over two orders of magnitude increase in nonlinearity at the given operation wavelength. In fact, the computed nonlinear enhancement factor in chalco-metallic fibers, compared to similar nanowires, is consistently greater than 50 across the investigated range of fiber radii.

2.2.4 Characterization of the modal propagation losses and discussion

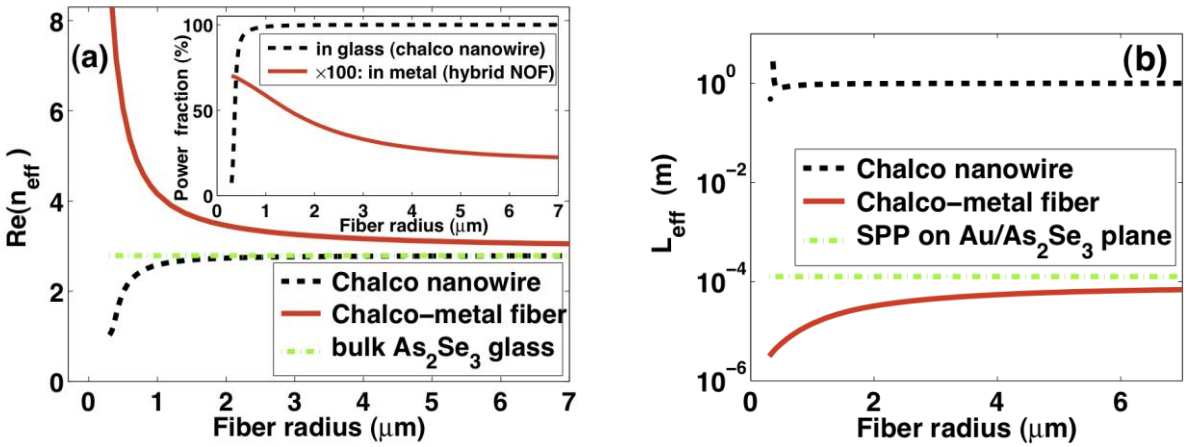

Figure 2.16 (a) Real effective refractive index (n_{eff}) and (b) effective propagation length (L_{eff}) of a bare chalcogenide nanowire and a hybrid chalco-metallic nanofiber at λ=3.0 μm as a function of the fiber radius. Inset in (a): fraction of power guided inside metallic regions for the chalco-metallic fiber (solid curve) and inside chalcogenide glass, for the nanowire (dashed curve). The n_{eff} and L_{eff} of a classical SPP on the gold–As_2Se_3 planar interface is also shown (green dot–dashed curve) for reference in (a) and (b) respectively. Reprinted from [100] with permission.

The real part of the effective refractive index $\text{Re}(n_{\text{eff}})$ and the effective propagation length $L_{\text{eff}} = c/[2\omega \cdot \text{Im}(n_{\text{eff}})]$ of both the chalcogenide nanowire and the hybrid NOF, as a function of fiber radius, are plotted in Fig. 2.16(a) and Fig. 2.16(b), respectively. As shown in the inset of Fig.

2.16(a), the fraction of guided power of the fundamental mode in the bare nanowire becomes more confined inside the chalcogenide glass matrix – and therefore less in the air cladding – as the fiber radius increases. Consequently we observe in Fig. 2.16(a) for the nanowire: $n_{\text{eff}} \to n_{\text{mat}}$ as $r_{\text{fiber}} \to \infty$, where $n_{\text{mat}} = 2.789$ at λ=3.0 μm for bulk As_2Se_3 glass. The contrary is also true in the unguided limit: the value of n_{eff} reaches the refractive index of air cladding such that $n_{\text{eff}} \to n_{\text{air}} = 1$ as $r_{\text{fiber}} \to 0$. On the other hand for the hybrid NOF, the value of n_{eff} increases with reduction of the fiber radius. The latter behavior can be understood by considering the fraction of power that propagates inside the metallic regions [solid curve in inset in Fig. 2.16(a)]. One must first bear in mind that the geometrical proportions of the fiber's internal nanostructure are preserved as the radius gets smaller. Hence for very small NOF radii ($r_{\text{fiber}} < 1\ \mu\text{m}$), the dimensions of the metallic nanowires become deeply subwavelength and comparable to the skin depth in metal, such that a significant fraction of guided power overlaps with the strongly dispersive and lossy metallic regions.

The last remark also explains the gradual lowering of L_{eff} in the hybrid NOF when $r_{\text{fiber}} \to 0$ as shown in Fig. 2.16(b). In particular, Fig. 2.16(b) indicates that the effective propagation length of the chalco-metallic NOF is asymptotically comparable in magnitude to that of a planar SPP whose effective refractive index is given by $n_{\text{eff}}^2 = \varepsilon_{\text{m}}\varepsilon_{\text{d}}/(\varepsilon_{\text{m}} + \varepsilon_{\text{d}})$, where ε_{m} and ε_{d} denote the complex dielectric constants of the metal and the adjacent dielectric respectively. This last observation highlights the fact that the fundamental mode of interest in the metallo-dielectric NOF represents a plasmonic mode created by all the "gap-plasmon" modes [e.g. Fig. 2.13(d)] supported by the array of bowtie nanowires. A notable feature here is that a reduction of r_{fiber} from 5.0 to 0.5 μm translates into lowering the L_{eff} value of the hybrid NOF by a factor of 10 [Fig. 2.16(b)], while simultaneously enhancing its nonlinearity by a 400-fold factor [Fig. 2.15(a)]. In order to alleviate the large plasmonic losses, the incorporation of optical gain via dipolar dopants in the dielectric host (e.g. dye molecules, silicon nanocrystals, and quantum dots) has demonstrated some success [184, 208], and more on this topic will be discussed in Chapter 4.1.

2.2.5 Conclusions

In this Section, a novel type of NOF was proposed. Our theoretical calculations demonstrated that the *hybrid chalcogenide–metal nanostructured optical fiber* provides an attractive platform for

achieving nanoscale mode area nonlinear light–matter interactions. Thus the proposed chalcometallic fibers are relevant for studying extreme nonlinear light–matter interactions for all-optical signal processing and highly-integrated nanophotonic devices in general. It also broadens the scope of both conventional and exotic physical phenomena, which could be studied through the use of micro-(nano-)structured optical fibers.

CHAPTER 3 : EMERGING MICROSTRUCTURED POLYMER FIBERS FOR TERAHERTZ WAVEGUIDING

This Chapter describes the experimental results and theoretical analysis of the *hollow-core Bragg fibers* fabricated with high-refractive-index composite materials [Chapter 3.1], and of the *suspended core subwavelength dielectric fibers* [Chapter 3.2]. I outline the motivations behind the design of suspended core subwavelength dielectric fibers, and how this design partly solves some critical problems that currently hinders practical THz waveguiding. But first, I will present the outcomes of a theoretical and numerical study on the influence of the concentration of (high-refractive-index / high-loss) additives within a polymer host, on the photonic bandgaps (in other words: the fiber transmission windows) of hollow-core Bragg fibers. The numerical results are analyzed and put into the context of actual samples fabricated in our research labs.

3.1 High-refractive-index composite materials for terahertz waveguides: trade-off between index contrast and absorption loss

3.1.1 Introduction

As highlighted in Chapter 1.2, the chief obstacle for realizing low-loss terahertz waveguides stems from the fact that most materials exhibit large absorption losses inside the THz spectrum. A solution found to partly overcome this problem was to design either hollow-core or highly porous waveguides, or subwavelength solid-core waveguides, in all of which a substantial portion of the optical power is guided in dry air. The present study focuses on the hollow-core Bragg fiber, which can support spectrally broad transmission windows (i.e. large bandgaps) when using two dielectrics with high-refractive-index (hRI) contrast in the periodic reflector surrounding the fiber core. In this regard, there is a strong incentive to develop hRI materials to enable THz waveguides and components that operate on the principles of the photonic bandgap.

In this work, we demonstrate that increasing the concentration of subwavelength-size microparticles inside a polymer host not only elevates the refractive index of the resulting composite dielectric material (which is a desirable feature); but also significantly raises the absorption losses (an undesirable feature). We also present experimental optical characterizations of the doped-polymer films and the hollow-core Bragg fiber fabricated by our group (i.e. A.

Dupuis, K. Stoeffler, and C. Dubois; all from Ecole Polytechnique de Montréal). The analysis reveals that for the design of efficient THz Bragg fibers – and Bragg photonic bandgap devices in general – a balance between the strength of the refractive index contrast and rising material losses must be found; otherwise high losses may completely suppress the fiber bandgaps.

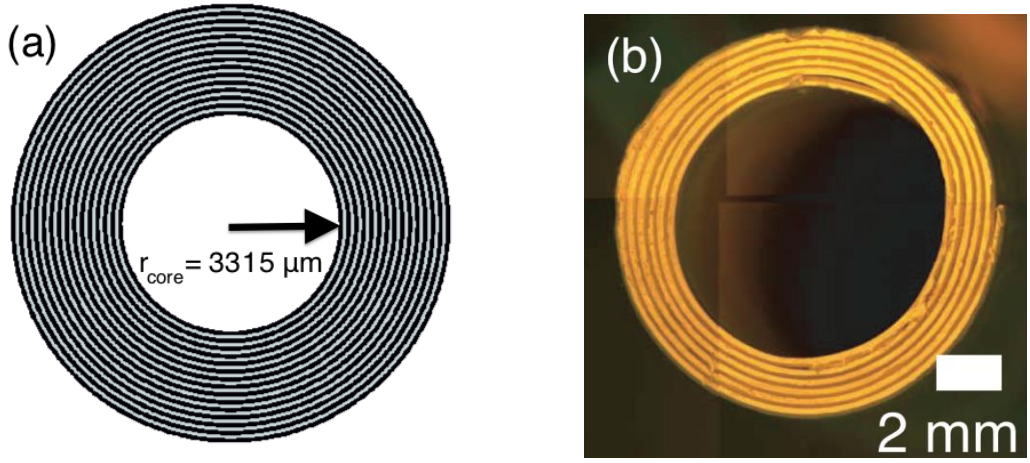

Figure 3.1 Hollow-core Bragg fiber with the reflector made of alternating hRI TiO_2-doped PE layers and low-index pure PE layers. (a) Structure with 14 bilayers used in the T-matrix calculations. (b) Bragg fiber with five bilayers fabricated using a combination of film extrusion, hot pressing, and subsequent coiling. Reprinted from [151] with permission from The Optical Society of America.

3.1.2 Geometry of the hollow-core Bragg fibers

In this regard, losses occurring inside a periodic dielectric reflector decrease exponentially with the number of bilayers. Hence, the larger the number of bilayers, the lower are the losses and *clearer* are the bandgaps. However in practice it is only possible to simulate a finite number of bilayers. So in order to clearly illustrate the theoretically achievable bandgaps in a Bragg fiber, in our numerical calculations we assume a perfectly circular-symmetric Bragg fiber of core diameter $d_{\text{core}} = 6.63\ \text{mm}$, composed of 14 bilayers [Fig. 3.1(a)] created by the periodic wrapping of hRI titania-doped polyethylene (PE) and low-refractive-index undoped PE films, of respective thicknesses $d_{\text{H}} = 135\ \mu\text{m}$ and $d_{\text{L}} = 100\ \mu\text{m}$. These values correspond exactly to the hollow-core size and layer thicknesses measured in the fabricated rolled-up Bragg fiber [Fig. 3.1(b)]. Because of the fragility of the strongly TiO_2-doped layers, the fabrication process currently remains challenging, and thus we successfully produced only five bilayers in the actual 22.5 cm long Bragg fiber.

3.1.3 Optical characterization of the titania-doped polymer composites

Prior to this work, hRI materials in the terahertz range have been demonstrated by incorporating hRI subwavelength-size particles within a host polymer [209-211]. Similarly in this work, we utilize the doping of linear low-density PE with high-index rutile titanium dioxide (TiO_2) microparticles of varying concentrations in order to enhance and control the composite material's refractive index and absorption coefficient.

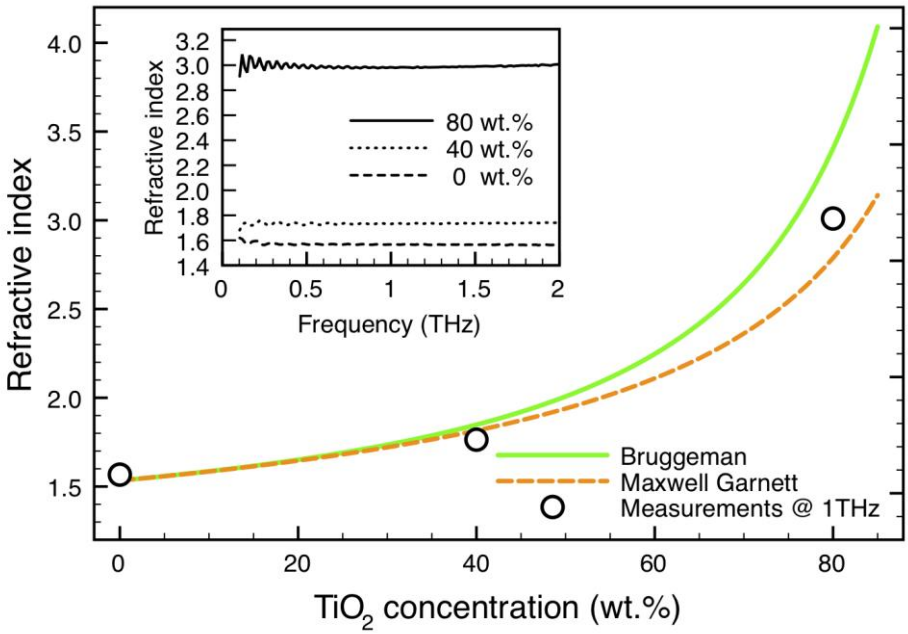

Figure 3.2 Refractive index of a PE-based polymer compound as a function of weight concentration of TiO_2 particles: Bruggeman model fit (solid curve) [see Eq. (3.1)] and measurements at 1 THz frequency (circles). Inset: THz-TDS measurements of the refractive index for pure PE (dashed curve), 40 wt.% (dotted curve), and 80 wt.% (solid curve) TiO_2 doping. Reprinted from [151] with permission from The Optical Society of America.

Terahertz time-domain spectroscopy (THz-TDS) transmission measurements performed on the fabricated TiO_2-doped and undoped PE films showed that the refractive index of the polymer compounds remained practically constant throughout the 0.1–2.0 THz range (inset of Fig. 3.2). The refractive index of the PE-TiO_2 polymeric compound was well fitted with Bruggeman's effective medium approximation which is valid for spherical doping particles [211]:

$$1 - f_V = \frac{\varepsilon_p - \varepsilon_m}{\varepsilon_p - \varepsilon_h} \sqrt[3]{\frac{\varepsilon_h}{\varepsilon_m}} \tag{3.1}$$

where f_V is the volumetric particle fraction ($0 < f_V < 1$) of the doping particles, and ε_p, ε_h, and ε_m denote the respective permittivities of the dielectric particles, host, and mixture. Contrary to the Maxwell–Garnett (MG) effective medium model which is only valid for dilute volume concentrations ($f_V < 15$ vol.%) of spherical particles within the host material; the Bruggeman mixing model extends the validity domain of the MG approach towards higher concentration of dopants by taking into account the distinct interactions of the two-phase composite medium. We measured for the host pure-PE: $\varepsilon_h = 2.455$ (or $n_h = 1.567$). The utilized permittivity of pure rutile titanium dioxide (TiO_2) is $\varepsilon_p = 109.96$ as measured in [211]. Small discrepancies between the model [Eq. (3.1)] and the measurements in Fig. 3.2 can be explained by noting that samples displayed significant inhomogeneity at high doping concentrations, and that the TiO_2 grade used (DuPont, Ti-Pure® R-104) contains up to 3 wt.% of impurities. The simple relation $f_V = f_W \big/ \left(f_W + (1 - f_W)\rho_p / \rho_h \right)$, where ρ_p and ρ_h denote the respective mass densities of the doping particles and the host, was used for converting a weight fraction f_W of particles into a volume fraction f_V. The density of the PE polymer provided by the manufacturer (Nova Chemicals, SCLAIR® FP120-A grade) is $\rho_h = 0.920$ g/cm^3 and that of rutile TiO_2 is $\rho_p = 4.2743$ g/cm^3.

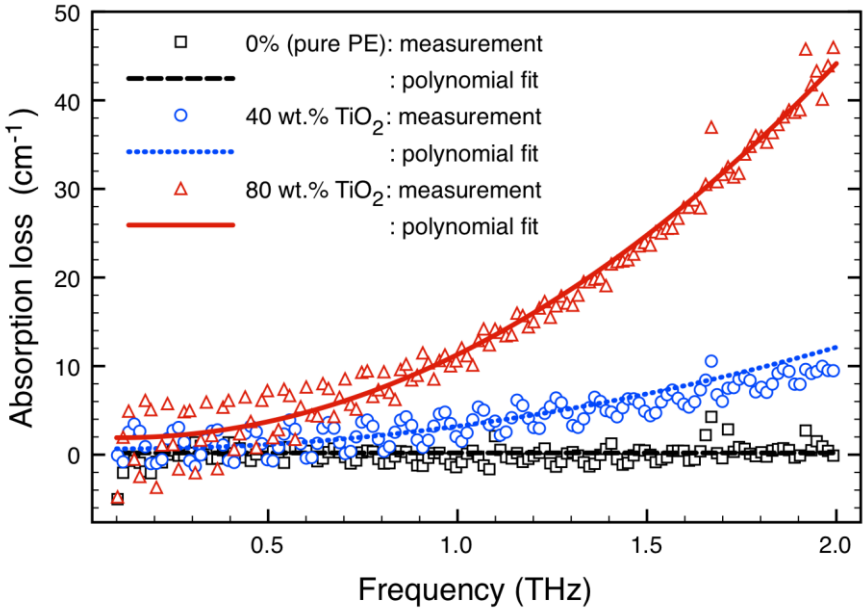

Figure 3.3 Power absorption loss of the doped PE-based polymer compound as a function of frequency (THz) for various levels of TiO_2 doping concentrations: 0 wt.% (pure PE), 40 wt.%, and 80 wt.%. Squares, circles, and triangles denote THz-TDS measurements, while the dashed, dotted and solid curves represent the corresponding polynomial fits [see Eq. (3.2)]. Reprinted from [151] with permission from The Optical Society of America.

In Fig. 3.3, the THz-TDS measurements of the absorption loss of doped compounds exhibit a sharp quadratic increase with frequency in doped compounds. The bulk material loss coefficient (α_m) in cm^{-1} of a TiO_2-doped PE composite was here empirically modeled as a function of the volumetric doping fraction (f_V) and input frequency (ν) via a second-order polynomial fit:

$$\alpha_m = f_V\left(a_1\nu^2 + a_2\nu + a_3\right) + a_4 \quad [cm^{-1}], \quad \nu = [THz] \tag{3.2}$$

For our TiO_2-PE compound, the best-fit coefficients are $a_1 = 25.5$, $a_2 = -5.5$, $a_3 = 4.0$, and $a_4 = 0.2$. Coefficient a_4 actually defines the measured baseline absorption of undoped PE, which rapidly oscillates (due to Fabry–Perot effects in planar samples [11]) about an average value of 0.2 cm^{-1} inside the range of 1.0–2.0 THz.

3.1.4 Vectorial simulations of the modal properties in doped Bragg fibers

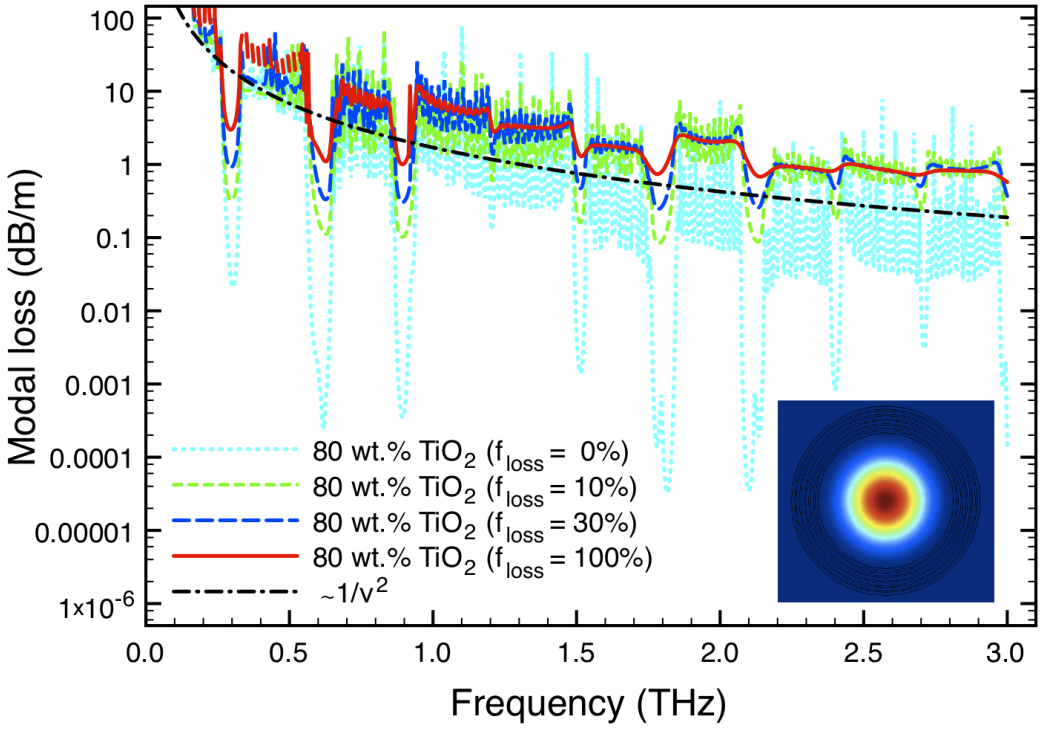

Figure 3.4 Fundamental mode loss in doped-PE/PE hollow-core polymer Bragg fibers (14 bilayers) as a function of input frequency and for various levels of fractional nominal loss (f_{loss}) inside the dielectric layers. Inset: calculated fundamental mode power profile at 1 THz. Reprinted from [151] with permission from The Optical Society of America.

Pertaining to the waveguiding of THz light in Bragg fibers built from a combination of doped and pure PE films, we assume a linearly polarized THz source for coupling light into the hollow core fiber, thus predominantly exciting modes with angular momentum $m = 1$ (HE_{1n} and EH_{1n} modes). The attenuation coefficient of the lowest-order fundamental HE_{11}-like mode was computed using a vectorial transfer-matrix (T-matrix) mode solver [212] and assuming hRI layers of $n_{\mathrm{m}} = 2.985$, corresponding to $f_{\mathrm{W}} = 80$ wt.%. And in order to systematically elucidate the detrimental effect of the reflector's material loss on the Bragg fiber transmission, we present the HE_{11} modal losses for various values of the hRI material loss [in Fig. 3.4]. Specifically, we vary in our simulations the loss of a composite material from zero (i.e. the ideal case) up to its nominal (and maximal) value set by Eq. (3.2) via $\alpha_{\mathrm{hRI}} = f_{\mathrm{loss}}\alpha_{\mathrm{m}}$ where $0 \le f_{\mathrm{loss}} \le 1$. The cyan dotted curve in Fig. 3.4 corresponds to a doped Bragg fiber with *no* absorption losses ($f_{\mathrm{loss}} = 0$ %) in the bilayers. This idealized configuration reveals 10 distinct bandgaps inside the 0.1–3.0 THz range, with the widest one being the fundamental bandgap centered at 0.3 THz. For frequencies inside the bandgaps, the HE_{11} optical mode is tightly confined within the hollow core and thus guided with very low attenuation [see inset of Fig. 3.4].

For frequencies outside of the bandgaps however, a substantial fraction of guided power is present in the dielectric reflector layers, and we observe that the fiber transmission is a highly oscillatory function of frequency [see for example, the 0.35–0.50 THz region in Fig. 3.4]. This oscillatory behavior can be explained by noting that for frequencies outside of the bandgaps, the multilayer reflector stack can be viewed as a single thick dielectric tube. As discussed in Chapter 1.2, such tubes are known as ARROW fibers or capillary waveguides [147, 148], and they exhibit periodic drops and rises in their transmission spectrum with a period inversely proportional to the tubular walls' thickness [Eq. (1.13)].

3.1.5 Discussion on the trade-off between index contrast and absorption losses in doped Bragg fibers

From our analysis of Fig. 3.4 we isolate the two main effects of the material absorption on the transmission properties of the fundamental HE_{11} mode in a Bragg fiber. First, we notice that for frequencies outside of bandgaps, the elevated material loss leads to a flattening of the rapid oscillations in the modal loss curve. The explanation is that large material losses cause strong attenuation of the outgoing traveling waves inside the reflector over the transverse section of the

tubular wall thickness. The second observation is that low-loss HE_{11} transmission within bandgap regions persists even for relatively high material losses (dashed green, long-dashed dark blue, and solid red curves in Fig. 3.4). We note that for frequencies within the bandgaps, the modal fields decay exponentially fast into the reflector region, thus field penetration is typically limited to the first few bilayers.

The creation of bandgap in a Bragg fiber transmission spectrum is actually due to destructive interference of counterpropagating waves within several reflector bilayers closest to the core/reflector interface. Intuitively, in order to destroy spatial interference over a distance of a few bilayers, much higher material losses are required than those needed to disrupt spatial interference over a distance of a much thicker capillary wall. It is thus unsurprising to find that bandgap guidance can still persist, even for high material losses for which leaky modes due to anti-resonances in the capillary walls are already suppressed. This indicates that, in principle, the bandgap guiding mechanism in Bragg fibers is more resilient to material losses than ARROW fibers (or capillaries). In the limit of very high material loss, spatial interference within the first few reflector layers vanishes; instead, the Bragg fiber guides solely due to Fresnel reflections at the inner air/reflector interface [red solid curve in Fig. 3.4 for $\nu > 2$ THz]. In these conditions, the Bragg fiber actually behaves as a bore waveguide with a characteristic $\alpha \propto 1/\nu^2$ attenuation dependence with frequency.

To further examine the combined effects of the elevation of the refractive index and material losses with increasing doping concentration on the bandgaps, we computed the theoretical HE_{11} mode attenuation spectrum between 0.8 and 1.2 THz for an ideal (perfectly circular) Bragg fiber made of 5 bilayers whose layer thicknesses (d_H and d_L) were suitably chosen to obey the *quarter-wave condition*, $d_H \tilde{n}_H = d_L \tilde{n}_L = \lambda_c/4$, at grazing angle of incidence (θ = 89°) of a planar reflector [213-214] so as to maximize the bandgap size around a center wavelength of interest λ_c (in this case, λ_c corresponds to $\nu_c = 1$ THz), where $\tilde{n}_i = \sqrt{n_i^2 - n_c^2 \sin^2\theta}$, and n_c denotes the refractive index of the hollow core. The results depicted in Fig. 3.5 first indicate that the minimum HE_{11} loss (~ 0.3 dB/m) in this ideal Bragg fiber is obtained at low TiO_2 doping concentrations (~ 10 wt.%); however larger band gaps along with relatively low losses can be found at very high concentration levels (~ 85 wt.%). Between these two far opposite regimes of doping, we identify a much less interesting and intermediary zone, roughly between 30–70 wt.%, that offers limited bandgap size and substantially larger attenuation losses. What we conclude from Fig. 3.5 is that

one can obtain very wide bandgaps using high-loss and high-refractive-index composite materials; but the trade-off is in the form of an increase of the achievable minimum attenuation value (i.e. *trough* of the bandgap) compared to a similar low-loss low-index-contrast Bragg fiber.

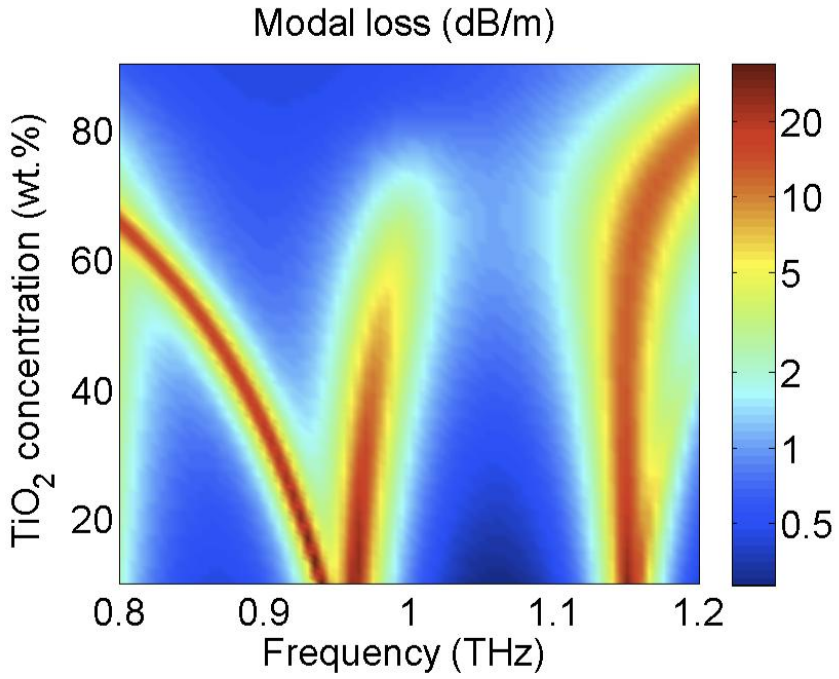

Figure 3.5 Fundamental mode loss (dB/m) as a function of TiO_2 doping concentration of high-index layers and frequency, for an ideal Bragg fiber (five bilayers) whose reflector layer thicknesses are tuned to obey the quarter-wave condition near the center frequency 1 THz. Reprinted from [151] with permission from The Optical Society of America.

We also investigated the effect of the spiral shape of a rolled Bragg fiber [inset of Fig. 3.6] on the modal transmission properties of the fiber. We compare in Fig. 3.6 the losses of a fundamental HE_{11} core mode as computed using the T-matrix method, versus the results of a finite-element method (FEM) simulation of the corresponding and more realistic spiral structure (dashed green and dotted blue curves, respectively). We see in Fig. 3.6 that the inner step defect of the actual spiral-shaped Bragg fiber had only a minor effect, since the two numerical approaches yield very similar modal loss curves. The FEM calculations [dotted curve in Fig. 3.6] of the propagation losses indicate that the hollow-core's broken symmetry created by the small step defect results in a slight (~ 0.05 THz) blue-shift of some peaks of radiation loss located near the blue end of the THz range, where the dimension of the light wavelength becomes close to that of the step defect.

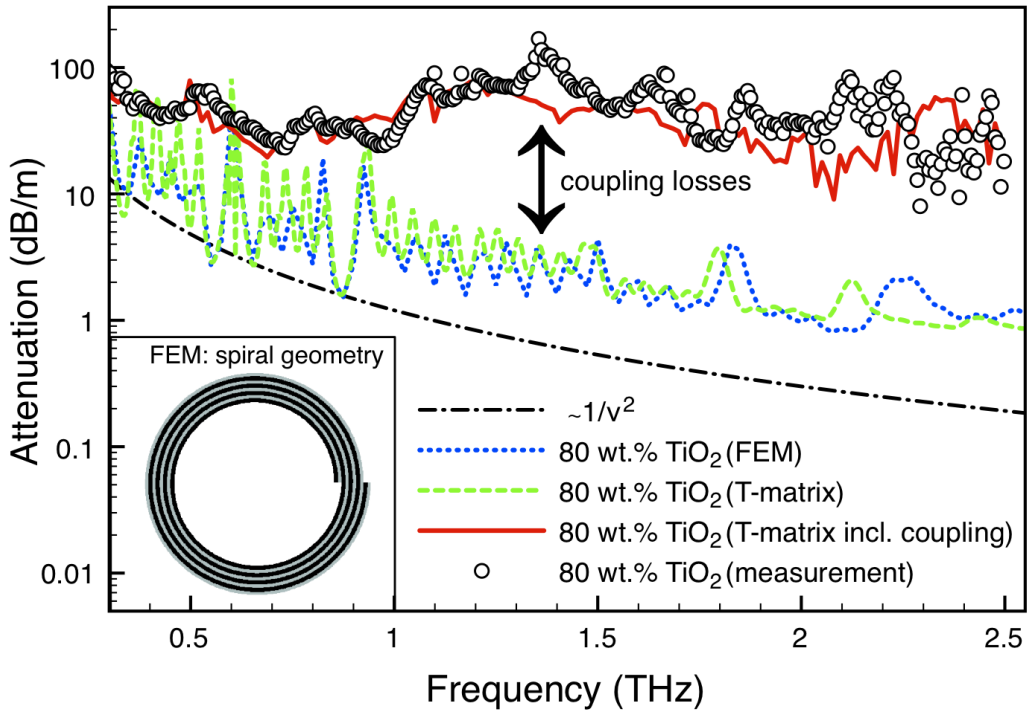

Figure 3.6 Fundamental mode loss (dB/m) in 80 wt.% doped Bragg fiber (five bilayers) computed by the T-matrix method (dashed curve) with perfect circular symmetry, and via the FEM (dotted curve) with the spiral shape defect (shown inset). THz-TDS measurements of total attenuation (open circles), and theoretical calculations including coupling losses and intermodal interference effects (solid curve). Reprinted from [151] with permission from The Optical Society of America.

Figure 3.6 also presents the THz-TDS measurements (open circles) of the total loss of the fabricated Bragg fiber [shown in Fig. 3.1(b)]. The actual total fiber loss includes not only the transmission loss, but also the input and output coupling losses. Moreover the fiber is multimode, therefore in order to provide a correct theoretical prediction of the exprimental results, we must include the intermodal interference effects and the frequency-dependent coupling losses into consideration. We account for intermodal interference effects by calculating the output transmission at the end of the Bragg fiber using the respective modal absorption coefficients and effective indices of the HE_{11} and the second lowest-loss HE_{21} mode. A standard frequency-dependent estimate of the *coupling efficiency* (or in other words, the "coupling losses") was obtained by using the overlap integral of the input Gaussian field with that of the HE_{11} (and HE_{21}) mode field as computed in [126]:

$$\eta_{\text{mode}}^{\text{coupling}}(\nu) = \frac{\left| \int_{\text{total}} dA \cdot E_{\text{input}}(\nu) \cdot E_{\text{mode}}(\nu) \right|^2}{\int_{\text{total}} dA \cdot \left| E_{\text{input}}(\nu) \right|^2 \cdot \int_{\text{total}} dA \cdot \left| E_{\text{mode}}(\nu) \right|^2} \tag{3.3}$$

The results of simulations taking into account intermodal effects and coupling losses [red solid curve in Fig. 3.6] agree on the scale and the overall behavior with the experimentally measured results.

3.1.6 Conclusions

In summary in this Sub-section, we have theoretically and experimentally investigated the performance of photonic bandgap Bragg fibers using hRI terahertz materials based on doped polymeric compounds. As discussed in Chapter 1.2, current state-of-the-art THz waveguides exhibit losses just below the 1 dB/m level. Our numerical calculations predict that propagation losses below 0.3 dB/m in doped-polymer Bragg fibers are theoretically achievable. However, it is difficult to demonstrate such a low attenuation directly in our experiments due to the coupling losses and the intermodal interference effects. Our detailed analysis of the hollow-core Bragg fibers has revealed that large absorption losses induced by a high concentration of dopants can effectively destroy the bandgap confinement mechanism of the periodic reflectors made from such compounds, even when material combination with a very hRI-contrast is used. This finding is important for the design of THz optical components, especially Bragg fibers / mirrors / filters, based on hRI composite materials.

3.2 Suspended core subwavelength fibers: towards practical designs for low-loss terahertz guidance

3.2.1 Introduction

Among the several designs of low-loss waveguides for the terahertz that have recently been proposed [see review in Chapter 1.2], the *subwavelength dielectric fiber* presents definite advantages: it supports a single HE_{11} mode that provides easy and efficient coupling to a linearly polarized Gaussian-like beam emitted from a terahertz dipole antenna, and offers a large fraction of power that is guided outside the lossy dielectric material and within low-loss air (due to highly delocalized modal fields). The main disadvantages of *subwavelength dielectric fibers* are their relatively small bandwidth (which is limited towards high frequencies due to onset of large material absorption losses, and limited at low frequencies by scattering losses), and the fact that the highly delocalized fields strongly couples with the surrounding environment thus making subwavelength fibers difficult to manipulate (and to support via holders) without disrupting the propagating THz signal. Moreover, the actual use of subwavelength fibers generally requires a bulky gas-purged enclosure to minimize the resonant absorption lines of ambient water vapor on the measured THz spectra.

3.2.2 Geometry of proposed design

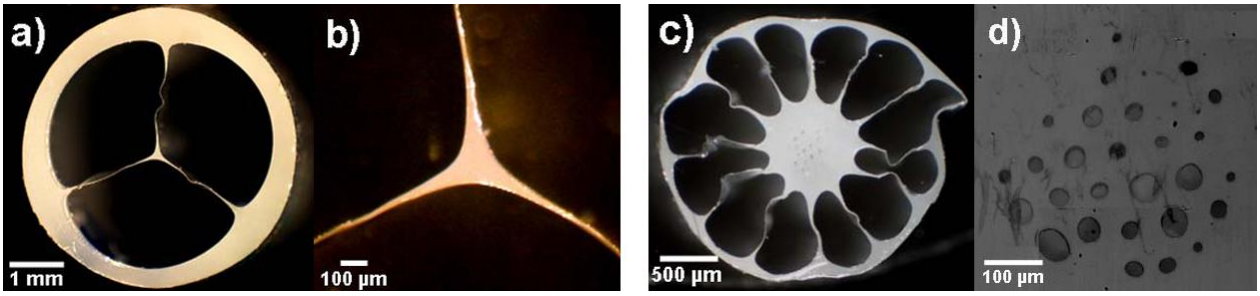

Figure 3.7 (a) Cross-section of the suspended solid core fiber (OD = 5.1 mm), and (b) close-up view of the suspended solid core region (d_{core} ~150 µm). (c) Cross-section of the suspended porous core fiber (OD = 3 mm), and (d) close-up view of the suspended large porous core (d_{core} = 900 µm). Reprinted from [139] with permission from The Optical Society of America.

In this work, we present the analysis of two *suspended core dielectric fibers* that partly solves the above-mentioned problems towards practical terahertz waveguiding. The proposed

fiber design [in Fig. 3.7] incorporates a subwavelength-diameter core suspended inside a large porous outer cladding filled with dry air (or another low-loss gas). We show that the purpose of the porous cladding is two-fold. First, it effectively isolates the core-guided mode from interacting with the surrounding environment, thus preventing undesirable external perturbations to affect the terahertz signal waveform. Secondly, it serves as a natural air-tight enclosure for the fiber core, thus avoiding the need for an externally purged housing.

3.2.3 Optical characterization of the polyethylene polymer, and fabrication of the suspended core dielectric fibers

All the polymer-MOFs presented in this work were fabricated using commercial rods of low-density polyethylene (PE) known to be one of the lowest loss polymers in the terahertz region [see Fig. 1.5(b) and discussion therein]. The refractive index and absorption coefficient of this specific grade of PE were characterized by THz-TDS (detailed description of setup in [137, 149]) using a 1.5 cm thick PE slab with polished parallel interfaces [see Fig. 3.8].

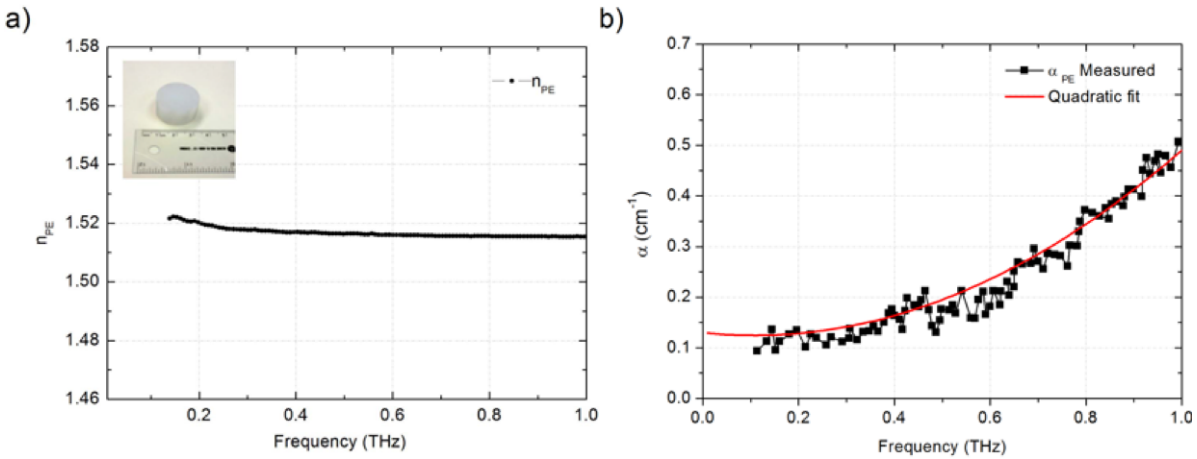

Figure 3.8 (a) Refractive index and (b) bulk material losses of polyethylene (PE) in the frequency range 0.10 – 1 THz as measured by THz-TDS. The inset picture in Fig.(a) shows the PE slab used for the measurements. Reprinted from [139] with permission from The Optical Society of America.

The determined refractive index [Fig. 3.8(a)] remains largely constant between 0.10 and 1.00 THz and equal to n_{PE} = 1.514. Power absorption losses (in cm^{-1}) of the PE polymer increase quadratically as a function of frequency [Fig. 3.8(b)] and can be fitted with Eq. (3.2) using $f_V = 1$ and coefficients: $a_1 = 0.46$, $a_2 = 0.10$, $a_3 = 0.13$, and $a_4 = 0$. In particular, the absorption losses reach 0.2 cm^{-1} at 0.5 THz and about 0.5 cm^{-1} at 1 THz.

The preform of the suspended *solid core* fiber [Fig. 3.7(a)-(b)] was obtained by drilling three holes of 4 mm diameter, equidistantly spaced by 2 mm and centered on a one-inch diameter PE rod. The preform was then drawn under gas pressure into a fiber of OD = 5.1 mm and a suspended core of $d_{\text{core}} \sim 150$ μm in size. The whole cross-section of the solid suspended core fiber is presented in Fig. 3.7(a), with an enlarged view of the core region in Fig. 3.7(b).

The other type of suspended dielectric fiber that we investigated presents a large *porous core* suspended by 12 thin bridges. This MOF was fabricated using a combination of drilling and stacking techniques. Capillaries of 0.8 mm inside diameter (ID) and 1.2 mm outside diameter (OD) were first drawn under pressure from initial PE tubes of ID = 10 mm and OD = 25.4 mm. Resulting capillaries were then stacked into a hexagonal lattice of 3 rings and solidified in a furnace. The stack of capillaries was then inserted in the middle of a large PE tube presenting 12 holes of 3 mm diameter in its periphery. After pressure-controlled drawing, we obtained a fiber of OD = 3 mm with a porous core of approximately 900 μm in diameter suspended in the middle of the holey cladding. The structure of the porous core shows a random array of longitudinally-running holes ranging from 20 μm to 70 μm in diameter, yielding a porosity of approximately 4%. The whole cross-section of the fiber is presented in Fig. 3.7(c) and a detailed view of the microstructured porous core is in Fig. 3.7(d).

3.2.4 Terahertz near-field imaging setup for the characterization of the modal properties in the suspended core dielectric fibers

We now turn to the investigation of the principal guiding mechanisms in these MOFs. Specifically, we expect that guidance by these fibers to stem from a combination of single-mode guidance inside the subwavelength core, rapidly decaying cladding modes, and anti-resonant guiding by the tube of finite thickness. Therefore the main task is to find out what are the excitation conditions that lead to one or the other propagation regime. To accomplish this task we used *near-field imaging* at the fibers output facet to directly probe the modal composition in these fibers [215-216].

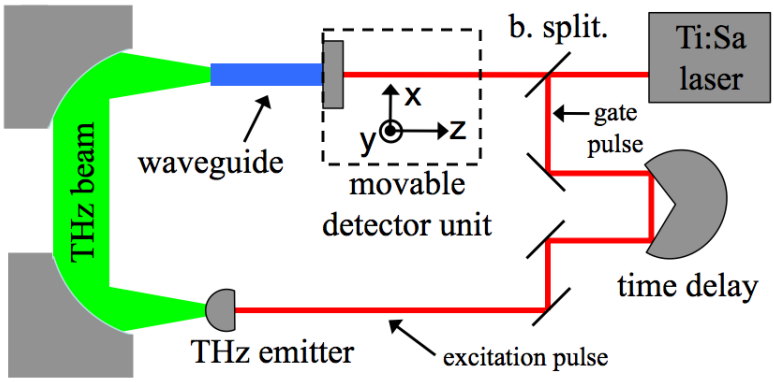

Figure 3.9 Schematic of the THz near-field microscopy setup used for fiber mode profiling.

Near-field images of the output field profiles in both fibers were obtained using a terahertz near-field microscopy system based on the implementation of photoconductive antennae acting first as the coherent E_x–polarized THz pulsed source and as a near-field probe [Fig. 3.9]. A detailed description of the setup and experimental procedure used by our collaborator, Prof. Markus Walther (Freiburg University) who performed the measurements, can be found in [217, 218]. The time-domain near-field microscopy allows recording of the temporal evolution of the electric field in close proximity (<30 μm) to the output facet of a fiber sample excited by a broadband THz pulse, with sub-picosecond temporal precision and subwavelength spatial resolution ($\sim\lambda/20$). After Fourier transform of the time-domain data, frequency-dependent near-field images of the fibers in the 0.01–1.00 THz range were retrieved. Taking the *z*-axis as the direction of propagation in the waveguide, two-dimensional profile maps (*x*-*y* distribution) of the transverse E_x-field were obtained via raster scanning of the fiber cross-section by the probe detector, yielding a 60×60 pixels resolution in a 6×6 mm^2 area which covered the whole output facet of our fibers. By rotating the polarization-sensitive detector by a 90° angle allows further mapping of the E_y-field component.

3.2.5 Comparison between the experiments and simulations of the output modal field distributions

To understand the principal guiding mechanisms in these fibers, one has to recognize a somewhat complex modal structure in these waveguides. Thus, even if propagation in the suspended core is typically single-mode, the fiber can also support a variety of leaky cladding modes. Then if the excitation beam is large enough – which is definitely the case at low frequencies – one should

expect contributions from both core modes and cladding modes in the total transmission of the fiber.

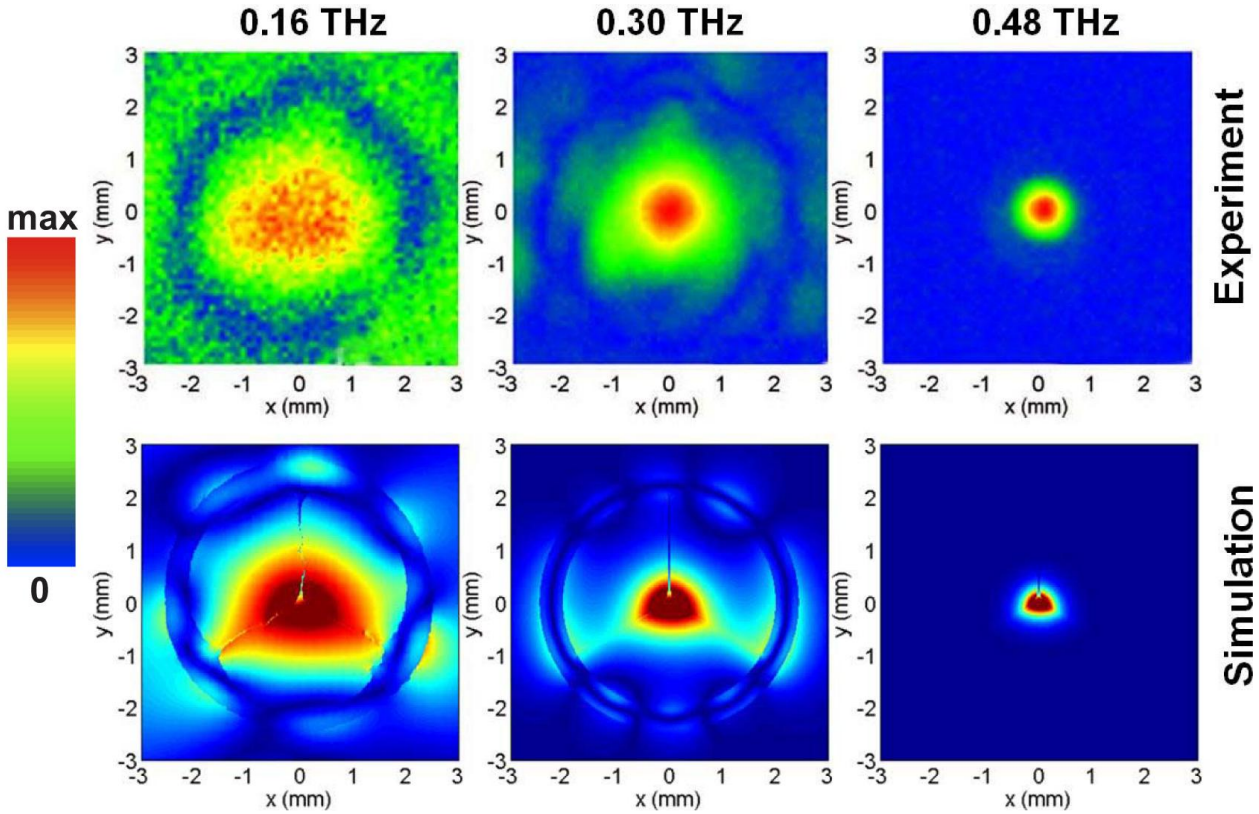

Figure 3.10 Near-field microscopy images (top row) and corresponding simulations (bottom row) of the output $|E_x|$-field profile of the suspended small solid core fiber at 0.16, 0.30 and 0.48 THz. Reprinted from [139] with permission from The Optical Society of America.

In Fig. 3.10 we present the $|E_x|$-field output profiles at selected frequencies as measured experimentally (top row) and as computed numerically (bottom row) using vectorial FEM, for the case of the small suspended core fiber [Fig. 3.7(a)-(b)]. From these images one can distinguish two regimes of propagation. The first regime is anti-resonant guidance at 0.16 THz where the fiber acts as a capillary tube (i.e. ARROW fibers). In that regime the modal fields are strongly delocalized and extend far away from the suspended core, such that guiding mechanism is essentially dictated by the Fabry-Pérot anti-resonant conditions in the tube cladding of finite thickness. Correspondingly one notices in Fig. 3.13(a) a narrow transmission peak at 0.16 THz due to the anti-resonant field confinement [shown in Fig. 3.10] at that frequency. The second propagation regime observed in Fig. 3.10 represents the main regime of interest where the field is confined by the central solid core and guided by total internal reflection as illustrated by the

output profiles at 0.30 THz and 0.48 THz. One also notes that these guided modes are located inside the main low-loss propagation window (as given by the cut-back measurements) [Fig. 3.14(a)] spanning the range between 0.28 and 0.48 THz. Moreover, the near-field profiles in Fig. 3.10 indicate that transmission occurs in an *effectively-single-mode* regime; in other words, the HE_{11}-like core-guided mode is dominant. So as expected, field confinement becomes stronger as the frequency increases such that for $\nu > 0.50$ THz a large fraction of power propagates within the lossy solid core, thus explaining the steep increase of propagation losses thereafter [see Fig. 3.14(a)].

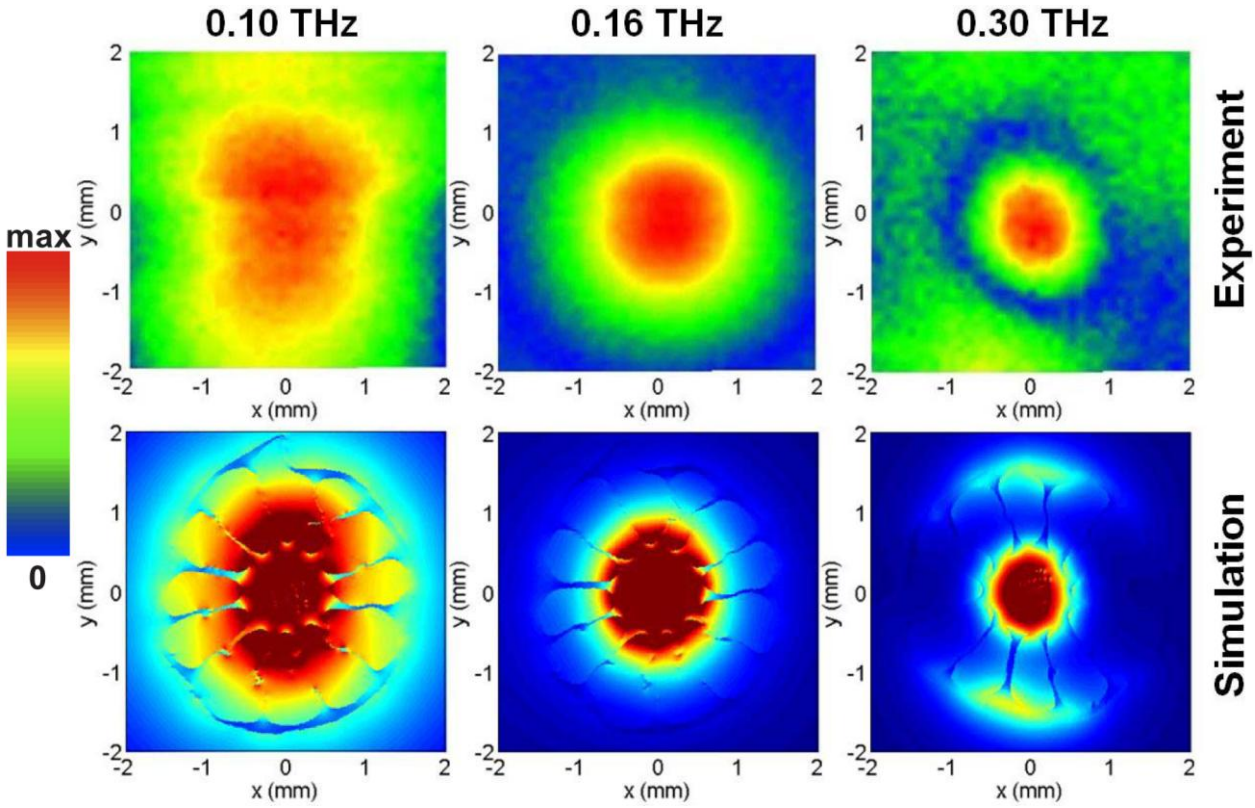

Figure 3.11 Near-field microscopy images (top row) and corresponding simulations (bottom row) of the output $|E_x|$-field profile of the suspended large porous core fiber at 0.10, 0.16 and 0.30 THz. Reprinted from [139] with permission from The Optical Society of America.

Figure 3.11 shows the $|E_x|$-field distributions at the output facet of a large suspended porous-core fiber at selected frequencies. One observes a similar behavior – as previously described for the suspended small solid core fiber – albeit shifted towards lower frequencies. In particular, at low frequencies (close to 0.10 THz) the field is highly delocalized and extends in the microstructured holey cladding (filled with low-loss air), thus enabling attenuation values smaller

than the bulk material loss [Fig. 3.14(b)]. For frequencies larger than 0.16 THz, most of the power propagates within the large porous core thus leading to an increase in the attenuation loss due to material absorption. Modal confinement in the fiber core becomes stronger at higher frequencies, thus explaining the rapid decline in transmission above 0.20 THz [see Fig. 3.13(b)].

In our simulations, the distribution of the transverse *E*-field components, $\mathbf{E}^{\text{output}} = (E_x^{\text{output}}, E_y^{\text{output}})$, at the output facet of a waveguide of length *L* is modeled as the coherent superposition of *N* guided modes (including both core and cladding modes):

$$\mathbf{E}^{\text{output}}(\omega) = \sum_{m=1}^{N} C_m \cdot \mathbf{E}^m(\omega) \cdot \exp\left[i \frac{\omega}{c} (n_{\text{eff}}^m L) \right] \cdot \exp\left[-\frac{\alpha^m L}{2} \right] \tag{3.4}$$

where $\mathbf{E}^m = (E_x^m, E_y^m)$ stands for the transverse field components of the *m*-th guided mode. The variables α^m and n_{eff}^m denote respectively the power loss coefficient and the real part of the complex effective refractive index ($\tilde{N}_{\text{eff}}^m = n_{\text{eff}}^m + i\alpha^m c/2\omega$) of the *m*-th mode at the given angular frequency $\omega = 2\pi\nu$. The variable C_m refers to the normalized amplitude *coupling coefficients* computed from the overlap integral of the respective flux distributions of the *m*-th mode and that of the input Gaussian beam [125]:

$$C_m = \frac{1}{4} \int \left[E_x^{\text{input},*}(x,y) \cdot H_y^m(x,y) + E_x^m(x,y) \cdot H_y^{\text{input},*}(x,y) \right] \cdot dx\, dy \tag{3.5}$$

where the electromagnetic fields of each *m*-th mode are normalized to carry unit power in the *z*-direction via $F \Big/ \sqrt{\tfrac{1}{2} \int \text{Re}(E_t \times H_t^*) dx\, dy}$, where *F* denotes electromagnetic field vector component. Since the probe antenna is placed directly at the fiber output facet, the use of output coupling coefficients is not required.

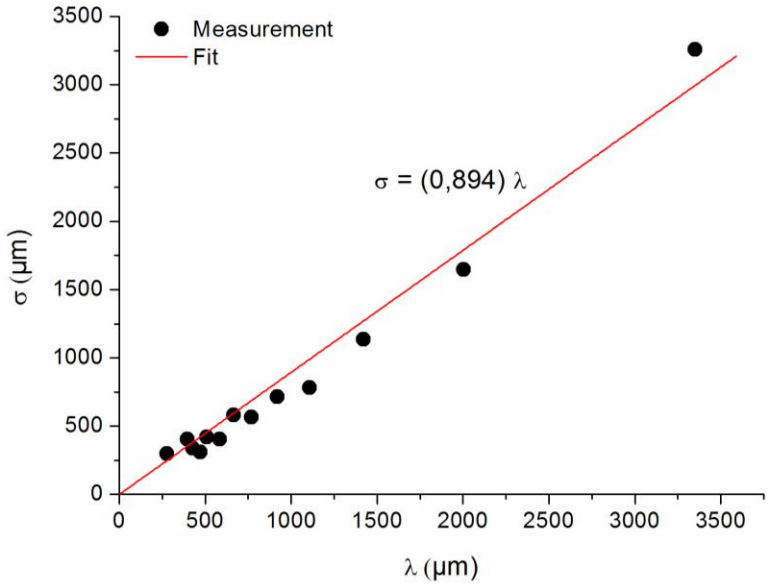

Figure 3.12 Gaussian beam waist parameter (σ) as a function of input wavelength, as measured with the THz near-field microscopy setup (dots), and modeled by a linear fit (solid line). Reprinted from [139] with permission from The Optical Society of America.

To model the input source of power *P*, we assume an *x*-polarized Gaussian beam whose fields are normalized via $E_x^{\text{input}}(x,y) = \hat{x} \cdot \sqrt{2P/\pi\sigma^2 n_{\text{clad}}} \cdot \exp\left[-(x^2+y^2)/2\sigma^2\right]$ and $H_y^{\text{input}}(x,y) = \hat{y} \cdot \sqrt{2n_{\text{clad}}P/\pi\sigma^2} \cdot \exp\left[-(x^2+y^2)/2\sigma^2\right]$ where the Gaussian beam waist parameter (σ) is related to the full-width half-maxima value through $\text{FWHM} = 2\sigma\sqrt{2\cdot\ln 2}$, and n_{clad} denotes the refractive index of the cladding medium. The frequency dependence of the beam waist was separatly measured by near-field microscopy, and the data was fitted to a linear function of the input wavelength [Fig. 3.12], $\sigma = (0.894)\lambda$, which was subsequently used in our numerical simulations. A finite-element method (FEM) code was used to calculate the modes of both fibers. To perform such simulation, we first imported the fiber cross-section geometries (as captured by the optical microscope in Fig. 3.7) into COMSOL Multiphysics® FEM software, and then solved for the complex effective refractive indices (N_{eff}^m) and field profiles of the *m*-th modes (both core and cladding modes) in Eq. (3.4). We simulated *N*=12 modes for the suspended small solid core fiber, and *N*=8 modes in the case of the suspended large porous core fiber.

3.2.6 Fiber output transmission and propagation losses: results and discussions

Next, the transmission characteristics of both fibers [Fig. 3.13] were measured using the same THz near-field imaging setup [in Fig. 3.9]; except this time the near-field probe was *not* scanned across the whole output facet area of the fiber. Instead, the probe remained positioned at a fixed location above the center (x_0, y_0) of the core on the output side. We note that the latter approach for measuring fiber transmission loss is somewhat different from a traditional one that measures the total power coming out of the whole fiber cross-section. Particularly, by placing the near-field probe at the fiber center during cutback measurements, one preferentially measures losses of the few lowest-order modes. This is related to the fact that such modes have their intensity maxima in the vicinity of the fiber core, thus providing the dominant contribution to the total transmission. In the case of a few modes fiber, the latter method preferentially measures the loss of the fundamental HE_{11} mode. We also note that the recorded transmission spectrum is sensitive to the exact (x_0, y_0) location of the near-field probe, especially at higher frequencies for which the guided mode becomes more tightly confined in the core region such that a slight position offset of the probe with respect to the actual peak field amplitude can significantly lower the detected signal. A similar remark can be made regarding the exact location of the incident Gaussian beam focus spot on the input cross-section. Both effects partly explain the discrepancies at higher frequencies between experiments and simulations in Fig. 3.13. Particularly in the case of the porous core fiber's simulated transmission spectrum [Fig. 3.13(d)] we notice a shoulder for frequencies above 0.20 THz compared to measurements [Fig. 3.13(b)]. To better understand this behavior, we performed additional simulations (not shown here for sake of brevity) where the positioning of the incident beam spot was shifted by $\Delta x_0 = x_0' - x_0 = 150$ μm with respect to the core's cross-section center (x_0, y_0), and subsequently observed a significant lowering of the shoulder behavior.

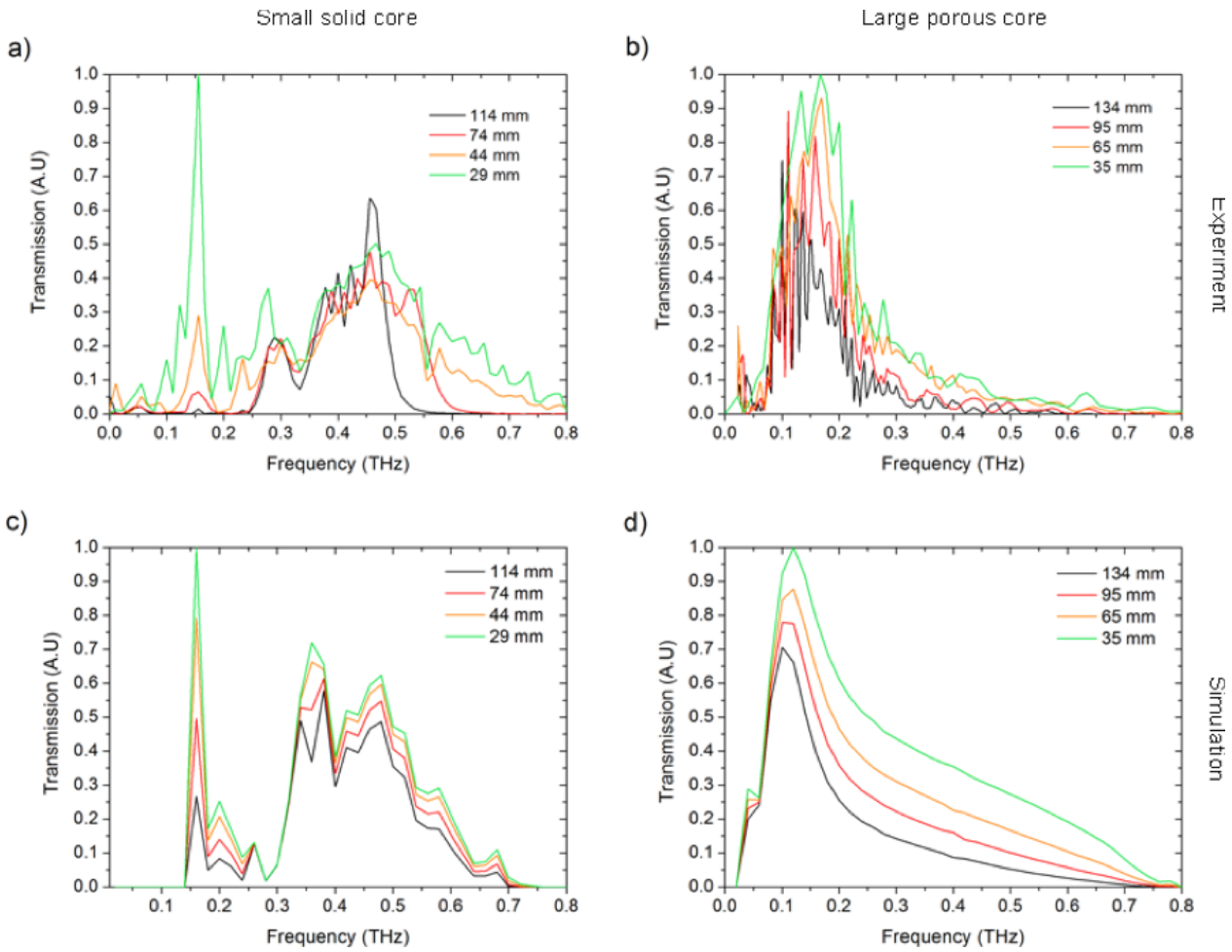

Figure 3.13 Transmitted $|E_x|$-field as measured by the near-field THz-TDS probe between 0.01 and 0.80 THz for various lengths of (a) suspended small solid core fiber, and (b) suspended large porous core fiber. Corresponding numerical simulations of the amplitude transmission through the (c) suspended solid core fiber, and (d) the suspended porous core fiber. Reprinted from [139].

Using Eq. (3.4) we derive an expression for the each fiber's transmission (T_{fiber}) as estimated from the transmitted $|E_x|$-field measured by the near-field probe located at (x_0, y_0) :

$$T_{\text{fiber}}(\omega) \cong \left|\mathbf{E}^{\text{output}}(x_0, y_0, \omega)\right| = \left|\sum_{m=1}^{N} C_m \cdot \mathbf{E}^m(x_0, y_0, \omega) \cdot \exp\left[i\frac{\omega}{c}(n_{\text{eff}}^m L)\right] \cdot \exp\left[-\frac{\alpha^m L}{2}\right]\right| \qquad (3.6)$$

In Fig. 3.13(a) and Fig. 3.13(b) we present the experimentally-measured transmission spectra for different lengths (L) of the *suspended solid core fiber* and the *suspended porous core fiber*, respectively. The corresponding simulated transmission spectra of both fibers – as modeled with Eq. (3.6) – are presented respectively in Fig. 3.13(c) and Fig. 3.13(d). We first note that the measured transmission spectra are well reproduced by the numerical simulations. We observe

that terahertz transmission through the suspended small solid core fiber covers the 0.25–0.51 THz region. A notable feature in the measured transmission spectrum [Fig. 3.13(a)] is the sharp transmission peak located at 0.16 THz. This peak is attributed to the coupling of the Gaussian excitation beam to the cladding and surface modes that are prevalent at low frequencies. This remark can be confirmed directly by looking at the near-field image of the output field profile of Fig. 3.10 at 0.16 THz. We also note that cladding modes exhibit high propagation losses due to their strong confinement inside the thick and lossy cladding region, and that surface modes also exhibit high losses due to their evanescent nature, thus explaining their rapid exponential decline with the fiber's length (L).

In the case of the suspended large porous core fiber [Fig. 3.13(b)], we first note a transmission window that is narrower compared to the small solid core fiber. Specifically for the longest fiber L = 134 mm, frequencies between 0.10 and 0.27 THz are effectively guided by such a fiber with a peak transmission near 0.13 THz, which is also reproduced by the numerical modeling [Fig. 3.13(d)]. One also notices that the transmission abruptly drops at frequencies higher than 0.33 THz corresponding to a wavelength of 900 μm, a dimension that matches the diameter of the porous core. The sharp transmission drop at higher frequencies can be explained by strong confinement of the guided modes inside the lossy core. This rationale is also supported by the near-field images of the guided modes [in Fig. 3.11] which clearly confirm that for frequencies below 0.30 THz the field is significantly delocalized and extends into the low-loss air cladding; while for frequencies above 0.30 THz the modal fields remains primarily confined inside the porous core. Moreover, some fringe oscillations are visible in the measured transmission spectrum of the suspended porous core fiber [Fig. 3.13(b)]. These oscillations are not caused by interference of higher-order modes (or cladding modes) with the fundamental mode. Instead, these closely spaced spectral oscillations represent residual noise stemming from the application of the discrete Fourier transform to retrieve the output spectrum. In fact, the simulations [Fig. 3.13(d)] reveal a very smooth transmission spectrum that confirms the effectively single-mode regime in this fiber. The latter claim is also supported by the near-field output profiles [in Fig. 3.11] that clearly show the core-guided fundamental mode.

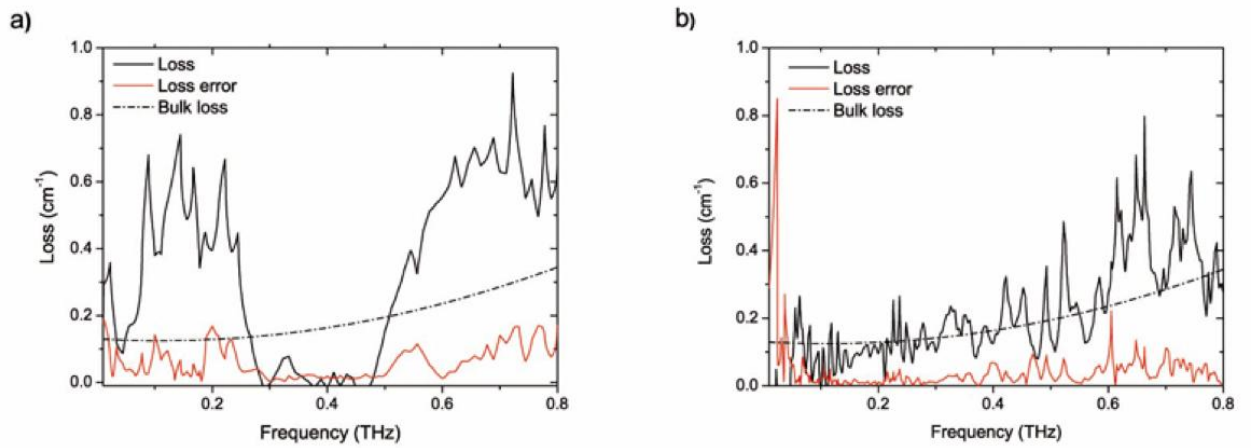

Figure 3.14 (a) Power propagation losses (measured by the cutback method) of the suspended solid core fiber, and of the (b) suspended porous core fiber, as a function of frequency. Dashed line corresponds to quadratic fit of the bulk material losses. Reprinted from [139] with permission from The Optical Society of America.

In Figs. 3.14(a)-(b) we present the power propagation losses of the fibers obtained from *cutback* measurements (black solid line) and also show as reference the quadratically increasing bulk material absorption losses (in dashed line) obtained from measurements in Fig. 3.8(b).

We here make a short parenthesis regarding the *cutback method* for evaluating the propagation losses of a given fiber. This destructive technique is performed by first measuring the transmitted power (P_1) through a fiber of initial length (L_1) and then cleaving the same fiber so as to "cut back" its length (L_2) and re-measuring the transmitted power (P_2). The propagation losses in *decibels* per fiber length scale (dB/L), where $L = L_1 - L_2$, are then given by:

$$\frac{\alpha(\mathrm{dB})}{L} = \frac{10}{L}\log_{10}\left(\frac{P_2}{P_1}\right) \tag{3.7}$$

Using the relation $\alpha(\mathrm{dB}/\ell) \cong (4.34)\cdot\alpha(\ell^{-1})$ where ℓ denotes the unit of length, it is then simple to convert from dB units to inverse lengths [Example: $\alpha(\mathrm{dB/cm}) \cong 4.34\cdot\alpha(\mathrm{cm}^{-1})$].

Upon examining the cutback propagation losses of the small solid core fiber [Fig. 3.14(a)], we find a low-loss region inside the 0.28–0.48 THz range. The loss values measured in this region are smaller in magnitude than the estimation of the absolute error [red solid line in Fig. 3.14(a)]. Therefore, we can only establish an upper bound value of ~ 0.02 cm^{-1} for the minimum propagation loss which is defined by the average loss error inside the low-loss region. This upper bound value of 0.02 cm^{-1} is considerably lower than the bulk material losses in this region. In

order to yield lower absolute error values in the low-loss region, it would require a setup capable of handling longer lengths of fiber so as to accumulate greater signal attenuation (or in other words "signal discrimination": $\Delta P = P_2 - P_1$) before detection at the fiber output. The low-loss regime is achieved owing to the large fraction of power guided in the low-loss air cladding, as clearly revealed in the near-field profiles of Fig. 3.10. At lower frequencies, the highly delocalized field enhances scattering on structural imperfections such as geometrical variations in the bridges' thicknesses. The strongly delocalized mode also enhances the field interaction with the polymer tubular cladding thus inducing high losses below 0.28 THz. For frequencies higher than 0.48 THz, the fiber propagation loss increases dramatically over the bulk material loss level. One rationale for this sharp increase in losses is the onset excitation of – or the conversion from the fundamental mode power into – a *higher-order* core-guided mode as pictured in [Fig. 3.15].

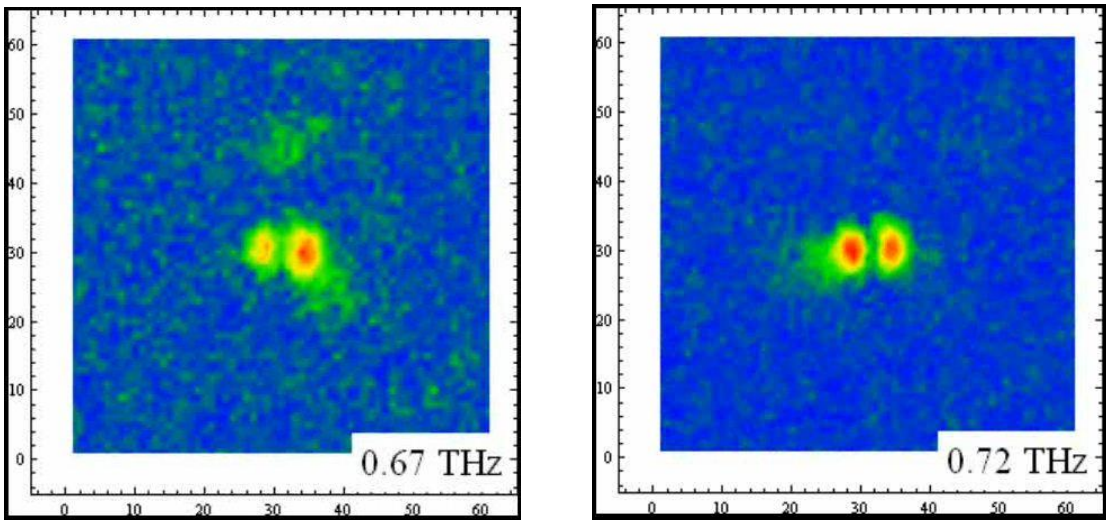

Figure 3.15 Near-field microscopy images of the output $|E_x|$-field profile at (a) 0.67 THz and (b) 0.72 THz, that indicate the presence of a higher-order guided mode in the suspended small solid core fiber.

At higher frequencies $\nu > 0.60$ THz, the near-field imaging clearly reveals a two-peaked output field profile that indicates the presence of a higher-order mode [Fig. 3.15]. Hence the fixed location of the near-field probe at the center of the suspended core (x_0, y_0), which coincides with the minimum trough of the two-peaked mode profile [Fig. 3.15], further helps to explain the radical drop in detected signal at these higher frequencies, and the subsequent surge in the measured losses [Fig. 3.14(a)]. Still, additional measurements must be performed to univocally confirm the origin of this threshold-like behavior near 0.60 THz.

In Fig. 3.14(b), corresponding to the suspended large porous core fiber, the general trend of the propagation losses is to follow that of the bulk material loss curve (in dashed line). Propagation losses increase from 0.05 cm^{-1} to 0.15 cm^{-1} between 0.10 THz and 0.40 THz; while the bulk material losses quadratically rise from 0.12 cm^{-1} to 0.16 cm^{-1} inside the same frequency range. The microstructured holey cladding surrounding the suspended core allows a substantial fraction of power to be guided in air, especially at low frequencies, so that propagation losses are substantially lower than the bulk level between 0.05 THz and 0.20 THz; a span which roughly matches the transmission bandwidth identified in the fiber transmission spectrum [Fig. 3.13(b)]. We note however that for higher frequencies $\nu > 0.20$ THz, the small 4% porosity of the core is not high enough in order to significantly lower the propagation losses below the level of bulk material absorption.

3.2.7 Conclusions

In summary, we emphasize that the key feature of the proposed *suspended core fibers* stems from their outer protective tubing that shields the core-guided mode from interactions with the surrounding environment. This feature enables direct and convenient manipulation of the fibers during normal operation, thus allowing practical positioning and holding of the fibers. Moreover, the protective tubing prevents the accumulation of dust and other contaminants on the surface of the fiber core that otherwise would perturb and attenuate the propagation of the guided mode. Finally we note that, shortly after publishing the results of this work, an Australian research group demonstrated a similar suspended solid core fiber fabricated with a Zeonex® polymer [219]. However the measured propagation losses are considerably higher ($\alpha \sim 0.24\ cm^{-1}$) compared to the low-loss level ($\alpha \sim 0.02\ cm^{-1}$) reported here [in Fig. 3.14(a)]. The reason for the poorer transmission demonstrated in [219] is owed to their larger core d_{core} = 400 μm and their smaller outer fiber diameter (OD = 3.0 mm) which limits the fraction of power guided inside low-loss air regions.

CHAPTER 4 : GENERAL DISCUSSION, CONCLUSIONS AND PERSPECTIVES

4.1 Nonlinear emerging microstructured fibers for the middle-infrared

In the case of the proposed *chalcogenide microporous fibers* in Chapter 2.1, the split-step Fourier method simulations at the 10.6 μm input wavelength demonstrated a broadest and un-segmented SC with a bandwidth of approximately 3100 nm (between 8.5 and 11.6 μm) and was obtained with the 0.9 nJ pulse of 1 ps duration. We first note that this simulated bandwidth was attained without full optimization of the parameters. Therefore for SC bandwidth optimization, a more detailed investigation is required to find the optimum parameters of the system (seed energy, pulse duration, GVD through fiber geometry, and especially, the fiber length) for maximal spectral broadening.

We also note that the effects of two-photon absorption (TPA) have been duly neglected in that numerical investigation because they were deemed negligible. The reason stems from the fact that As_2Se_3 glass behaves as a wide bandgap semiconductor with an energy gap of $E_g = 1.78$ eV, corresponding to a free space wavelength of 700 nm, meaning that very few carriers are actually excited at a wavelength of 10.6 μm corresponding to photons of $E = 0.12$ eV. And at such low optical energies (much lower than the half-gap level) the absorption losses in chalcogenide glasses are dominated by *impurities* and the onset of *multiphonon absorption* [82]. Nonetheless, a complete and accurate optimization of the SC bandwidth would also require incorporation of the *multiphoton absorption* effects, particularly TPA, since part of the simulated spectrum covers regions where these nonlinear absorption effects are somewhat significant.

Furthermore, the issues of photorefractive effects at the input facet of the fiber, and of permanent optical damage due to high peak laser intensities, were not considered in this study. Considering the small effective mode area (A_{eff} =11 μm^2) assumed in the simulations, the above input pulse parameters translate into a peak power of $P_0 = 0.846$ kW and a sizable peak modal intensity of 15.4 GW/cm^2 on the beam axis (assuming a Gaussian beam profile). Previously, supercontinuum generation in a high-purity As_2Se_3 glass small-core step-index fiber and a PCF fiber have sustained intensities on the order of ~ 3.5 GW/cm^2 at 1 kHz rate with no permanent damage reported [220]. However, it is still unclear whether the proposed As_2Se_3 microporous

fibers can sustain peak intensities >10 GW/cm^2 due to the lack of available data in that regime. Nevertheless, we note that contrary to standard small solid-core fibers where peak intensity is located in the solid glass center; the peak power in microporous fibers is mostly concentrated inside the air holes [as shown in Fig. 2.3(b)], thus significantly reducing the risk of optical damage to the glass structure.

The concern of photorefractive damage at the input side of the fiber can be minimized by putting an anti-reflecting coating on the surface of the fiber facet. The issue of photorefractive effects (and of low insertion efficiency into the small core fiber) can also be handled by exciting the fundamental mode of a *large mode area* porous chalcogenide fiber with large initial effective mode area (A_{eff} > 100 μm^2) and then gradually tapering the fiber (e.g. via flame-brush technique) so as to adiabatically "squeeze" the effective mode area to that of the desired size (11 μm^2) [221, 222]. Such fiber tapering decreases the risks of permanent optical damage at the input facet of a small-core fiber because of the substantially reduced intensities involved, and allows a much more efficient and convenient way of coupling laser excitation on the input side of the fiber, as well as collecting the generated SC at the output end, as schematically shown in Fig. 4.1 below.

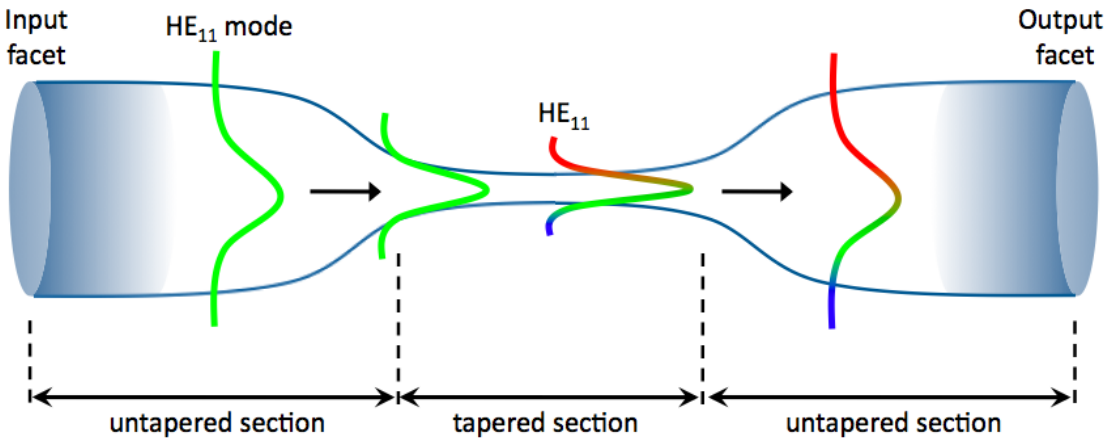

Figure 4.1 Schematic of the tapering of a multimoded nonlinear optical fiber into a single-mode fiber (along with enhanced optical nonlinearities inside the tapered section).

While the idea of filling the subwavelength holes with a nonlinear gas (Argon was suggested in [99]) to perform nonlinear optical interactions was proposed in the paper, this idea further requires detailed investigation in order to better assess its potential. In this regard, we note that considerable progress towards nonlinear optics with gas-filled hollow-core fibers has been achieved recently [223, 224].

Moreover, while the numerical study concentrated on small diameter fibers with $N = 4$ layers of subwavelength holes, we stress that the proposed type of EMF is also suited for the design of large mode area (LMA) fibers, where typically $N >> 4$, that are desirable for mitigating the optical nonlinearities and absorption losses, in (high-power) linear optical applications. In fact, the porous core design helps to lower the average refractive index of the core (n_{core}) – in order to reduce the refractive index contrast with the cladding (n_{clad}) – such that single-mode guidance can still be achieved with a large diameter (d_{core}) fiber. To this end, we recall the single-mode condition for the normalized frequency (V) in TIR-guided step-index fibers:

$$V = \frac{\pi}{\lambda} d_{\text{core}} \sqrt{n_{\text{core}}^2 - n_{\text{clad}}^2} < 2.405 \qquad (4.1)$$

Still, the study presented in Chapter 2.1 clearly demonstrated the potential of dispersion-tailored microporous fibers for nonlinear optical applications. Shortly after publication in [99], a research group headed by R. Buczynski experimentally demonstrated red-shifting of the ZDW of a nonlinear borosilicate-glass nanoporous fiber and subsequent near-infrared spectral broadening of nanojoule femtosecond 806 nm pulses [225, 226].

While the proposed microporous fiber design has been successfully implemented using current MOF fabrication technology; the realization of a *hybrid chalcogenide-metal nanostructured fiber* [proposed in Chapter 2.2] presents several practical challenges that need to be overcome before experimental demonstration is possible:

- The influence of thermo-optical effects was not investigated in [100]. Hence it is not clear whether the reported large Ohmic losses [in Fig. 2.16(b)] – especially for deep-subwavelength nanowire dimensions (i.e. for $r_{\text{fiber}} < 1\ \mu\text{m}$) – will translate into significant light-induced heating of the metallic nanowires, that could utimately disrupt the structural integrity of the NOF. In fact, it was recently demonstrated in [227] that when the points of junction between crossing metallic nanowires are subject to laser illumination, the intense and strongly-localized plasmonic "hotspots" [228, 229] that are excited may act to weld the adjoining metallic nanowires together, as illustrated in Fig. 4.2 below. Therefore a detailed study of the thermo-optical effects on the performance limits and on the overall mechanical integrity and reproducibility of the proposed hybrid chalco-metal NOF, is required in the future.

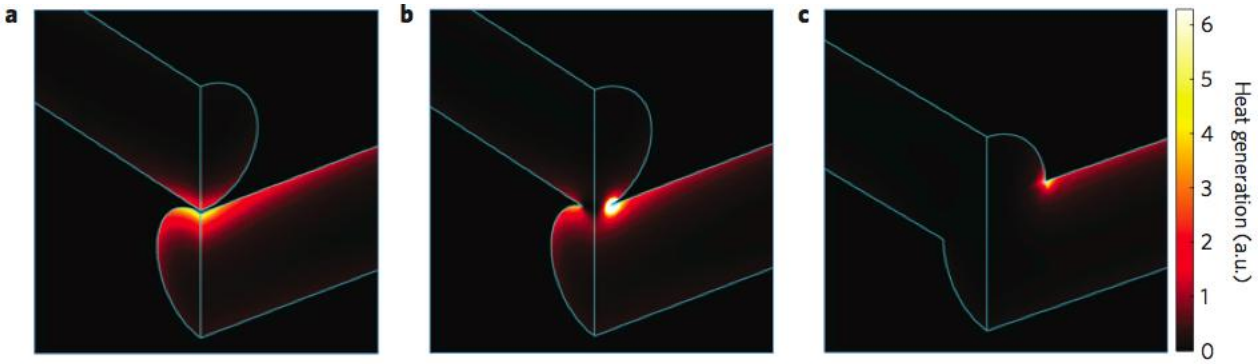

Figure 4.2 Finite element method simulations of optical heat generation at a silver nanowire junction during the nanowelding process in the 2 nm gap between silver nanowires with a 100 nm diameter and circular cross-section. The illumination source is a plane wave with a wavelength of 800 nm, incident from the top and polarized perpendicular to the top nanowire. Reprinted by permission from Macmillan Publishers Ltd: Nature Materials (Ref.[227]), copyright (2012).

- The optical properties of the modeled metallic nanowires used *bulk* metal properties even though at the nanoscale, new physics (new interface phenomena, nonlinear electrodynamics, and possible quantum effects) emerge that could significantly alter the metal's response. In the particular case of small-diameter hybrid NOFs ($r_{\text{fiber}} < 1\ \mu\text{m}$), the characteristic size of the metallic nanowires is deeply-subwavelength and becomes close to the *electron mean free path* in gold ($\ell_e^{\text{Au}} \sim 39\ \text{nm}$ at room temperatures) such that an abrupt nonlinear increase in electrical resistivity may occur in this nanoscale regime [230]. A potential solution to the latter problem was reported by a Belgian research group which suggested that a specific Gold/Copper bimetallic compound does not exhibit the usual nonlinear increase of the resistivity with size reduction of the metal nanostructures [231]. Alternatively, the detrimental nonlinear absorption with nanoscale size reduction could be countered via another nonlinear electrodynamical effect, namely, the *anomalous skin effect* (ASE) whereby the *skin depth* ($\delta_{\text{skin}} = \sqrt{2/\mu\sigma\omega}$ where μ and σ denote respectively the permeability and electrical conductivity of the metal [232]), in other words the magnetic field penetration distance inside the metal, which is classically assumed much larger than the *electron mean free path* ($\delta_{\text{skin}} >> \ell_e$) for bulk metals; becomes smaller in the ASE regime ($\delta_{\text{skin}} < \ell_e$). In this regime the electron surface scattering (i.e. electrons collisions with the interface) predominates over the conventional electron bulk scattering on lattice ions (i.e. the Drude model). The phenomenological explanation is that photoexcited electrons randomly oscillating within the skin depth (δ_{skin}) have a weak probability of colliding with the lattice of

ions located further away (ℓ_e on average) in the bulk [233]. The ASE conditions are typically obtained when a metal is exposed to low temperatures such that its conductivity increases markedly, and ℓ_e decreases correspondingly. The possibility of exploiting the ASE in (low-temperature) metals and superconductors towards low-loss plasmonic guidance has been discussed in theory [234], and very recently in practice [235-237] showing promising results. Additionally, a side benefit of actively cooling the hybrid NOF would be to prevent heat-induced damages to the nanofiber.

- At normal room temperatures (for which $\delta_{skin}^{Au} \approx 84\,\text{nm} > \ell_e^{Au}$) the magnitude of propagation losses in chalco-metallic NOFs are huge [Fig. 2.16(b)], and consequently hamper their practicability. One solution actively investigated at the moment is to use gain media adjacent to the metallic nanostructures in order to compensate for the plasmonic losses [238-245]. The challenge is then to find a gain medium that is compatible with mid-infrared frequencies and fiber drawing technology. A related topic of future research pertains to the use of novel metallic and semiconductor materials that exhibit high-carrier-mobility at room temperatures, such as *carbon nanotubes* and *graphene*, towards fiber-based low-loss plasmonics and for nanoscale optics in general [246-254]. In this regard, the synthesis technology is not yet mature such that it is still difficult to grow and isolate single-walled (and multi-walled) carbon nanotubes of a specific *chirality* (i.e. the orientation of the honeycomb lattice of C atoms with respect to tube axis) as well as graphene flakes of a particular size distribution; even though intense research is currently conducted in this direction [255-260].

4.2 Emerging microstructured fibers for terahertz waveguiding

The numerical study in Chapter 3.1 supported by experiments, demonstrated that polymer composites doped with high-refractive-index (hRI) microparticles enable to design dielectric reflectors for creating wide bandgaps in hollow-core Bragg fibers. However the analysis also revealed that the large absorption losses (at high concentration of dopants) can effectively destroy the bandgap confinement mechanism of the periodic reflectors made from such compounds, even when material combination with a very hRI contrast is used.

One solution is to lower the concentration of dopants at the expense of smaller bandgaps, whose width ($\Delta\omega$) centered at the frequency (ω_c) is predicted by the relation [28]:

$$\frac{\Delta\omega}{\omega_c} = \frac{4}{\pi}\sin^{-1}\left(\frac{n_H^2/\tilde{n}_H - n_L^2/\tilde{n}_L}{n_H^2/\tilde{n}_H + n_L^2/\tilde{n}_L}\right) \tag{4.2}$$

where n_H and n_L denote respectively the refractive indices of the high-index and low-index layers, with $\tilde{n}_i = \sqrt{n_i^2 - n_c^2 \sin^2\theta}$, and n_c is the refractive index of the hollow core. The above equation indicates that bandgap size is proportional to the refractive index contrast: $\Delta\omega/\omega_c \sim (n_H - n_L)/(n_H + n_L)$. Thus lowering the concentration of dopants results in a significant *reduction* of the modal losses incurred by material absorption in the dielectric layers, as demonstrated in Fig. 3.5 near 1.05 THz. In fact, the large material losses in the TiO_2-doped polymer-composite layers are primarily ascribed to the large scattering losses due to the high granularity and density inhomogeneity (even some cracks) of the polymer composites at high doping concentrations (>40 wt.%). Hence, fabrication techniques of the TiO_2-doped polymer composites must be improved. Among others, the average particle size of the TiO_2 dopants should be as small as possible in order to improve their homogeneous dispersion within the compound. The Dupont Ti-Pure® R-104 grade of TiO_2 (rutile crystalline) particles used in our study has an average particle size of 220 nm; but we note that novel commercial grades of anatase crystalline TiO_2 particles can reach an ultrafine average size of 70 nm [261].

Moreover, one of the causes of density homogeneity in the doped-polymer films is the presence of small local defects due to micro-bubbles. These air bubbles are most likely created when the titania particles are mixed with the host polymer melt during the film extrusion process. To minimize the formation of micro-bubbles, a proper *degassing* procedure (possibly with microscope monitoring) should be implemented, as suggested in [209]. Alternatively, it has been suggested in [123] to exploit these micro-bubbles so as to create low-refractive-index polymer layers, with the refractive index change controlled by the (gaseous) porosity introduced inside the host polymer via foaming agents. These low-index layers would then be co-rolled with their higher-index non-porous counterparts (both sharing similar thermo-forming properties) for making the Bragg fibers. All the above practical reasons suggest that doped-polymer THz Bragg fiber technology – which is still in its infancy – will first be amenable at low doping concentrations of high-index microparticles. Hence, future efficient designs of doped Bragg fibers should initially focus on utilizing low-refractive-index composites for creating the multi-layered dielectric reflector.

The theoretical and experimental investigation of novel *suspended core dielectric fibers* [in Chapter 3.2] represents a significant step towards practical terahertz waveguiding. But there are still a number of pending issues that must be adressed:

- In the experiments reported in Chapter 3.2 and [139], solely the E_x-field component of the near-field have been imaged. Rotating the polarization-sensitive detector by a 90° angle and performing another full sets of measurements would provide a similar mapping of the output E_y-field component. The latter procedure, which was not performed in the experiments due to lack of time, would permit a more accurate identification and discrimination of the various modes (especially higher-order modes; example in Fig. 3.15) supported by the suspended fibers.

- The fabrication of the *suspended porous core fibers* must be improved in order to significantly increase the core porosity, which was only 4% in the current design. This limitation hinders the practical adoption of *suspended porous core fibers* that represent attractive candidates for the fully-encapsulated single-moded large-mode-area low-loss THz signal delivery; a key achievement in THz waveguiding. The first step towards this goal would be to increase the number of rings of holes (in hexagonal lattice) inside the core, which was set to N=3 in [139] for easier fabrication. Furthermore, the cross-section of the suspended porous core fiber [Fig. 3.7(d)] showed irregular holes with many that became partially or completely blocked during the fabrication process by the stack-and-draw method; due to uneven (or insufficient) pressurization of the tiny holes. The alternate *casting method* for fabricating porous fibers [discussed in Chapter 1.2] would permit drawing of a fully solid-core preform into a suspended core fiber, and afterwards, reveal the holes by etching away the sacrifical polymer that fills the holes. The latter technique would yield better overall geometrical regularity of the holes (spatial distribution and shape) and result in fewer blocked holes, owing to the separate etching step.

- The error levels in the fiber loss measurements [Fig. 3.14] prevented us from accurately quantifying the minimum propagation losses of the *suspended solid core fiber*; which instead was estimated by the average loss error inside the lowest-loss frequency window. We first explained that these loss levels were so low (~ 0.02 cm^{-1}) that the short fiber lengths (~ 11 cm) used for the cutback measurements only allow about 20% maximal loss from the input power. Therefore it was suggested that longer lengths of test fiber would enable greater loss discrimination between the various fiber lengths, and hence better accuracy. The other important source of errors in the

loss measurements stems from the poor quality and the high variability in the successive fiber cleaves (performed with a razor blade) in the cutback method. Slight changes in the angles of successive fiber cleaves will result in different Fresnel reflection coefficients at the corresponding facet, resulting in non-repeatable errors. Moreover, each new cleave of a highly-porous polymer fiber may induce unpredictable structural deformations to the fiber. To improve cleave reproducibility of polymer fibers, a cleaving setup based on UV excimer laser [262] and a fully-automated razor-blade guillotine setup [263] (with automatic control of fiber temperature, blade temperature and cleaving speed) have both demonstrated nice results.

- Additionally, one procedure to minimize the loss errors in future experiments would be to more accurately measure the *total* output power from the fibers by introducing a THz focusing lens in the setup, whose role is to more effectively collect the output THz waves from the fibers and focus the radiation on the detector. Such implementation will also alleviate the high sensitivity of measurements to the exact fixed location of the probe, thus taking into account the contributions of the low-order and higher-order modes (with non-homogeneous field profiles) on an equal footing.

- It was brought to my attention by a participant in the attendance of a conference presentation [264] that the optical mode isolation (in other words: "fiber encapsulation") could be further improved by covering the suspended core fibers with an outer metal sheet layer of sufficient thickness. Such metal coating would prevent any residual THz radiation leaking from the polymer tubular cladding [see for example Fig. 3.10 at 0.16 THz and 0.30 THz] to interact with the surrounding environment, for the whole THz range.

- We note that, to the best of our knowledge, there are currently no bending loss measurements on standard *subwavelength fibers*. The chief reason lies in that it is very challenging to realize in practice owing to the need for fiber holders that would likely perturb the propagating mode profile. However, with the proposed *suspended core fibers* this becomes a definite possibility. Further experiments are required in order to quantify the resilience of the proposed suspended core fibers to bending, and to measure the associated losses.

- An interesting future application of suspended core polymer fibers pertains to exploiting the highly-delocalized (i.e. evanescent) terahertz radiation guided by the suspended core, for the non-ionizing and athermal biochemical sensing and monitoring of analytes. Prior research on utilizing

suspended core fibers for biochemical and biomedical sensing have been conducted in the visible and near-infrared parts of the spectrum [265, 266]; but never at THz frequencies. Very recently, our research group demonstrated the successful demonstration of a suspended solid core fiber for the THz evanescent field biosensing of *E. Coli* bacteria which had binded on the outer surface of the suspended core [267, 268].

REFERENCES

[1] T. Monro, H. Ebendorff-Heidepriem, W.Q. Zhang, and S. Afshar, "Emerging Nonlinear Optical Fibers: Revised Fundamentals, Fabrication and Access to Extreme Nonlinearity," *IEEE Journal of Quantum Electronics*, vol. 45, no. 11, pp. 1357–1364, 2009.

[2] T. Monro, S. Afshar, H. Ebendorff-Heidepriem, W.Q. Zhang, and Y. Ruan, "Emerging Optical Fibers: New Fiber Materials and Structures," in *Conference on Lasers and Electro-Optics (CLEO)*, 2009, paper CFH2.

[3] O.V. Butov, K.M. Golanta, A.L. Tomashuka, M.J.N. van Stralenb, and A.H.E. Breuls, "Refractive index dispersion of doped silica for fiber optics," *Optics Communications*, vol. 213, pp. 301–308, 2002.

[4] G.P. Agrawal, *Nonlinear Fiber Optics (4th Ed.)*, San Diego, USA: Academic Press, 2006.

[5] R. Won, "Shining in the mid-infrared," *Nature Photonics*, vol. 5, pp. 457–458, 2011.

[6] B. Jalali, "Nonlinear optics in the mid-infrared," *Nature Photonics*, vol. 4, pp. 506–508, 2010.

[7] I.T. Sorokina, and K.L. Vodopyanov (Eds.), *Solid-State Mid-Infrared Laser Sources*, Berlin, Germany: Springer, 2008.

[8] J. Dudley, and R. Taylor (Eds.), *Supercontinuum Generation in Optical Fibers*, New York, USA: Cambridge University Press, 2010.

[9] J. Dudley, G. Genty, and S. Coen, "Supercontinuum generation in photonic crystal fiber," *Reviews of Modern Physics*, vol. 78, no. 4, pp. 1135–1184, 2006.

[10] G. Genty, S. Coen, and J. Dudley, "Fiber supercontinuum sources," *Journal of the Optical Society of America B*, vol. 24, no. 8, pp. 1771–1785, 2007.

[11] R.R. Alfano (Ed.), *The Supercontinuum Laser Source*, New York, USA: Springer, 2006.

[12] J. Dudley, and R. Taylor, "Ten years of nonlinear optics in photonics crystal fibre," *Nature Photonics*, vol. 3, pp. 85–-90, 2009.

[13] G.P. Agrawal, "Nonlinear fiber optics: its history and recent progress," *Journal of the Optical Society of America B*, vol. 28, no. 12, pp. A1-A10, 2011.

[14] J.S. Sanghera, and I.D. Aggarwal, *Infrared fibers optics*, Boca Raton, USA: CRC Press, 1998.

[15] J.H.V. Price, T.M. Monro, H. Ebendorff-Heidepriem, F. Poletti, V. Finazzi, J.Y.Y. Leong, P. Petropoulos, J.C. Flanagan, G. Brambilla, X. Feng and D.J. Richardson, "Non-silica microstructured optical fibers for mid-IR supercontinuum generation from 2μm – 5μm," *Proceedings of SPIE*, vol. 6102, no. 61020A, 2006.

[16] J.H.V. Price, T.M. Monro, H. Ebendorff-Heidepriem, F. Poletti, P. Horak, V. Finazzi, J.Y.Y. Leong, P. Petropoulos, J.C. Flanagan, G. Brambilla, X. Feng and D.J. Richardson, "Mid-IR Supercontinuum Generation From Nonsilica Microstructured Optical Fibers," *IEEE Journal of Selected Topics in Quantum Electronics*, vol. 13, no. 3, pp. 738–749, 2007.

[17] J.A. Harrington, "Infrared fiber optics," in *OSA Handbook of optics: Vol. III*, M. Bass (Ed.), New York, USA: McGraw-Hill, 2007.

[18] J.A. Harrington, *Infrared fibers and their applications*, New York, USA: SPIE Press, 2004.

[19] J.A. Harrington, "A Review of IR Transmitting, Hollow Waveguides," *Fiber and Integrated Optics*, vol. 19, pp. 211–227, 2000.

[20] L. Butvina, O.V. Sereda, E.M. Dianov, N.V. Lichkova, and V.N. Zagorodnev, "Single-mode microstructured optical fiber for the middle infrared," *Optics Letters*, vol. 32, pp. 334–336, 2007.

[21] L. Butvina, A.L. Butvina, A. Okhrimchuk, N. Lichkova, V. Zagorodnev, and E. Dianov, "Low loss micro and nano structured single mode crystalline fibers for 5-15 μm," in *Advances in Optical Materials (AIOM) Conference*, 2011, paper AIThD.

[22] L. Butvina, O.V. Sereda, E.M. Dianov, N.V. Lichkova and V.N. Zagorodnev, "Single mode leakage channel fiber for the middle infrared," *Proceedings of SPIE*, vol. 7357, no. 73570G, 2009.

[23] S. Shalem, A. Tsun, E. Rave, A. Millo, L. Nagli, and A. Katzir, "Silver halide single-mode fibers for the middle infrared," *Applied Physics Letters*, vol. 87, 091103, 2005.

[24] T. Lewi, A. Tsun, A. Katzir, J. Kaster, and F. Fuchs, “Silver halide single mode fibers for broadband middle infrared stellar interferometry,” *Applied Physics Letters*, vol. 94, 261105, 2009.

[25] B. Temelkuran, S.D. Hart, G. Benoit, J.D. Joannopoulos and Y. Fink, “Wavelength-scalable hollow optical fibres with large photonic bandgaps for CO2 laser transmission,” *Nature*, vol. 420, pp. 650–653, 2002.

[26] R. George and J.A. Harrington, “Infrared transmissive, hollow plastic waveguides with inner Ag–AgI coatings,” *Applied Optics*, vol. 44, pp. 6449–6455, 2005.

[27] A. Hongo, K. Morosawa, K. Matsumoto, T. Shiota and T. Hashimoto, “Transmission of kilowatt-class CO2 laser light through dielectric-coated metallic hollow waveguides for material processing,” *Applied Optics*, vol. 31, pp. 5114–5120, 1992.

[28] S.G. Johnson, M. Ibanescu, M. Skorobogatiy, O. Weisberg, T.D. Engeness, M. Soljacic, S.A. Jacobs, J.D. Joannopoulos, and Y. Fink, “Low-loss asymptotically single-mode propagation in large-core OmniGuide fibers,” *Optics Express*, vol. 9, pp. 748–779, 2001.

[29] T.D. Engeness, M. Ibanescu, S.G. Johnson, O. Weisberg, M. Skorobogatiy, S.A. Jacobs, and Y. Fink, “Dispersion tailoring and compensation by modal interactions in OmniGuide fibers,” *Optics Express*, vol. 11, pp. 1175–1196, 2003.

[30] M. Ibanescu, Y. Fink, S. Fan, E.L. Thomas, and J.D. Joannopoulos, “An All-Dielectric Coaxial Waveguide,” *Science*, vol. 289, pp. 415–419, 2000.

[31] Y. Fink, J.N. Winn, S. Fan, C. Chen, J. Michel, J.D. Joannopoulos, and E.L. Thomas, “A Dielectric Omnidirectional Reflector,” *Science*, vol. 282, pp. 1679–1682, 1998.

[32] Michel Poulain, Marcel Poulain, and J. Lucas, “Verres fluorés au tétrafluorure de zirconium propriétés optiques d'un verre dopé au Nd^{3+},” *Materials Research Bulletin*, vol. 10, no. 4, pp. 243–246, 1975.

[33] H. Ebendorff-Heidepriem, T. Foo, R.C. Moore, W. Zhang, Y. Li, T.M. Monro, A. Hemming, and D.G. Lancaster, “Fluoride glass microstructured optical fiber with large mode area and mid-infrared transmission,” *Optics Letters*, vol. 33, pp. 2861-2863, 2008.

[34] X. Zhu, and N. Peyghambarian, “High-Power ZBLAN Glass Fiber Lasers: Review and Prospect,” *Advances in OptoElectronics*, vol. 2010, 501956, 2010.

[35] F. Désévédavy, “Fibres optiques micro-structurées à base de verres de chalcogénures pour applications dans le domaine des télécommunications et le moyen IR,” *Doctoral thesis*, Université de Rennes, France, 2008.

[36] M. Rozé, “Verres et vitrocéramiques transparents dans l'infrarouge pour application à l'imagerie thermique,” *Doctoral thesis*, Université de Rennes, France, 2009.

[37] A. Zakery and S.R. Elliot, “Optical properties and applications of chalcogenide glasses: a review,” *Journal of Non-Crystalline Solids*, vol. 330, pp. 1-12, 2003.

[38] J.S. Sanghera and I.D. Aggarwal, “Active and passive chalcogenide glass optical fibers for IR applications: a review,” *Journal of Non-Crystalline Solids*, vol. 256-257, pp. 6-16, 1999.

[39] F. Désévédavy, G. Renversez, J. Troles, L. Brilland, P. Houizot, Q. Coulombier, F. Smektala, N. Traynor, and J.-L. Adam, “Te-As-Se glass microstructured optical fiber for the middle infrared,” *Applied Optics*, vol. 48, no. 19, pp. 3860-3865, 2009.

[40] P. Bordé, G. Perrin, T. Nguyen, A. Amy-Klein, C. Daussy, P.-I. Raynal, A. Leger and G. Maze, “10-μm wavefront spatial filtering: first results with chalcogenide fibers,” *Proceedings of SPIE*, vol. 4838, pp. 273–279, 2003.

[41] P. Houizot, C. Boussard-Plédel, A. J. Faber, L. K. Cheng, B. Bureau, P. A. Van Nijnatten, W.L.M. Gielesen, J. Pereira do Carmo, and J. Lucas, “Infrared single mode chalcogenide glass fiber for space,” *Optics Express*, vol. 15, pp. 12529–12538, 2007.

[42] Amorphous Materials Inc. “Amorphous Materials IR Fibers,” Internet : http://www.amorphousmaterials.com/IR%20Fibers.htm, [24 Jan. 2012].

[43] CorActive High-Tech Inc. “Infrared Fiber Products,” Internet : http://www.coractive.com/pdf/brochures/InfraredProducts_BR0001r04.pdf, [24 Jan. 2012].

[44] L. Brilland, F. Smektala, G. Renversez, T. Chartier, J. Troles, T.N. Nguyen, N. Traynor, and A. Monteville, “Fabrication of complex structures of Holey Fibers in Chalcogenide glass,” *Optics Express*, vol. 14, no. 3, pp. 1280–1285, 2006.

[45] F. Smektala, F. Désévédavy, L. Brilland, P. Houizot, J. Troles, and N. Traynor, “Advances in the elaboration of chalcogenide photonic crystal fibers for the mid infrared,” *Proceedings of SPIE*, vol. 6588, no. 658803, 2007.

[46] F. Désévédavy, G. Renversez, L. Brilland, P. Houizot, J. Troles, Q. Coulombier, F. Smektala, N. Traynor, and J.-L. Adam, "Small-core chalcogenide microstructured fibers for the infrared," *Applied Optics*, vol. 47, no. 32, pp. 6014–6021, 2008.

[47] Q. Coulombier, L. Brilland, P. Houizot, T.N. Nguyen, T. Chartier, F. Smektala, G. Renversez, A. Monteville, D. Méchin, T. Pain, H. Orain, J.-C. Sangleboeuf, and J. Troles, "Casting method for producing low-loss chalcogenide microstructured optical fibers," *Optics Express*, vol. 18, no. 8, pp. 9107–9112, 2010.

[48] Z. Guiyao, H. Zhiyun, L. Shuguang, and H. Lantian, "Fabrication of glass photonic crystal fibers with a die-cast process," *Applied Optics*, vol. 45, no. 18, pp. 4433–4436, 2006.

[49] J. Troles, J.-L. Adam, L. Brilland, Q. Coulombier, and T. Chartier, "Elaboration of photonic crystal fibers for telecom and mid infrared wavelengths," in *International Conference on Transparent Optical Networks (ICTON)*, 2010, paper We.B4.4.

[50] T. Monro, and H. Ebendorff-Heidepriem, "Progress in Microstructured Optical Fibers," *Annual Review of Materials Research*, vol. 36, pp. 467–495, 2006.

[51] H. Ebendorff-Heidepriem, and T. Monro, "Extrusion of complex preforms for microstructured optical fibers," *Optics Express*, vol. 15, no. 23, pp. 15086–15092, 2007.

[52] H. Ebendorff-Heidepriem, R.C. Moore, and T. Monro, "Progress in the Fabrication of the Next- Generation Soft Glass Microstructured Optical Fibers," *Proceedings of the American Institute of Physics (AIP) Conference*, vol. 1055, pp. 95–98, 2008.

[53] D. Hewak, K. Kahn, and C.C. Huang, "Applications of Chalcogenide Fibers," in *Optical Society of America: Specialty Optical Fibers Conference (SOF)*, 2011, paper SOTuB.

[54] N. Anscombe, "Interview with Dan Hewak: The promise of chalcogenides," *Nature Photonics*, vol. 5, p. 474, 2011.

[55] Y.R. Shen and G.-Z. Yang. "Theory of Self-Phase Modulation and Spectral Broadening," in *The Supercontinuum Laser Source*, 2nd ed., R.R. Alfano (Ed.), New York: Springer, 2006, pp. 1-32.

[56] R.R. Alfano and S.L. Shapiro. "Observation of self-phase modulation and small scale filaments in crystals and glasses," *Physical Review Letters*, vol. 24, pp. 584–592, 1970.

[57] C. Lin and R.H. Stolen, "New nanosecond continuum for excited-state spectroscopy," *Applied Physics Letters*, vol. 28, pp. 216–218, 1976.

[58] P. Beaud, W. Hodel, B. Zysset, and H.P. Weber, "Ultrashort pulse propagation, pulse breakup, and fundamental soliton formation in a single-mode optical fiber," *IEEE Journal of Quantum Electronics*, vol. 23, pp. 1938–1946, 1987.

[59] A.S. Gouveia-Neto, M.E. Faldon, and J.R. Taylor, "Solitons in the region of the minimum group-velocity dispersion of single-mode optical fibers," *Optics Letters*, vol. 13, pp. 770–772, 1988.

[60] T. Morioka, K. Mori, and M. Saruwatari, "More than 100-wavelength-channel picosecond optical pulse generation from single laser source using supercontinuum in optical fibres," *Electronics Letters*, vol. 29, pp. 862–864, 1993.

[61] K. Mori, T. Morioka, and M. Saruwatari, "Ultrawide spectral range group-velocity dispersion measurement utilizing supercontinuum in an optical-fiber pumped by a 1.5 μm compact laser source," *IEEE Transactions on Instrumentation and Measurement*, vol. 44, pp. 712–715, 1995.

[62] K.R. Tamura, H. Kubota and M. Nakazawa, "Fundamentals of stable continuum generation at high repetition rates," *IEEE Journal of Quantum Electronics*, vol. 36, pp. 773–779, 2000.

[63] J.K. Ranka, R.S. Windeler, and A.J. Stentz, "Visible continuum generation in air–silica microstructure optical fibers with anomalous dispersion at 800 nm," *Optics Letters*, vol. 25, pp. 25–27, 2000.

[64] S. Afshar, and T. Monro, "A full vectorial model for pulse propagation in emerging waveguides with subwavelength structures part I: Kerr nonlinearity," *Optics Express*, vol. 17, pp. 2298–2318, 2009.

[65] S. Afshar, W.Q. Zhang, H. Ebendorff-Heidepriem, and T. Monro, "Small core optical waveguides are more nonlinear than expected: experimental confirmation," *Optics Letters*, vol. 34, pp. 3577–3579, 2009.

[66] N. Akhmediev, and M. Karlsson, "Cherenkov radiation emitted by solitons in optical fibers," *Physical Review A*, vol. 51, pp. 2602–2607, 1995.

[67] A.V. Husakou, and J. Herrmann, “Supercontinuum generation of higher-order solitons by fission in photonic crystal fibers”, *Physical Review Letters,* vol. 87, 203901, 2001.

[68] L. Yin, Q. Lin, and G.P. Agrawal, “Soliton fission and supercontinuum generation in silicon waveguides,” *Optics Letters,* vol. 32, pp. 391–393, 2007.

[69] C. Xia, M. Kumar, M.N. Islam, A. Galvanauskas, F.L. Terry Jr. and M.J. Freeman, “All-Fiber-Integrated Mid-Infrared Supercontinuum System with 0.7 Watts Time-Averaged Power,” in *Conference on Lasers and Electro-Optics (CLEO),* 2007, paper CThH1.

[70] C. Xia, Z. Xu, M.N. Islam, F.L. Terry Jr., M.J. Freeman, A. Zakel, and J. Mauricio, “10.5 W Time-Averaged Power Mid-IR Supercontinuum Generation Extending Beyond 4 μm With Direct Pulse Pattern Modulation,” *IEEE Journal of Selected Topics in Quantum Electronics,* vol. 15, pp. 422–434, 2009.

[71] B.J. Eggleton, “Chalcogenide photonics: fabrication, devices and applications: Introduction,” *Optics Express,* vol. 18, pp. 26632–26634, 2010.

[72] B.J. Eggleton, B. Luther-Davies, and K. Richardson “Chalcogenide photonics,” *Nature Photonics,* vol. 5, pp. 141–148, 2011.

[73] M.D. Pelusi, V.G. Ta’eed, L. Fu, E. Mägi, M.R.E. Lamont, S. Madden, D.-Y. Choi, D.A.P. Bulla, B. Luther-Davies, and B.J. Eggleton, “Applications of Highly-Nonlinear Chalcogenide Glass Devices Tailored for High-Speed All-Optical Signal Processing,” *IEEE Journal of Selected Topics in Quantum Electronics,* vol. 14, pp. 529–539, 2008.

[74] C. Tsay, F. Toor, C.F. Gmachl, and C.B. Arnold, “Chalcogenide glass waveguides integrated with quantum cascade lasers for on-chip mid-IR photonic circuits,” *Optics Letters,* vol. 35, pp. 3324–3326, 2010.

[75] J.S. Sanghera, L.B. Shaw, I.D. Aggarwal, “Chalcogenide Glass-Fiber-Based Mid-IR Sources and Applications,” *IEEE Journal of Selected Topics in Quantum Electronics*, vol. 15, pp. 114–119, 2009.

[76] Z.G. Lian, Q.Q. Li, D. Furniss, T.M. Benson, and A.B. Seddon, “Solid Microstructured Chalcogenide Glass Optical Fibers for the Near- and Mid-Infrared Spectral Regions,” *IEEE Photonics Technology Letters,* vol. 21, pp. 1804–1806, 2009.

[77] J. Troles, Q Coulombier, G. Canat, M. Duhant, W. Renard, P. Toupin, L. Calvez, G. Renversez, F. Smektala, M. El-Amraoui, J.-L. Adam, T. Chartier, D. Mechin, L. Brilland, "Low loss microstructured chalcogenide fibers for large non linear effects at 1995 nm," *Optics Express*, vol. 18, pp. 26647–26654, 2010.

[78] C. Conseil, Q. Coulombier, C. Boussard-Plédel, J. Troles, L. Brilland, G. Renversez, D. Mechin, B. Bureau, J.-L. Adam, and J. Lucas, "Chalcogenide step index and microstructured single mode fibers," *Journal of Non-Crystalline Solids*, vol. 357, pp. 2480–2483, 2011.

[79] G. Lenz, J. Zimmermann, T. Katsufuji, M.E. Lines, H.Y. Hwang, S. Spälter, R.E. Slusher, and S.-W. Cheong, J. S. Sanghera, and I. D. Aggarwal, "Large Kerr effect in bulk Se-based chalcogenide glasses," *Optics Letters*, vol. 25, pp. 254–256, 2000.

[80] J.M. Harbold, F.Ö. Ilday, F.W. Wise, J.S. Sanghera, V.Q. Nguyen, L.B. Shaw, and I.D. Aggarwal, "Highly nonlinear As–S–Se glasses for all-optical switching," *Optics Letters*, vol. 27, pp. 119–121, 2002.

[81] R. Stegeman, L. Jankovic, H. Kim, C. Rivero, G. Stegeman, K. Richardson, P. Delfyett, Y. Guo, A. Schulte, and T. Cardinal, "Tellurite glasses with peak absolute Raman gain coefficients up to 30 times that of fused silica," *Optics Letters*, vol. 28, pp. 1126–1128, 2003.

[82] R.E. Slusher, G. Lenz, J. Hodelin, J.S. Sanghera, L.B. Shaw, and I.D. Aggarwal, "Large Raman gain and nonlinear phase shifts in high-purity As2Se3 chalcogenide fibers," *Journal of the Optical Society of America B*, vol. 21, pp. 1146–1155, 2004.

[83] A. Zakery, and S.R. Elliott, *Optical Nonlinearities in Chalcogenide Glasses and their Applications*, Berlin, Germany: Springer, 2007.

[84] T.M. Monro, Y.D. West, D.W. Hewak, N.G.R. Brodcrick, and D.J. Richardson, "Chalcogenide holey fibres," *Electronics Letters*, vol. 36, pp. 1998–2000, 2000.

[85] M.A. Foster, and A.L. Gaeta, "Ultra-low threshold supercontinuum generation in sub-wavelength waveguides," *Optics Express*, vol. 12, pp. 3137–3143, 2004.

[86] X. Feng, F. Poletti, A. Camerlingo, F. Parmigiani, P. Horak, P. Petropoulos, W.H. Loh, and D.J. Richardson, "Dispersion-shifted all-solid high index-contrast microstructured optical fiber for nonlinear applications at 1.55 um," *Optics Express*, vol. 17, pp. 20249–20255, 2009.

[87] M. Liao, X. Yan, G. Qin, C. Chaudhari, T. Suzuki, and Y. Ohishi, "Controlling the chromatic dispersion of soft glass highly nonlinear fiber through complex microstructure," *Journal of Non-Crystalline Solids*, vol. 356, pp. 2613–2617, 2010.

[88] F. Poletti, X. Feng, G.M. Ponzo, M.N. Petrovich, W.H. Loh, and D.J. Richardson, "All-solid highly nonlinear singlemode fibers with a tailored dispersion profile," *Optics Express*, vol. 19, pp. 66–80, 2010.

[89] E.C. Mägi, L. Fu, H.C. Nguyen, M.R.E. Lamont, D.-I. Yeom, and B.J. Eggleton, "Enhanced Kerr nonlinearity in sub-wavelength diameter As_2Se_3 chalcogenide fiber tapers," *Optics Express*, vol. 15, pp. 10324–10329, 2007.

[90] D.-I. Yeom, E.C. Mägi, M.R.E. Lamont, M.A.F. Roelens, L. Fu, and B.J. Eggleton, "Low-threshold supercontinuum generation in highly nonlinear chalcogenide nanowires," *Optics Letters*, vol. 33, pp. 660–662, 2008.

[91] C. Baker, and M. Rochette, "Highly nonlinear hybrid AsSe-PMMA microtapers," *Optics Express*, vol. 18, pp. 12391–12398, 2010.

[92] D.D. Hudson, S.A. Dekker, E.C. Mägi, A.C. Judge, S.D. Jackson, E. Li, J.S. Sanghera, L.B. Shaw, I.D. Aggarwal, and B.J. Eggleton, "Octave spanning supercontinuum in an As_2S_3 taper using ultralow pump pulse energy," *Optics Letters*, vol. 36, pp. 1122–1124, 2011.

[93] M. El-Amraoui, J. Fatome, J.C. Jules, B. Kibler, G. Gadret, C. Fortier, F. Smektala, I. Skripatchev, C.F. Polacchini, Y. Messaddeq, J. Troles, L. Brilland, M. Szpulak, and G. Renversez, "Strong infrared spectral broadening in low-loss As-S chalcogenide suspended core microstructured optical fibers," *Optics Express*, vol. 18, pp. 4547–4556, 2010.

[94] M. El-Amraoui, G. Gadret, J.C. Jules, J. Fatome, C. Fortier, F. Désévédavy, I. Skripatchev, Y. Messaddeq, J. Troles, L. Brilland, W. Gao, T. Suzuki, Y. Ohishi, and F. Smektala, "Microstructured chalcogenide optical fibers from As_2S_3 glass: towards new IR broadband sources," *Optics Express*, vol. 18, pp. 26655–26665, 2010.

[95] M. Liao, X. Yan, W. Gao, Z. Duan, G. Qin, T. Suzuki, and Y. Ohishi, "Five-order SRSs and supercontinuum generation from a tapered tellurite microstructured fiber with longitudinally varying dispersion," *Optics Express*, vol. 19, pp. 15389–15396, 2011.

[96] P. Domachuk, N.A. Wolchover, M. Cronin-Golomb, A. Wang, A.K. George, C.M.B. Cordeiro, J.C. Knight, F.G. Omenetto, "Over 4000 nm Bandwidth of Mid-IR Supercontinuum Generation in sub-centimeter Segments of Highly Nonlinear Tellurite PCFs," *Optics Express*, vol. 16, pp. 7161–7168, 2008.

[97] J. Hu, C.R. Menyuk, L.B. Shaw, J.S. Sanghera, and I.D. Aggarwal, "Maximizing the bandwidth of supercontinuum generation in As2Se3 chalcogenide fibers," *Optics Express*, vol. 18, pp. 6722–6739, 2010.

[98] J. Hu, C.R. Menyuk, L.B. Shaw, J.S. Sanghera, and I.D. Aggarwal, "Computational study of 3–5 μm source created by using supercontinuum generation in As_2S_3 chalcogenide fibers with a pump at 2 μm," *Optics Letters*, vol. 35, pp. 2907–2909, 2010.

[99] B. Ung, and M. Skorobogatiy, "Chalcogenide microporous fibers for linear and nonlinear applications in the mid-infrared," *Optics Express*, vol. 18, pp. 8647–8659, 2010.

[100] B. Ung, and M. Skorobogatiy, "Extreme nonlinear optical enhancement in chalcogenide glass fibers with deep-subwavelength metallic nanowires," *Optics Letters*, vol. 36, pp. 2527–2529, 2011.

[101] B. Ferguson, and X.-C. Zhang, "Materials for terahertz science and technology," *Nature Materials*, vol. 1, pp. 26–33, 2002.

[102] G. Imeshev, M.E. Fermann, K.L. Vodopyanov, M.M. Fejer, X. Yu, J.S. Harris, D. Bliss, and C. Lynch, "High- power source of THz radiation based on orientation-patterned GaAs pumped by a fiber laser," *Optics Express*, vol. 14, pp. 4439–4444, 2006.

[103] W. Shi, L. Hou, Z. Lui, and T. Tongue, "Terahertz generation from SI-GaAs stripline antenna with different structural parameters", *Journal of the Optical Society of America B*, vol. 26, pp. A107−A112, 2009.

[104] M. Tang, H. Minamide, Y. Wang, T. Notake, S. Ohno, and H. Ito, "Dual-wavelength single-crystal double-pass KTP optical parametric oscillator and its application in terahertz wave generation," *Optics Letters*, vol. 35, pp. 1698–1700, 2010.

[105] M.C. Hoffmann, and J.A. Fülöp, "Intense ultrashort terahertz pulses: generation and applications," *Journal of Physics D: Applied Physics*, vol. 44, pp. 083001, 2011.

[106] Y. Cai, I. Brener, J. Lopata, J. Wynn, L. Pfeiffer, J.B. Stark, Q. Wu, X.-C. Zhang, and J.F. Federici, "Coherent terahertz radiation detection: Direct comparison between free-space electro-optic sampling and antenna detection," *Applied Physics Letters*, vol. 73, pp. 444–446, 1998.

[107] N. Karpowicz, J. Chen, T. Tongue, and X.-C. Zhang, "Coherent millimetre wave to mid-infrared measurements with continuous bandwidth reaching 40 THz," *Electronics Letters*, vol. 44, pp. 544–545, 2008.

[108] D. Dooley, "Sensitivity of broadband pyroelectric terahertz detectors continues to improve", *Laser Focus World*, vol. 46, pp. 49–56, 2010.

[109] Z. Popovic, and E.N. Grossman, "THz Metrology and Instrumentation", *IEEE Transactions on Terahertz Science and Technology*, vol. 1, pp. 133–144, 2011.

[110] H. Hoshina, Y. Sasaki, A. Hayashi, C. Otani, and K. Kawase, "Noninvasive Mail Inspection System with Terahertz Radiation", *Applied Spectroscopy*, vol. 63, pp. 81−86, 2009.

[111] C. Jansen, S. Wietzke, O. Peters, M. Scheller, N. Vieweg, M. Salhi, N. Krumbholz, C. Jördens, T. Hochrein, and M. Koch, "Terahertz imaging: applications and perspectives," *Applied Optics*, vol. 49, pp. E48–E57, 2010.

[112] S. Zhong, Y.-C. Shen, L. Ho, R.K. May, J.A. Zeitler, M. Evans, P.F. Taday, M. Pepper, T. Rades, K.C. Gordon, R. Müller, and P. Kleinebudde, "Non-destructive quantification of pharmaceutical tablet coatings using terahertz pulsed imaging and optical coherence tomography," *Optics and Lasers in Engineering*, vol. 49, pp. 361–365, 2011.

[113] G.J. Wilmink, B.L. Ibey, T. Tongue, B. Schulkin, N. Laman, X.G. Peralta, C.C. Roth, C. Z. Cerna, B.D. Rivest, J.E. Grundt, and W.P. Roach, "Development of a compact terahertz time-domain spectrometer for the measurement of the optical properties of biological tissues," *Journal of Biomedical Optics*, vol. 16, 047006, 2011.

[114] P.H. Siegel, "Terahertz Technology in Biology and Medicine," *IEEE Transactions on Microwaves Theory and Techniques*, vol. 52, pp. 2438−2447, 2004.

[115] M. Tonouchi, "Cutting-edge terahertz technology," *Nature Photonics*, vol. 1, pp. 97−105, 2007.

[116] Daily Mail Online. “The amazing strip-search scanner,” Internet : http://www.dailymail.co.uk/sciencetech/article-455506/The-amazing-strip-search-scanner.html, [accessed: 20 Jan. 2011].

[117] J.P. Laib, and D.M. Mittleman, “Temperature-Dependent Terahertz Spectroscopy of Liquid n-alkanes,” *Journal of Infrared, Millimeter, and Terahertz Waves*, vol. 31, pp. 1015–1021, 2010.

[118] Y.S. Jin, G.J. Kim, C.H. Shon, S. Jeon, and J.I. Kim, “Analysis of Petroleum Products and Their Mixtures by Using Terahertz Time Domain Spectroscopy,” *Journal of the Korean Physical Society*, vol. 53, pp. 1879−1885, 2008.

[119] J.A. Zeitler, P.F. Taday, D.A. Newnham, M. Pepper, K.C. Gordon, and T. Rades, “Non-destructive quantification of pharmaceutical tablet coatings using terahertz pulsed imaging and optical coherence tomography,” *Journal of Pharmacy and Pharmacology*, vol. 59, pp. 209–223, 2007.

[120] S. Ebbinghaus, S.J. Kim, M. Heyden, X. Yu, M. Gruebele, D.M. Leitner, and M. Havenith, “Protein Sequence- and pH-Dependent Hydration Probed by Terahertz Spectroscopy,” *Journal of the American Chemical Society*, vol. 130, pp. 2374−2375, 2008.

[121] J. Liu, J. Dai, S.-L. Chin, and X.-C.Zhang, “Broadband terahertz wave remote sensing using coherent manipulation of fluorescence from asymmetrically ionized gases,” *Nature Photonics*, vol. 4, pp. 627−631, 2010.

[122] Y.-S. Jin, G.-J. Kim, and S.-Y. Jeon, “Terahertz dielectric properties of polymers,” *Journal of the Korean Physical Society*, vol. 49, pp. 513– 517, 2006.

[123] A. Dupuis, K. Stoeffler, B. Ung, C. Dubois, and M. Skorobogatiy, “Transmission measurements of hollow-core THz Bragg Fibers,” *Journal of the Optical Society of America B*, vol. 28, pp. 896–907, 2011.

[124] P.D. Cunningham, N.N. Valdes, F.A. Vallejo, L.M. Hayden, B. Polishak, X.-H. Zhou, J. Luo, A.K. Jen, J.C. Williams, and R.J. Twieg, “Broadband terahertz characterization of the refractive index and absorption of some important polymeric and organic electro-optic materials,” *Journal of Applied Physics*, vol. 109, 043505, 2011.

[125] M. Skorobogatiy, and J. Yang, *Fundamentals of Photonic Crystal Guiding*, New York, USA: Cambridge University Press, 2009.

[126] L.-J. Chen, H.-W. Chen, T.-F. Kao, J.-Y. Lu, and C.-K. Sun, "Low-loss subwavelength plastic fiber for terahertz waveguiding," *Optics Letters*, vol. 31, pp. 308–310, 2006.

[127] J.-Y. Lu, C.-C. Kuo, C.-M. Chiu, H.-W. Chen, Y.-J. Hwang, C.-L. Pan, and C.-K. Sun, "THz interferometric imaging using subwavelength plastic fiber based THz endoscopes," *Optics Express*, vol. 16, pp. 2494–2501, 2008.

[128] J.-Y. Lu, C.-M. Chiu, C.-C. Kuo, C.-H. Lai, H.-C. Chang, Y.-J. Hwang, C.-L. Pan, and C.-K. Sun, "Terahertz scanning imaging with a subwavelength plastic fiber," *Applied Physics Letters*, vol. 92, 084102, 2008.

[129] C.-M. Chiu, H.-W. Chen, Y.-R. Huang, Y.-J. Hwang, W.-J. Lee, H.-Y. Huang, and C.-K. Sun, "All-terahertz fiber-scanning near-field microscopy," *Optics Letters*, vol. 34, pp. 1084–1086, 2009.

[130] Y.-W. Huang, T.-F. Tseng, C.-C. Kuo, Y.-J. Hwang, and C.-K. Sun, "Fiber-based swept-source terahertz radar," *Optics Letters*, vol. 35, pp. 1344–1346, 2010.

[131] B. You, T.-A. Liu, J.-L. Peng, C.-L. Pan, and J.-Y. Lu, "A terahertz plastic wire based evanescent field sensor for high sensitivity liquid detection," *Optics Express*, vol. 17, pp. 20675–20683, 2009.

[132] B. You, J.-Y. Lu, T.-A. Liu, J.-L. Peng, and C.-L. Pan, "Subwavelength plastic wire terahertz time-domain spectroscopy," *Applied Physics Letters*, vol. 96, 051105, 2010.

[133] M. Nagel, A. Marchewka, and H. Kurz, "Low-index discontinuity terahertz waveguides," *Optics Express*, vol. 14, pp. 9944–9954, 2006.

[134] A. Hassani, A. Dupuis, and M. Skorobogatiy, "Low loss porous terahertz fibers containing multiple subwavelength holes," *Applied Physics Letters*, vol. 92, 071101, 2008.

[135] A. Hassani, A. Dupuis, and M. Skorobogatiy, "Porous polymer fibers for low-loss Terahertz guiding," *Optics Express*, vol. 16, pp. 6340–6351, 2008.

[136] A. Dupuis, J.-F. Allard, D. Morris, K. Stoeffler, C. Dubois, and M. Skorobogatiy, "Fabrication and THz loss measurements of porous subwavelength fibers using a directional coupler method," *Optics Express*, vol. 17, pp. 8012– 8028, 2009.

[137] A. Dupuis, A. Mazhorova, F. Désévédavy, M. Rozé, and M. Skorobogatiy, "Spectral characterization of porous dielectric subwavelength THz fibers fabricated using a microstructured molding technique," *Optics Express*, vol. 18, pp. 13813–13828, 2010.

[138] S. Atakaramians, S. Afshar V, H. Ebendorff-Heidepriem, M. Nagel, B. M. Fischer, D. Abbott, and T. M. Monro, "THz porous fibers: design, fabrication and experimental characterization," *Optics Express*, vol. 17, pp. 14053–15062, 2009.

[139] M. Rozé*, B. Ung*, A. Mazhorova, M. Walther, and M. Skorobogatiy, "Suspended core subwavelength fibers: towards practical designs for low-loss terahertz guidance," *Optics Express*, vol. 19, pp. 9127–9138, 2011. (**These authors contributed equally to the paper*)

[140] C.S. Ponseca Jr., R. Pobre, E. Estacio, N. Sarukura, A. Argyros, M.C.J. Large, and M.A. van Eijkelenborg, "Transmission of terahertz radiation using a microstructured polymer optical fiber," *Optics Letters*, vol. 33, pp. 902–904, 2008.

[141] J. Anthony, R. Leonhardt, S.G. Leon-Saval, and A. Argyros, "THz propagation in kagome hollow-core microstructured fibers," *Optics Express*, vol. 19, pp. 18470–18478, 2011.

[142] K. Nielsen, H.K. Rasmussen, P.U. Jepsen, and O. Bang, "Porous-core honeycomb bandgap THz fiber," *Optics Letters*, vol. 36, pp. 666–668, 2011.

[143] H. Han, H. Park, M. Cho, and J. Kim, "Terahertz pulse propagation in a plastic photonic crystal fiber," *Applied Physics Letters*, vol. 80, pp. 2634–2636, 2002.

[144] M. Goto, A. Quema, H. Takahashi, S. Ono, and N. Sarukura, "Teflon Photonic Crystal Fiber as Terahertz Waveguide," *Japanese Journal of Applied Physics*, vol. 43, pp. L317–L319, 2004.

[145] K. Nielsen, H.K. Rasmussen, A.J.L. Adam, P.C.M. Planken, O. Bang, and P.U. Jepsen, "Bendable, low-loss Topas fibers for the terahertz frequency range," *Optics Express*, vol. 17, pp. 8592–8601, 2009.

[146] M. A Duguay, Y. Kokubun, T. L. Koch, and L. Pfeiffer, "Antiresonant reflecting optical waveguides in SiO_2- Si multilayer structures," *Applied Physics Letters*, vol. 49, pp. 13–15, 1986.

[147] C.-H. Lai, Y.-C. Hsueh, H.-W. Y.-J. Huang, Chen, H.-C. Chang, and C.-K. Sun, "Low-index terahertz pipe waveguides," *Optics Letters*, vol. 34, pp. 3457–3459, 2009.

[148] C.-H. Lai, B. You, J.-Y. Lu, T.-A. Liu, J.-L. Peng, C.-K. Sun, and H.-C. Chang, "Modal characteristics of antiresonant reflecting pipe waveguides for terahertz waveguiding," *Optics Express*, vol. 18, pp. 309–322, 2010.

[149] A. Dupuis, "Dielectric THz waveguides", *Ph.D. thesis*, Ecole Polytechnique de Montréal, Department of engineering physics, 2010.

[150] M. Skorobogatiy, and A. Dupuis, "Ferroelectric all-polymer hollow Bragg fibers for terahertz guidance," *Applied Physics Letters*, vol. 90, 113514, 2007.

[151] B. Ung, A. Dupuis, K. Stoeffler, C. Dubois, and M. Skorobogatiy, "High-refractive-index composite materials for terahertz waveguides: trade-off between index contrast and absorption loss," *Journal of the Optical Society of America B*, vol. 28, pp. 917– 921, 2011.

[152] A. Dupuis, K. Stoeffler, B. Ung, C. Dubois, and M. Skorobogatiy, "Transmission measurements of hollow-core THz Bragg fibers," *Journal of the Optical Society of America B*, vol. 28, pp. 896−907, 2011.

[153] A. Argyros, "Microstructured Polymer Optical Fibers," *Journal of Lightwave Technology*, vol. 27, pp. 1571−1579, 2009.

[154] G. Barton, M.A. van Eijkelenborg, G. Henry, M.C.J. Large, and J. Zagari , "Microstructured Polymer Optical Fibers," *Optical Fiber Technology*, vol. 10, pp. 325−335, 2004.

[155] Y. Zhang, K. Li, L. Wang, L. Ren, W. Zhao, R. Miao, M.C.J. Large, and M.A. van Eijkelenborg, "Casting preforms for microstructured polymer optical fibre fabrication," *Optics Express*, vol. 14, pp. 5541–5547, 2006.

[156] H. Ebendorff-Heidepriem, T.M. Monro, M.A. van Eijkelenborg, and M.C.J. Large, "Extruded high-NA microstructured polymer optical fibre," *Optics Communications*, vol. 273, pp. 133–137, 2007.

[157] L. Kang, L. Wang, X. Yang, and J. Wang, "Mass-fabrication of Air-core Microstructured Polymer Optical Fiber," in *Conference on Lasers and Electro-Optics (CLEO)*, 2008, paper CTuMM4.

[158] G.S. Wiederhecker, C.M.B. Cordeiro, F. Couny, F. Benabid, S.A. Maier, J.C. Knight, C.H.B. Cruz, and H.L. Fragnito, "Field enhancement within an optical fibre with a subwavelength air core," *Nature Photonics*, vol. 1, pp. 115–118, 2007.

[159] Y. Ruan, H. Ebendorff-Heidepriem, S. Afshar, and T.M. Monro, "Light confinement within nanoholes in nanostructured optical fibers," *Optics Express*, vol. 18, pp. 26018–26026, 2010.

[160] M.A. Foster, A.C. Turner, M. Lipson, and A.L. Gaeta, "Nonlinear optics in photonic nanowires," *Optics Express*, vol. 16, pp. 1300–1320, 2008.

[161] G. Brambilla, F. Xu, P. Horak, Y. Jung, F. Koizumi, N.P. Sessions, E. Koukharenko, X. Feng, G.S. Murugan, J.S. Wilkinson, and D.J. Richardson, "Optical fiber nanowires and microwires: fabrication and applications," *Advances in Optics and Photonics*, vol. 1, pp. 107–161, 2009.

[162] T. Koga, Y. Namihira, T. Kinjo, S.F. Kaijage, S.M. Abdur-Razzak, and S. Nozaki, "Highly nonlinear photonic crystal fiber with refractive index core for dental OCT applications," *Proceedings of SPIE*, vol. 7609, no. 760910, 2010.

[163] J. Hou, D. Bird, A. George, S.A. Maier, B.T. Kuhlmey, and J.C. Knight, "Metallic mode confinement in microstructured fibres," *Optics Express*, vol. 16, pp. 5983–5990, 2008.

[164] M.A. Schmidt, H. Tyagi, H. Lee, and P. St. J. Russell, "Novel Nanophotonic Waveguides Based on Metal, Semiconductor or Soft Glass Modified Photonic Crystal Fibres," in *International Conference on Transparent Optical Networks (ICTON)*, 2009, paper We.A5.2.

[165] D. Chen, "Cylindrical hybrid plasmonic waveguide for subwavelength confinement of light," *Applied Optics*, vol. 49, pp. 6868–6871, 2010.

[166] N. Granzow, P. Uebel, M.A. Schmidt, A.S. Tverjanovich, L. Wondraczek, and P. St. J. Russell, "Bandgap guidance in hybrid chalcogenide–silica photonic crystal fibers," *Optics Letters*, vol. 36, pp. 2432–2434, 2011.

[167] T.X. Tran, and F. Biancalana, "An accurate envelope equation for light propagation in photonic nanowires: new nonlinear effects," *Optics Express*, vol. 17, pp. 17934–17949, 2009.

[168] F. Biancalana, T.X. Tran, S. Stark, M.A. Schmidt, and P. St. J. Russell, "Emergence of Geometrical Optical Nonlinearities in Photonic Crystal Fiber Nanowires," *Physical Review Letters*, vol. 105, 093904, 2010.

[169] C.J. Barrelet, H.-S. Ee, S.-H. Kwon, and H.-G. Park, "Nonlinear Mixing in Nanowire Subwavelength Waveguides," *Nano Letters*, vol. 11, 3022–3025, 2011.

[170] B. Ung, and M. Skorobogatiy, "Chalcogenide Microporous Fibers for Nonlinear Applications in Mid-Infrared," in *Conference on Lasers and Electro-Optics (CLEO)*, 2010, paper CTuT5.

[171] B. Ung, and M. Skorobogatiy, "Chromatic dispersion engineering in chalcogenide microporous fibers for the middle-infrared," in *Specialty Optical Fibers Conference (SOF), OSA Technical Digest*, 2011, paper SOTuB3.

[172] M. Moenster, G. Steinmeyer, R. Iliew, F. Lederer, and K. Petermann, "Analytical relation between effective mode field area and waveguide dispersion in microstructure fibers," *Optics Letters*, vol. 31, pp. 3249–3251, 2006.

[173] Y.H. Chen, S. Varma, I. Alexeev, and H.M. Milchberg, "Measurement of transient nonlinear refractive index in gases using xenon supercontinuum single-shot spectral interferometry," *Optics Express*, vol. 15, pp. 7458–7467, 2007.

[174] J. Hu, C. R. Menyuk, L. B. Shaw, J. S. Sanghera, and I. D. Aggarwal, "Raman response function and supercontinuum generation in chalcogenide fiber," in *Conference on Lasers and Electro-Optics (CLEO)*, 2008, Paper CMDD2.

[175] W.L. Barnes, A Dereux, and T.W. Ebbesen, "Surface plasmon subwavelength optics," *Nature*, vol. 424, pp. 824–830, 2003.

[176] A. Hassani, B. Gauvreau, M. F. Fehri, A. Kabashin, and M. Skorobogatiy, "Photonic Crystal Fiber and Waveguide-Based Surface Plasmon Resonance Sensors for Application in the Visible and Near-IR," *Electromagnetics*, vol. 28, pp. 198–213, 2008.

[177] B. Gauvreau, A. Hassani, M. F. Fehri, A. Kabashin, and M. Skorobogatiy, "Photonic bandgap fiber-based Surface Plasmon Resonance sensors," *Optics Express*, vol. 15, pp. 11413–11426, 2007.

[178] R. Kashyap, and G. Nemova, "Surface Plasmon Resonance-Based Fiber and Planar Waveguide Sensors," *Journal of Sensors*, vol. 2009, 645162, 2009.

[179] S. Patskovsky, A.V. Kabashin, M. Meunier, and J.H.T. Luong, "Silicon-based surface plasmon resonance sensing with two surface plasmon polariton modes," *Applied Optics*, vol. 42, pp. 6905–6909, 2003.

[180] Y. Shevchenko, T.J. Francis, D.A.D. Blair, R. Walsh, M.C. DeRosa, and J. Albert, "In Situ Biosensing with a Surface Plasmon Resonance Fiber Grating Aptasensor," *Analytical Chemistry*, vol. 83, pp. 7027–7034, 2011.

[181] S.I. Bozhevolnyi, V.S. Volkov, E. Devaux, and T.W. Ebbesen, "Channel Plasmon-Polariton Guiding by Subwavelength Metal Grooves," *Physical Review Letters*, vol. 95, 046802, 2005.

[182] M.L. Brongersma, R. Zia, and J.A. Schuller, "Plasmonics – the missing link between nanoelectronics and microphotonics," *Applied Physics A*, vol. 89, pp. 221–223, 2007.

[183] E. Moreno, S. G. Rodrigo, S. I. Bozhevolnyi, L. Martin- Moreno, and F. J. Garcia-Vidal, "Guiding and Focusing of Electromagnetic Fields with Wedge Plasmon Polaritons," *Physical Review Letters*, vol. 100, 023901, 2008.

[184] P. Berini, "Long-range surface plasmon polaritons," *Advances in Optics and Photonics*, vol. 1, pp. 484–588, 2009.

[185] S.A. Maier, M.L. Brongersma, P.G. Kik, S. Meltzer, A.A.G. Requicha, and H.A. Atwater, "Plasmonics- A Route to Nanoscale Optical Devices," *Advanced Materials*, vol. 13, pp. 1501–1505, 2001.

[186] E.J. Smythe, E. Cubukcu, and F. Capasso, "Optical properties of surface plasmon resonances of coupled metallic nanorods," *Optics Express*, vol. 15, pp. 7439–7447, 2007.

[187] J.A. Schuller, E.S. Barnard, W. Cai, Y.C. Jun, J.S. White, and M.L. Brongersma, "Plasmonics for extreme light concentration and manipulation," *Nature Materials*, vol. 9, pp. 193–205, 2010.

[188] K.F. MacDonald and N.I. Zheludev, "Active plasmonics: current status," *Laser & Photonics Reviews*, vol. 4, pp. 562–567, 2010.

[189] M.I. Stockman, "Nanoplasmonics: past, present, and glimpse into future," *Optics Express*, vol. 19, pp. 22029–22106, 2011.

[190] A. Degiron, C. Dellagiacoma, J.G. McIlhargey, G. Shvets, O.J.F. Martin, and D.R. Smith, "Simulations of hybrid long-range plasmon modes with application to 90° bends," *Optics Letters*, vol. 32, pp. 2354–2356, 2007.

[191] R.F. Oulton, V.J. Sorger, D.A. Genov, D.F.P. Pile, and X. Zhang, "A hybrid plasmonic waveguide for subwavelength confinement and long-range propagation," *Nature Photonics*, vol. 2, pp. 496–500, 2008.

[192] P.D. Flammer, J.M. Banks, T.E. Furtak, C.G. Durfee, R.E. Hollingsworth, and R.T. Collins, "Hybrid plasmon/dielectric waveguide for integrated silicon-on-insulator optical elements," *Optics Express*, vol. 18, pp. 21013–21023, 2010.

[193] V.J. Sorger, Z. Ye, R.F. Oulton, Y. Wang, G. Bartal, X. Yin, and X. Zhang, "Experimental demonstration of low-loss optical waveguiding at deep sub-wavelength scales," *Nature Communications*, vol. 2, pp. 331–335, 2011.

[194] M.A. Schmidt, L.N. Prill Sempere, H.K. Tyagi, C.G. Poulton, and P.St.J. Russell, "Waveguiding and plasmon resonances in two-dimensional photonic lattices of gold and silver nanowires," *Physical Review B*, vol. 77, 033417, 2008.

[195] A. Manjavacas, and F.J.G. Abajo, "Coupling of gap plasmons in multi-wire waveguides," *Optics Express*, vol. 17, pp. 19401–19413, 2009.

[196] Z.-X. Zhang, M.-L. Hu, K.T. Chan, and C.-Y. Wang, "Plasmonic waveguiding in a hexagonally ordered metal wire array," *Optics Letters*, vol. 35, pp. 3901–3903, 2010.

[197] P.J. Schuck, D.P. Fromm, A. Sundaramurthy, G.S. Kino, and W.E. Moerner, "Improving the Mismatch between Light and Nanoscale Objects with Gold Bowtie Nanoantennas," *Physical Review Letters*, vol. 94, 017402, 2005.

[198] N. Yu, E. Cubukcu, L. Diehl, D. Bour, S. Corzine, J. Zhu, G. Höfler, K.B. Crozier, and F. Capasso, "Bowtie plasmonic quantum cascade laser antenna," *Optics Express*, vol. 15, pp. 13272–13281, 2007.

[199] H. Fischer, and O.J.F. Martin, "Engineering the optical response of plasmonic nanoantennas," *Optics Express*, vol. 16, pp. 9144–9154, 2008.

[200] A. Kinkhabwala, Z. Yu, S. Fan, Y. Avlasevich, K. Müllen, and W.E. Moerner, "Large single-molecule fluorescence enhancements produced by a bowtie nanoantenna," *Nature Photonics*, vol. 3, 654–657, 2009.

[201] N.A. Hatab, C.-H. Hsueh, A.L. Gaddis, S.T. Retterer, J.-H. Li, G. Eres, Z. Zhang, and B. Gu, "Free-Standing Optical Gold Bowtie Nanoantenna with Variable Gap Size for Enhanced Raman Spectroscopy," *Nano Letters*, vol. 10, pp. 4952–4955, 2010.

[202] D.R. Ward, F. Huser, F. Pauly, J. Carlos-Cuevas, and D. Natelson, "Optical rectification and field enhancement in a plasmonic nanogap," *Nature Nanotechnology*, vol. 5, pp. 732–736, 2010.

[203] S. Sederberg, and A.Y. Elezzabi, "Nanoscale plasmonic contour bowtie antenna operating in the mid-infrared," *Optics Express*, vol. 19, pp. 15532–15537, 2011.

[204] A. Mazhorova, J.F. Gu, A. Dupuis, M. Peccianti, O. Tsuneyuki, R. Morandotti, H. Minamide, M. Tang, Y. Wang, H. Ito, and M. Skorobogatiy, "Composite THz materials using aligned metallic and semiconductor microwires, experiments and interpretation," *Optics Express*, vol. 18, pp. 24632–24647, 2010.

[205] M. Yaman, T. Khudiyev, E. Ozgur, M. Kanik, O. Aktas, E.O. Ozgur, H. Deniz, E. Korkut, and M. Bayindir, "Arrays of indefinitely long uniform nanowires and nanotubes," *Nature Materials*, vol. 10, pp. 494–501, 2011.

[206] H.K. Tyagi, H.W. Lee, P. Uebel, M.A. Schmidt, N. Joly, M. Scharrer, and P.St.J. Russell, "Plasmon resonances on gold nanowires directly drawn in a step-index fiber," *Optics Letters*, vol. 35, pp. 2573–2575, 2010.

[207] P. Wang, Y. Lu, L. Tang, J. Zhang, H. Ming, J. Xie, F.-H. Ho, H.-H. Chang, H.-Y. Lin, and D.-P. Tsai, "Surface-enhanced optical nonlinearity of a gold film," *Optics Communications*, vol. 229, pp. 425–429, 2004.

[208] G. Colas des Francs, P. Bramant, J. Grandidier, A. Bouhelier, J.-C. Weeber, and A. Dereux, "Optical gain, spontaneous and stimulated emission of surface plasmon polaritons in confined plasmonic waveguide," *Opics Express*, vol. 18, 16327–16334, 2010.

[209] C. Jansen, S. Wietzke, V. Astley, D.M. Mittleman, and M. Koch, "Mechanically flexible polymeric compound one-dimensional photonic crystals for terahertz frequencies," *Applied Physics Letters*, vol. 96, 111108, 2010.

[210] S. Wietzke, C. Jansen, F. Rutz, D.M. Mittleman, and M. Koch, "Determination of additive content in polymeric compounds with terahertz time-domain spectroscopy," *Polymer Testing*, vol. 26, pp. 614–618, 2007.

[211] M. Scheller, S. Wietzke, C. Jansen, and M. Koch, "Modelling heterogeneous dielectric mixtures in the terahertz regime: a quasi- static effective medium theory," *Journal of Physics D: Applied Physics*, vol. 42, 065415, 2009.

[212] P. Yeh, A. Yariv, and E. Marom, "Theory of Bragg fiber," *Journal of the Optical Society of America*, vol. 68, pp. 1196–1201, 1978.

[213] M. Skorobogatiy, "Efficient antiguiding of TE and TM polarizations in low-index core waveguides without the need for an omnidirectional reflector," *Optics Letters*, vol. 30, pp. 2991–2993, 2005.

[214] E. Garmire, "Theory of quarter-wave-stack dielectric mirrors used in a thin Fabry–Perot filter," *Applied Optics*, vol. 42, pp. 5442–5449, 2003.

[215] O. Mitrofanov, T. Tan, P.R. Mark, B. Bowden, and J.A. Harrington, "Waveguide mode imaging and dispersion analysis with terahertz near-field microscopy," *Applied Physics Letters*, vol. 94, 171104, 2009.

[216] J. R. Knab, A. J. L. Adam, R. Chakkittakandy, and P. C. M. Planken, "Terahertz near-field microspectroscopy," *Applied Physics Letters*, vol. 97, 031115, 2010.

[217] A. Bitzer, A. Ortner, and M. Walther, "Terahertz near-field microscopy with subwavelength spatial resolution based on photoconductive antennas," *Applied Optics*, vol. 49, pp. E1–E6, 2010.

[218] M. Walther and A. Bitzer, "Electromagnetic Wave Propagation Close to Microstructures Studied by Time and Phase-Resolved THz Near-Field Imaging," *Journal of Infrared, Millimeter, and Terahertz Waves*, vol. 32, pp. 1020–1030, 2011.

[219] J. Anthony, R. Leonhardt, A. Argyros, and M.C.J. Large, "Characterization of a microstructured Zeonex terahertz fiber," *Journal of the Optical Society of America B*, vol. 28, pp. 1013–1018, 2011.

[220] J.S. Sanghera, I.D. Aggarwal, L.B. Shaw, C.M. Florea, P.Pureza, V.Q. Nguyen, and F. Kung, "Nonlinear properties of chalcogenide glass fibers," *Journal of Optoelectronics and Advanced Materials*, vol. 8, pp. 2148–2155, 2006.

[221] D.J. Moss, Y. Miao, V. Ta'eed, E.C. Mägi, and B.J. Eggleton, "Coupling to high-index waveguides via tapered microstructured optical fibre," *Electronics Letters*, vol. 41, pp. 951–953, 2005.

[222] E.C. Mägi, L.B. Fu, H.C. Nguyen, M.R.E. Lamont, D.I. Yeom, and B.J. Eggleton, "Enhanced Kerr nonlinearity in sub-wavelength diameter As_2Se_3 chalcogenide fiber tapers," *Optics Express*, vol. 15, pp. 10324–10329, 2007.

[223] F. Couny, and F. Benabid, "Optical frequency comb generation in gas-filled hollow core photonic crystal fibres," *Journal of Optics A: Pure and Applied Optics*, vol. 11, pp. 103002, 2009.

[224] J.C. Travers, W. Chang, J. Nold, N.Y. Joly, and P.St.J. Russell, "Ultrafast nonlinear optics in gas-filled hollow-core photonic crystal fibers [Invited]," *Journal of the Optical Society of America B*, vol. 28, pp. A11–A26, 2011.

[225] R. Buczynski, D. Pysz, R. Stepien, A.J. Waddie, I. Kujawa, R. Kasztelanic, M. Franczyk, and M.R. Taghizadeh, "Supercontinuum generation in photonic crystal fibers with nanoporous core made of soft glass," *Laser Physics Letters*, vol. 8, pp. 443–448, 2011.

[226] R. Buczynski, D. Pysz, R. Stepien, R. Kasztelanic, I. Kujawa, M. Franczyk, A. Filipkowski, A.J. Waddie, and M.R. Taghizadeh, "Supercontinuum generation in photonic

crystal fibers with nanoporous core made of soft glass," *Journal of the European Optical Society: Rapid Publications*, vol. 6, 11038, 2011.

[227] E.C. Garnett, W. Cai, J.J. Cha, F. Mahmood, S.T. Connor, M. Greyson Christoforo, Y. Cui, M.D. McGehee, and M.L. Brongersma, "Self-limited plasmonic welding of silver nanowire junctions," *Nature Materials*, vol. 11, pp. 241–249, 2012.

[228] M. Moskovits, "Spot the hotspot: plasmonic hotspots," *Nature*, vol. 469, pp. 307–308, 2011.

[229] J.D. Caldwell, O.J. Glembocki, F.J. Bezares, M.I. Kariniemi, J.T. Niinistö, T.T. Hatanpää, R.W. Rendell, M. Ukaegbu, M.K. Ritala, S.M. Prokes, C.M. Hosten, M.A. Leskelä, and R. Kasica, "Large-area plasmonic hot-spot arrays: sub-2 nm interparticle separations with plasma-enhanced atomic layer deposition of Ag on periodic arrays of Si nanopillars," *Optics Express*, vol. 19, pp. 26056–26064, 2011.

[230] S. Link, C. Burda, Z.L. Wang, and M.A. El-Sayed, "Electron dynamics in gold and gold–silver alloy nanoparticles: The influence of a nonequilibrium electron distribution and the size dependence of the electron–phonon relaxation," *Journal of Chemical Physics*, vol. 111, pp. 1255–1264, 1999.

[231] W. Zhang, S.H. Brongersma, O. Richard, B. Brijs, R. Palmans, L. Froyen, and K. Maex, "Influence of the electron mean free path on the resistivity of thin metal films," *Microelectronic Engineering*, vol. 76, pp. 146–152, 2004.

[232] J.D. Jackson, "Chapter 5.18: Quasi-static magnetic fields in conductors; Eddy currents; Magnetic diffusion," in *Classical Electrodynamics (Third Edition)*, New Jersey, USA: John Wiley & Sons, 1999.

[233] P.W. Gilberd, "The anomalous skin effect and the optical properties of metals," *Journal of Physics F: Metal Physics*, vol. 12, pp. 1845–1860, 1982.

[234] B.G. Martin, A.A. Maradudin, and R.F. Wallis, "Theory of surface polaritons associated with the extreme anomalous skin effect in normal and superconducting metals," *Solid State Communications*, vol. 40, pp. 479–482, 1981.

[235] A. Tsiatmas, A.R. Buckingham, V.A. Fedotov, S. Wang, Y. Chen, P.A.J. de Groot, and N.I. Zheludev, "Superconducting plasmonics and extraordinary transmission," *Applied Physics Letters*, vol. 97, 111106, 2010.

[236] A. Tsiatmas, V.A. Fedotov, and N.I. Zheludev, "Plasmonics without losses? (the case for terahertz superconducting plasmonics)," *arXiv*, 1105.3045, 2011.

[237] A. Tsiatmas, V.A. Fedotov, and N.I. Zheludev, "Superconducting Analogue of Optical Plasmonic Waveguides," in *CLEO/Europe and EQEC 2011 Conference Digest, OSA Technical Digest*, 2011, paper EJ1_6.

[238] R.F. Oulton, V.J. Sorger, T. Zentgraf, R.-M. Ma, C. Gladden, L. Dai, G. Bartal, and X. Zhang, "Plasmon lasers at deep subwavelength scale," *Nature*, vol. 461, pp. 629–632, 2009.

[239] J. Grandidier, G. Colas des Francs, S. Massenot, A. Bouhelier, L. Markey, J.-C. Weeber, C. Finot, and A. Dereux, "Gain-Assisted Propagation in a Plasmonic Waveguide at Telecom Wavelength," *Nano Letters*, vol. 9, pp. 2935–2939, 2009.

[240] I. De Leon, and P. Berini, "Amplification of long-range surface plasmons by a dipolar gain medium," *Nature Photonics*, vol. 4, pp. 382–387, 2010.

[241] M.I. Stockman, "Spaser Action, Loss Compensation, and Stability in Plasmonic Systems with Gain," *Physical Review Letters*, vol. 106, 156802, 2011.

[242] J. Zhang, L. Cai, W. Bai, Y. Xu, and G. Song, "Hybrid plasmonic waveguide with gain medium for lossless propagation with nanoscale confinement," *Optics Letters*, vol. 36, pp. 2312–2314, 2011.

[243] S.M. García-Blanco, M. Pollnau, and S.I. Bozhevolnyi, "Loss compensation in long-range dielectric-loaded surface plasmon-polariton waveguides," *Optics Express*, vol. 19, pp. 25298–25310, 2011.

[244] A.A.E. Saleh, and J.A. Dionne, "Waveguides with a silver lining: Low threshold gain and giant modal gain in active cylindrical and coaxial plasmonic devices," *Physical Review B*, vol. 85, 045407, 2012.

[245] P. Berini, and I. De Leon, "Surface plasmon–polariton amplifiers and lasers," *Nature Photonics*, vol. 6, pp. 16–14, 2012.

[246] T. Durkop, S.A. Getty, E. Cobas, and M.S. Fuhrer, "Extraordinary Mobility in Semiconducting Carbon Nanotubes," *Nano Letters*, vol. 4, pp. 35–39, 2004.

[247] F. Bonaccorso, Z. Sun, T. Hasan, and A.C. Ferrari, "Graphene photonics and optoelectronics," *Nature Photonics*, vol. 4, pp. 611–622, 2010.

[248] A. Boltasseva, and H.A. Atwater, "Low-Loss Plasmonic Metamaterials," *Science*, vol. 331, pp. 290–291, 2011.

[249] L. Thylen, P. Holmström, E Berglind, M. Yan, D. Dai, L. Wosinski, and A Bratkovsky, "Complementing or Replacing Silicon and III-Vs: The Role of Plasmonics and Novel Materials in Future Integrated Photonics for Telecom and Interconnects," in *International Conference on Transparent Optical Networks (ICTON)*, 2011, paper Mo.C2.1.

[250] F.H.L. Koppens, D.E. Chang, and F.J. García de Abajo, "Graphene Plasmonics: A Platform for Strong Light-Matter Interactions," *Nano Letters*, vol. 11, pp. 3370–3377, 2011.

[251] W. Zhou, J. Lee, J. Nanda, S.T. Pantelides, S.J. Pennycook, and J.-C. Idrobo, "Atomically localized plasmon enhancement in monolayer graphene," *Nature Nanotechnology*, vol. 7, pp. 161–165, 2012.

[252] T. Stauber and G. Gomez-Santos, "Plasmons and near-field amplification in double-layer graphene," *Physical Review B*, vol. 85, 075410, 2012.

[253] S. Yamashita, "A Tutorial on Nonlinear Photonic Applications of Carbon Nanotube and Graphene," *Journal of Lightwave Technology*, vol. 30, pp. 427–447, 2012.

[254] P. Tassin, T. Koschny, M. Kafesaki, and C.M. Soukoulis, "A comparison of graphene, superconductors and metals as conductors for metamaterials and plasmonics," *Nature Photonics*, vol. 6, pp. 259–264, 2012.

[255] J.A. Rogers, M.G. Lagally, and R.G. Nuzzo, "Synthesis, assembly and applications of semiconductor nanomembranes," *Nature*, vol. 477, pp. 45–53, 2011.

[256] R. Rao, D. Liptak, T. Cherukuri, B.I. Yakobson, and B. Maruyama, "In situ evidence for chirality-dependent growth rates of individual carbon nanotubes," *Nature Materials*, vol. 11, pp. 213–216, 2012.

[257] O.O. Kit, T. Tallinen, L. Mahadevan, J. Timonen, and P. Koskinen, "Twisting graphene nanoribbons into carbon nanotubes," *Physical Review B*, vol. 85, 085428, 2012.

[258] J.-U. Park, S.W. Nam, M.-S. Lee, and C.M. Lieber, "Synthesis of monolithic graphene–graphite integrated electronics," *Nature Materials*, vol. 11, pp. 120–125, 2012.

[259] T. Dumitrica, S. Kodambaka, and S. Jun, "Synthesis, electromechanical characterization, and applications of graphene nanostructures," *Journal of Nanophotonics*, vol. 6, 064501, 2012.

[260] R. Van Noorden, "Producing graphene: Beyond sticky tape," *Nature*, vol. 483, pp. S32–S33, 2012.

[261] D.Q. Wu, J.S. Bloom, and J.D. Connolly, "Coating compositions having improved solar reflectivity and UV protection," *United States Patent*, US 2011/0151244 A1, 2011.

[262] S. Atakaramians, K. Cook, H. Ebendorff-Heidepriem, S. Afshar-V., J. Canning, D. Abbott, and T.M. Monro, "Cleaving of Extremely Porous Polymer Fibers," *IEEE Photonics Journal*, vol. 1, pp. 286–292, 2009.

[263] A. Stefani, K. Nielsen, H.K. Rasmussen, and O. Bang, "Cleaving of TOPAS and PMMA microstructured polymer optical fibers: Core-shift and statistical quality optimization," *Optics Communications*, vol. 285, pp. 1825–1833, 2012.

[264] B. Ung, M. Rozé, A. Mazhorova, M. Walther, and M. Skorobogatiy, "Suspended core polymer fibers with isolated mode for terahertz guiding," in *Conference on Lasers and Electro-Optics (CLEO)*, 2011, paper CThN4.

[265] S.C. Warren-Smith, H. Ebendorff-Heidepriem, T.C. Foo, R. Moore, C. Davis, and T.M. Monro, "Exposed-core microstructured optical fibers for real-time fluorescence sensing," *Optics Express*, vol. 17, pp. 18533–18542, 2009.

[266] T. Palmisano, F. Prudenzano, S.C. Warren-Smith, and T.M. Monro, "Design of exposed-core fiber for methadone monitoring in biological fluids," *Journal of Non-Crystalline Solids*, vol. 357, pp. 2000–2004, 2011.

[267] A, Mazhorova, A. Markov, A. Ng, R. Chinnappan, O. Skorobogata, M. Zourob, and M. Skorobogatiy, “Label-free bacteria detection using evanescent mode of a suspended core terahertz fiber,” *Optics Express*, vol. 20, pp. 5344–5355, 2011.

[268] A. Mazhorova, A. Markov, A. Ng, R. Chinnappan, M. Zourob, and M. Skorobogatiy, “Label-free bacteria detection using evanescent mode of a suspended core terahertz fiber,” in *Conference on Lasers and Electro-Optics (CLEO)*, 2012, paper CTu3B.6.

[269] G. S. Warren, and W. R. Scott Jr., “Numerical Dispersion of Higher Order Nodal Elements in the Finite-Element Method,” *IEEE Transactions of Antennas and Propagations*, vol. 44, pp. 317–320, 1996.

[270] J.-Y. Wu, D. M. Kingsland, J.-F. Lee, and R. Lee, “A Comparison of Anisotropic PML to Berenger’s PML and Its Application to the Finite-Element Method for EM Scattering,” *IEEE Transactions of Antennas and Propagations*, vol. 45, pp. 40–50, 1997.

[271] V. Zakharov, and A. Shabat, “An integration scheme for the nonlinear equations of mathematical physics by the method of the Inverse scattering problem,” *Functional Analysis and Its Applications*, vol. 8, pp. 43–54, 1974.

[272] A. Hasegawa, and F. Tappert, “Transmission of stationary nonlinear optical pulses in dispersive dielectric fibers. I. Anomalous dispersion,” *Applied Physics Letters*, vol. 23, pp. 142–144, 1973.

[273] R. H. Harding, and F. Tappert, “Applications of the split-step Fourier method to the numerical solution of nonlinear and variable coefficient wave equations,” *SIAM Review*, vol. 15, no. 423, 1973.

[274] O. V. Sinkin, R. Holzlöhner, J. Zweck, and C. R. Menyuk, “Optimization of the Split-Step Fourier Method in Modeling Optical-Fiber Communications Systems,” *Journal of Lightwave Technology*, vol. 21, pp. 61–68, 2003.

[275] S. Atakaramians, S. Afshar V., M. Nagel, H. K. Rasmussen, O. Bang, T. M. Monro, and D. Abbott, “Direct probing of evanescent field for characterization of porous terahertz fibers,” *Applied Physics Letters*, vol. 98, 121104, 2011.

APPENDIX A : LIST OF PUBLICATIONS

Below is the full list of contributed publications and conference proceedings produced during the course of this doctoral thesis.

Peer-reviewed journal articles:

1. **B. Ung** and M. Skorobogatiy, "Chalcogenide microporous fibers for linear and nonlinear applications in the mid-infrared," *Optics Express*, vol. 18, no. 8 (2010)
2. H. Qu, **B. Ung**, I. Syed, N. Guo, and M. Skorobogatiy, "Photonic bandgap fiber bundle spectrometer", *Applied Optics*, vol. 49, no. 25 (2010)
3. A. Dupuis, **B. Ung**, A. Mazhorova, M. Rozé and M. Skorobogatiy, "Transmission measurements of hollow-core THz Bragg Fibers," *J. Opt. Soc. Am. B*, vol. 28, no. 4 (2011)
4. **B. Ung**, A. Dupuis, K. Stoeffler, C. Dubois, and M. Skorobogatiy, "High refractive index composite materials for THz waveguides: trade-off between index contrast and absorption loss," *J. Opt. Soc. Am. B*, vol. 28, no. 4 (2011)
5. M. Rozé*, **B. Ung***, A. Mazhorova, M. Walther, and M. Skorobogatiy, "Suspended core subwavelength fibers: towards practical designs for low-loss terahertz guidance," *Optics Express*, vol. 19, no. 10 (2011)
6. A. Markov, C. Reinhardt, **B. Ung**, A. Evlyukhin, W. Cheng, B. Chichkov, and M. Skorobogatiy, "Photonic bandgap plasmonic waveguides," *Optics Letters*, vol. 36, no. 13 (2011)
7. **B. Ung**, and M. Skorobogatiy, "Extreme nonlinear optical enhancement in chalcogenide glass fibers with deep-subwavelength metallic nanowires," *Optics Letters*, vol. 36, no. 13 (2011)
8. **B. Ung**, and M. Skorobogatiy, "Extreme optical nonlinearities in chalcogenide glass fibers embedded with metallic and semiconductor nanowires," *Applied Physics Letters*, vol. 99, 121102 (2011)
9. **B. Ung***, M. Rozé*, A. Mazhorova, M. Walther, and M. Skorobogatiy, "Suspended core subwavelength fibers for THz guidance," *Optics Photonics News*, Special issue: *Optics in 2011*, December (2011)
10. **B. Ung**, A. Mazhorova, A. Dupuis, M. Rozé, and M. Skorobogatiy, "Polymer microstructured optical fibers for terahertz wave guiding," *Optics Express*, vol. 19, no. 26 (2011)
11. H. Qu, **B. Ung**, M. Rozé, and M. Skorobogatiy, "All photonic bandgap fiber spectroscopic system for detection of refractive index changes in aqueous analytes," *Sensors and Actuators B: Chemical*, vol. 161, pp. 235-243 (2012)
12. A. Mazhorova, A. Markov, **B. Ung**, M. Rozé, S. Gorgutsa, and M. Skorobogatiy, "Thin chalcogenide capillaries as efficient waveguides from mid-IR to THz," *J. Opt. Soc. Am. B*, vol. 29, pp. 2116-2123 (2012)

Conference proceedings:

1. **B. Ung** and M. Skorobogatiy, "Chalcogenide Microporous Fibers for Nonlinear Applications in Mid-Infrared," in *Proc. of CLEO*, San Jose, CA, (May 2010)
2. **B. Ung**, A Dupuis, and M. Skorobogatiy, "High refractive index titania-doped polymers for THz hollow Bragg fibers: how absorption losses limit the index contrast," in *Proc. of IRMMW-THz Conf.*, Rome, Italy (Sept. 2010)
3. **B. Ung** and M. Skorobogatiy, "Giant nonlinear optical enhancement in chalcogenide glass fibers with deep-subwavelength metallic nanowires," in *Proc. of CLEO*, Baltimore, MD, (May 2011)
4. **B. Ung**, M. Rozé, A. Mazhorova, M. Walther, and M. Skorobogatiy, "Suspended core polymer fibers with isolated mode for terahertz guiding," in *Proc. of CLEO*, Baltimore, MD, (May 2011)
5. **B. Ung** and M. Skorobogatiy, "Extreme nonlinear optical enhancement in chalcogenide glass fibers with deep-subwavelength metallic nanowires," in *CIPI Annual Meeting*, Ottawa, ON, (May 2011)
6. **B. Ung**, M. Rozé, A. Mazhorova, M. Walther, and M. Skorobogatiy, "Suspended core subwavelength fibers for practical low-loss terahertz guidance," in *Proc. of OSA Advanced Photonics Congress*, Toronto, Canada, (June 2011)
7. **B. Ung** and M. Skorobogatiy, "Chromatic dispersion engineering in chalcogenide microporous fibers for the middle-infrared," in *Proc. of OSA Advanced Photonics Congress*, Toronto, Canada (June 2011)
8. **B. Ung**, and M. Skorobogatiy, "Design and fabrication of photonic crystal and plasmonic waveguides for bio and chemical sensing; applications from the visible to THz spectral range," in *Proc. of OSA Frontiers in Optics*, San Jose, CA (Oct. 2011)
9. **B. Ung**, H. Qu, and M. Skorobogatiy, "Photonic bandgap fiber bundle spectrometer," in *Proc. of CLEO,* San Jose, CA, (May 7, 2012)

APPENDIX B : PRINCIPLES OF THE FINITE-ELEMENT METHOD

All of the microstructured fibers investigated in this thesis were at some point analyzed using the finite-element method (FEM). We here review the basic principles underlining this numerical method.

Guided modes of optical waveguides, including microstructured fibers, are governed by the time-independant Helmholtz equation, here written in terms of the *H* magnetic field component:

$$\nabla \times \left(\frac{1}{\varepsilon(x,y)} \nabla \times \mathbf{H} \right) = \left(\tilde{N}_{\text{eff}} \frac{\omega}{c} \right)^2 \mathbf{H} \qquad \text{(B.1)}$$

where a $e^{-i\omega t}$ time dependance was assumed and $\tilde{N}_{\text{eff}}$ stands for the complex effective refractive index ($\tilde{N}_{\text{eff}} = n_{\text{eff}} + i\alpha\, c/2\omega$) of a particular mode at a given frequency $\omega = 2\pi\nu$.

The premise of the finite-element method is to discretize the computational space into a set of finite geometrical elements (i.e. regular or irregular triangles) – which the interconnection creates a *mesh* – and approximate the unknown field inside each element using polynomial basis functions of order *n*. Most commercial FEM-based mode solvers such as RSoft FemSIM® and COMSOL Multiphysics® use 2nd-order ($n = 2$) polynomials for the basis functions. If more accuracy is needed or when the waveguide supports regions of rapidly varying field amplitude, it is advised to use higher-order polynomials. As a general rule, the numerical dispersion (i.e. the numerical error associated with the evaluation of the wavevector $\beta = k_0 n_{\text{eff}}$) of finite-element schemes utilizing a two-dimensional mesh exhibits the following trend [269] :

$$Error(n_{\text{eff}}) \sim \left(\frac{h}{\lambda} \right)^{n+1} \qquad \text{(B.2)}$$

where *h* denotes the shortest distance between nodes, and *nh* corresponds to the length of the shortest element side with *n* representing the polynomial order and λ denoting the light wavelength. Therefore, it is important when conducting finite-element calculations (or any numerical simulations for that matter) to make sure that the code converges asymptotically towards a given value. An example of such convergence study is shown in Fig. B. 1 where the fundamental mode's real effective index (n_{eff}) is plotted as a function of the inverse discrete element size (h^{-1}) with polynomial order $n = 2$ and for a given microporous chalcogenide fiber

geometry at $\lambda = 10.5\ \mu m$ [see Chapter 2.1]. One observes in Fig. B. 1 that n_{eff} converges towards a value close to $n_{eff}^{max} \approx 1.818$.

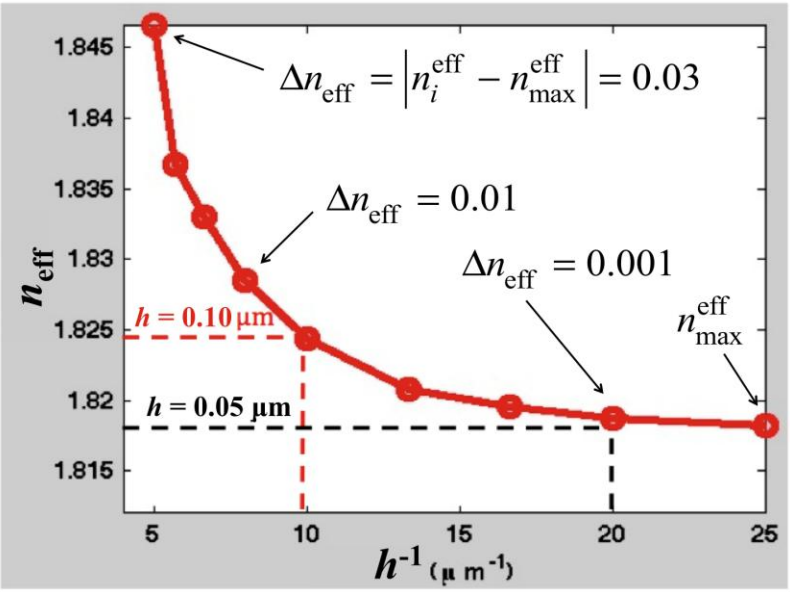

Figure B. 1 Convergence study for the fundamental mode guided in a specific microporous chalcogenide fiber geometry at $\lambda = 10.5\ \mu m$ and for polynomial order $n = 2$. FEM calculations conducted with RSoft FemSIM® software.

If we assume the best estimate (n_{eff}^{max}) as the reference value and rewrite Eq. (B.2) to read $Error(n_{eff} - n_{eff}^{max}) \sim (h/\lambda)^{n+1}$ and take the logarithm $\log\{Error(n_{eff} - n_{eff}^{max})\} \sim (n+1) \cdot \log\{h/\lambda\}$, we can then make a log-log plot to find the rate of convergence (η) which should be approximately equal to $\eta \sim (n+1)$. In the example of Fig. B. 1 the calculated rate was $\eta \approx 2.47$, thus slightly lower than the theoretical rate of $(n+1) = 3$.

Another important aspect in the implementation of FEM simulations is that the discretization mesh must conform and approximate the structure to be modeled as closely as possible. In this respect, it might be useful to exploit some symmetries (e.g. rotational) in the structure's geometry, which on the one hand can enhance the mesh's conformity, and/or on the other hand, help to reduce the number of discrete elements needed to attain a given level of accuracy. As an example, we show below in Fig. B. 2 the triangular mesh generated by the COMSOL Multiphysics® software to model the hybrid chalco-metallic nanofibers [see Chapter 2.2] at various zoom scales.

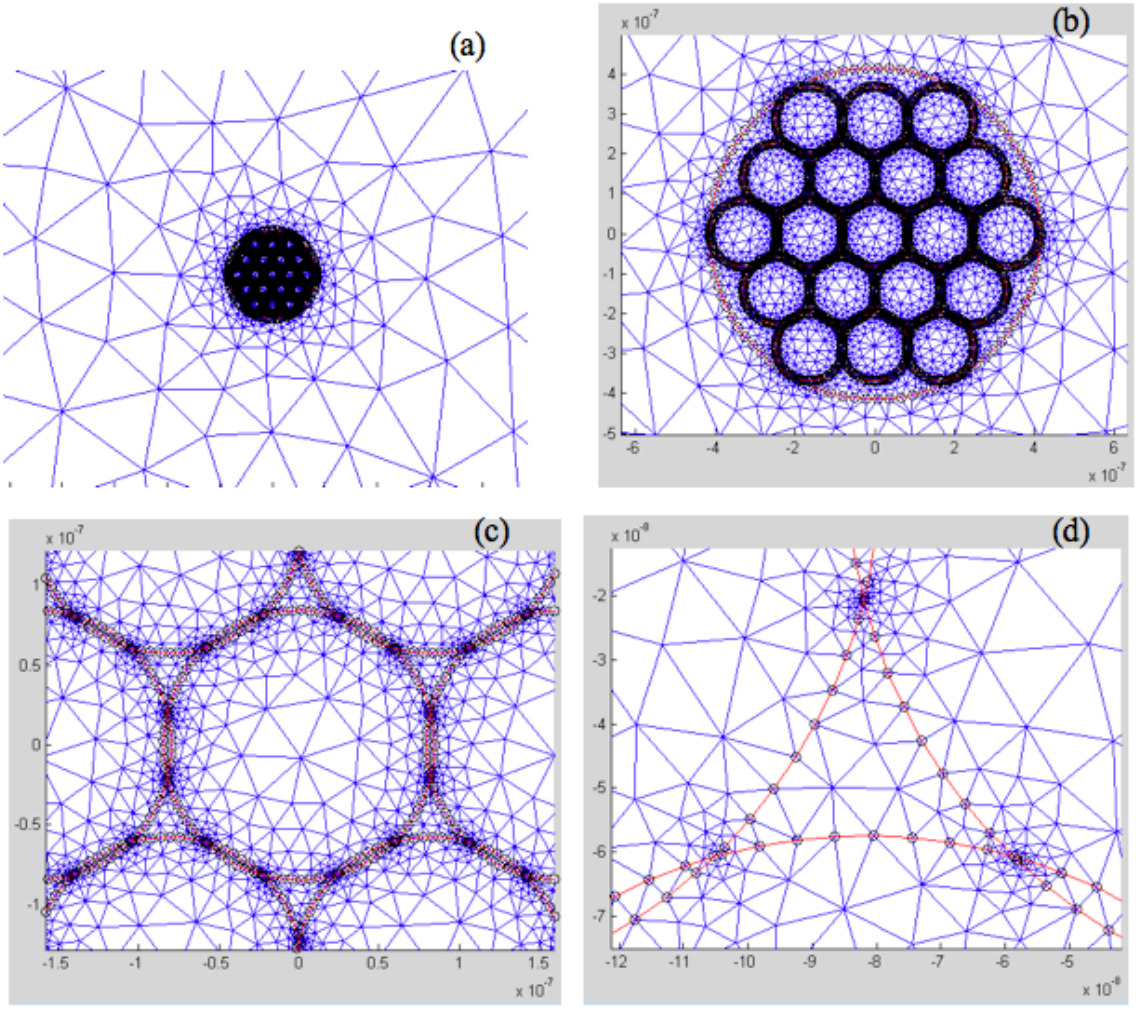

Figure B. 2 Triangular mesh generated by COMSOL® at different zoom scales, starting from farthest (a) to closest (d), for modelling a hybrid chalco-metallic nanofiber [see Chapter 2.2].

In the example mesh of Fig. B. 2, we observe that coarser elements are used in regions with the fewest objects, and so basically empty space. While the density of discrete elements increases as the size of objects decrease and the number of details increase. In this case, we remark that the finest mesh is located in the vicinity of the sharp apexes [Fig. B. 2(d)] of the deltoid-shaped objects. For that particular nanostructured optical fiber, it was important that the sharp apexes be well resolved since it is precisely at this location where the highest field intensities are produced as shown in the computed modal fields in Fig. B. 3(b). Because of the highly varying field intensities in the simulation, it was also important to choose a higher-order ($n = 3$) polynomial for the basis functions.

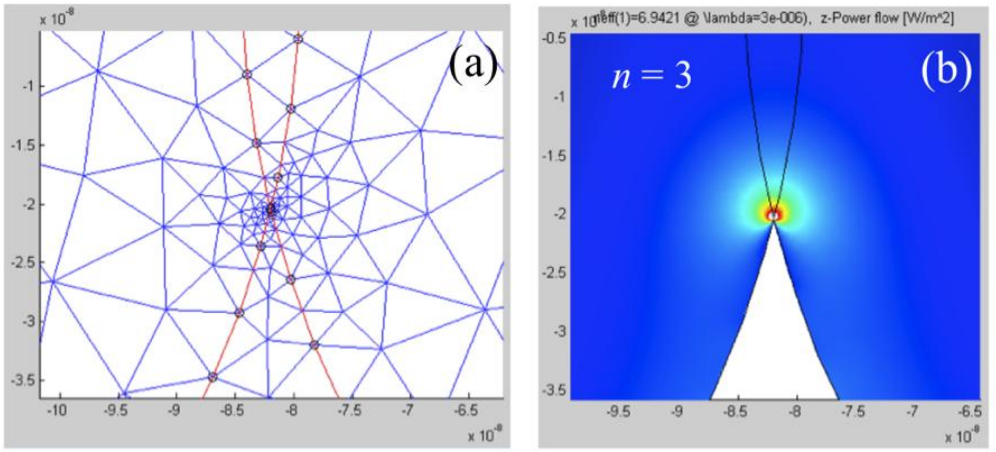

Figure B. 3 (a) Partial zoom image of the mesh generated by COMSOL® and (b) corresponding partial image of the fundamental mode in the hybrid chalco-metallic nanofiber at $\lambda = 3.0$ μm and for polynomial order $n = 3$.

We also note that the usage of *perfectly matched layers* (PML) – which act as artificial absorbing boundary conditions surrounding the main computational window – can help to eliminate the spurrious solutions that are often generated by numerical mode solvers [270].

APPENDIX C : PRINCIPLES OF THE SPLIT-STEP FOURIER METHOD

The nonlinear propagation of optical pulses in optical fibers is modeled by the nonlinear Schrodinger equation (NLSE) which is a nonlinear partial differential equation:

$$(T_{\mathrm{FWHM}} \geq 100 \text{ fs}): \quad \frac{\partial A}{\partial z} + \underbrace{\left[\frac{\alpha}{2} - i\sum_{m\geq 2}\frac{i^m \beta_m}{m!}\frac{\partial^m}{\partial t^m}\right]}_{\text{Linear operator: } \hat{D}} A = i\gamma \underbrace{\left[|A|^2 + \frac{i}{\omega_0}\frac{\partial}{\partial t}\left(|A|^2\right) - T_R \frac{\partial |A|^2}{\partial t}\right]}_{\text{Nonlinear operator: } \hat{N}} A \qquad \text{(C.1)}$$

There are very few analytical solutions to the NLSE, mostly obtained via the *inverse scattering method* [271], and which are valid for very specific cases. Arguably one of the most famous solution obtained in this fashion is for the *bright soliton* which assumes input pulses of hyperbolic secant waveform propagating in an anomalous dispersive optical fiber [272]. However for most practical cases, a numerical evaluation of the NLSE is necessary. The split-step Fourier method (SSFM) is a pseudospectral method that hinges on the separation and the consecutive numerical evaluation of the *linear contribution* (e.g. chromatic dispersion and losses) and the *nonlinear contribution* (e.g. Raman scattering, self-steepening, TPA, etc.) in the NLSE [273].

We rewrite the NLSE of Eq.(C.1) in the following functional form, where the linear and nonlinear contributions are respectively represented by the operators $\hat{D}$ and $\hat{N}$:

$$\frac{\partial A}{\partial z} = \left[-\hat{D} + \hat{N}\right] A \qquad \text{(C.2)}$$

The definition of the operators $\hat{D}$ and $\hat{N}$ can be easily inferred from inspection of Eq.(C.1) and Eq.(C.2). The main assumption of the SSFM is that in propagating from z to a small distance $z+h$ along the fiber, the linear and nonlinear contributions can be taken to act independently. The symmetrized version of the SSFM (this scheme was used for the simulations in Chapters 2.1.5 and 2.1.6) is third-order accurate with the step size $O(h^3)$ and has the following mathematical description [4]:

$$A(z+h,T) \approx A(z,T)\cdot \exp\left(\frac{h}{2}\hat{D}\right)\cdot \exp\left(\int_z^{z+h} \hat{N}(z')\cdot dz'\right) \exp\left(\frac{h}{2}\hat{D}\right) \qquad \text{(C.3)}$$

To implement Eq.(C.3) in practice, one first apply the fast Fourier transform (FFT) to evaluate the linear $\hat{D}$ operator in the frequency domain for the first $h/2$ distance. Then the inverse FFT of

the resulting spectrum is computed so that the nonlinear $\hat{N}$ operator is evaluated in the time domain. Finally, the FFT of the resulting pulse temporal profile at the midpoint $(z+h/2)$ is computed so that the linear $\hat{D}$ operator is evaluated for the remaing $h/2$ distance. The latter procedure is schematically described in the Fig. C. 1 below.

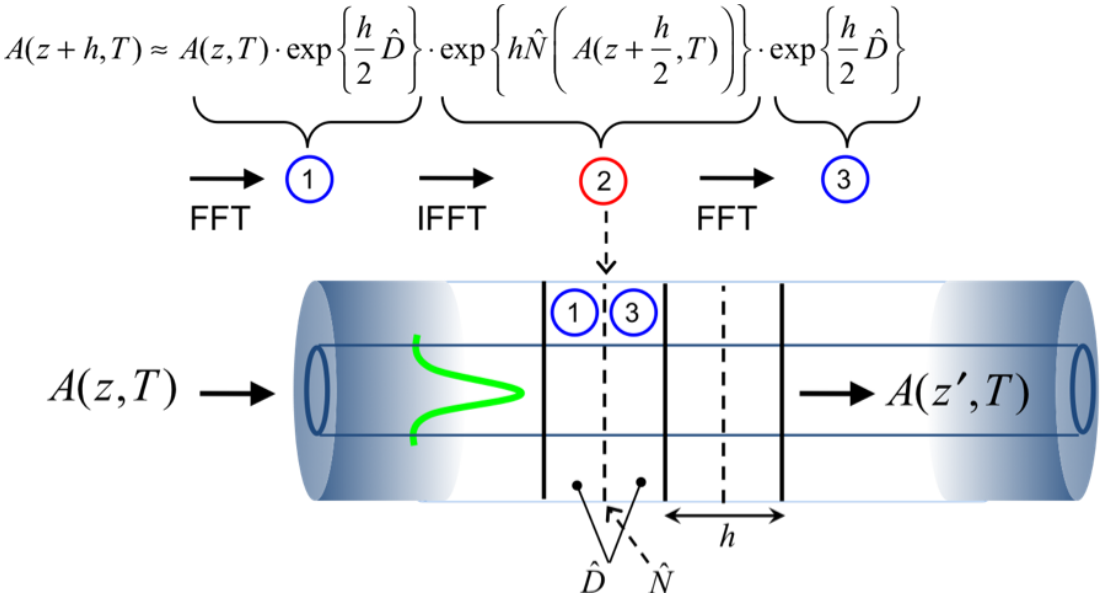

Figure C. 1 Schematic of the procedural implementation of the symmetrized split-step Fourier method.

In the symmetrized-SSFM, the nonlinear contributions are assumed to be lumped at the midpoint. For the successful application of the SSFM, it is critical to choose the proper step size (h). The step size must be much smaller than the characteristic length scales of the principal linear and nonlinear interactions in the fiber, hence the following inequalities: $h << L_{\mathrm{D}}$ and $h << L_{\mathrm{NL}}$ where L_{D} and L_{NL} denote respectively the *dispersion length* ($L_{\mathrm{D}} = T_0^2/|\beta_2|$) and the *nonlinear length* ($L_{\mathrm{NL}} = 1/(\gamma P_0)$) with $T_0 = T_{\mathrm{FWHM}}/(2\sqrt{\ln 2})$.

Moreover, the spectral computation window ($\delta\nu$) must be larger than the optical pulse bandwidth ($\nu_{\mathrm{FWHM}} \approx 0.44/T_{\mathrm{FWHM}}$ for transform-limited Gaussian pulses). As a rule of thumb, one typically selects a window at least ten times larger than the input pulse width: $\delta\nu \geq 10\,\nu_{\mathrm{FWHM}}$. However in the case of supercontinuum (SC) simulations, the spectral bandwidth of pulses can become so broad that the latter condition may not be sufficient. Therefore, one has to be careful when conducting SC simulations that the pulse spectral broadening does not reach the edges of

the computational window. Otherwise the periodic boundary conditions that are implicitly present in the SSFM will transfer the energy hitting one side of the computation window to re-enter the window from the opposite side. Additional detailed guidelines towards the optimization of SSFM-based simulations can be found in [274].

APPENDIX D : ERROR ANALYSIS OF THE CUTBACK TECHNIQUE

The *cutback method* is a destructive technique widely employed for measuring the propagation losses in microstructured optical fibers. Alternative non-destructrive techniques include the *directional coupler method* [136] and the *evanescent field tip-probing* [275]. The main advantage of the cutback method lies in its simplicity. As schematically pictured in Fig. D. 1, one basically proceeds to measure the total power (P_1) at the output end of the fiber of initial length L_1, then cuts a segment of the fiber and subsequently re-measure the output power (P_2) at the end of the fiber of length L_2. The latter procedure can be repeated several times to increase the statistical confidence of the measurements.

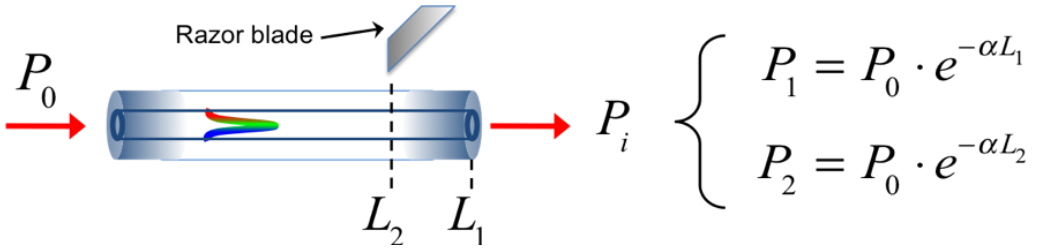

Figure D. 1 Schematic of the cutback technique procedure for measuring the optical propagation losses in an optical fiber.

The transmitted powers for each segment of the same fiber are written $P_1 = P_0 \cdot e^{-\alpha L_1}$ and $P_2 = P_0 \cdot e^{-\alpha L_2}$ where P_0 is the injected power and the shared unknown metric is the propagation loss coefficient (α). By writing the ratio of the output powers ($P_2/P_1 = P_0 \cdot e^{-\alpha L_2} / P_0 \cdot e^{-\alpha L_1}$) and taking the natural logarithm on both sides, we can then isolate the coefficient α to obtain the propagation losses in inverse centimeters (assuming that both L_1 and L_2 are expressed in cm):

$$\alpha(\text{cm}^{-1}) = \frac{\ln(P_2/P_1)}{(L_1 - L_2)} \quad , [\text{cm}^{-1}] \qquad \text{(D.1)}$$

Taking the base-10 logarithm in the above procedure instead of the natural logarithm yields the loss coefficient value in dB/m (where both L_1 and L_2 are expressed in meters):

$$\alpha(\text{dB/m}) = \frac{10 \cdot \log_{10}(P_2/P_1)}{(L_1 - L_2)} \quad , [\text{dB/m}] \qquad \text{(D.2)}$$

We note that a razor blade was used for cleaving the fibers in our measurements of the suspended core fibers [see Chapter 3.2.6], however we remark that other cleaving approaches exist (laser abalation, focussed ion beam milling, etc) that may result in better cleave reproducibility depending on the fiber's particular material composition and geometry. Along with cleave reproducibility, the re-alignment of the fiber (respective to the optical source axis) after each cleave, represent the most important source of experimental errors. Fully automated setups for fiber cleaving provides a means to achieve better cleave reliability and quality [263].

To understand the practical limitations of the cutback technique, it is insightful to track the propagation of experimental uncertainties in the calculated value of the propagation loss coefficient: $(\alpha \pm \Delta\alpha)$ where $\Delta\alpha$ denotes the absolute standard uncertainty of the measurement. Experimental uncertainties arise in the measured optical powers $P_1 \pm \Delta P$ and $P_2 \pm \Delta P$ and in the measured fiber lengths $L_1 \pm \Delta L$ and $L_2 \pm \Delta L$. We combine these standard uncertainties via the *root-sum-square method* by assuming that ΔP and ΔL are uncorrelated (i.e. statistically independent) to find the relative uncertainty of the loss coefficient value:

$$\frac{\Delta\alpha}{\alpha} = \sqrt{\left(\frac{\frac{\Delta P'}{(P_2/P_1)}}{\ln(P_2/P_1)} \right)^2 + \left(\frac{\Delta L'}{L_1 - L_2} \right)^2} \qquad \text{(D.3)}$$

where we used the following definitions for the respective uncertainties of the output powers and fiber lengths involved:

$$\frac{\Delta P'}{(P_2/P_1)} = \sqrt{\left(\frac{\Delta P}{P_1} \right)^2 + \left(\frac{\Delta P}{P_2} \right)^2} \qquad \text{(D.4a)}$$

$$\Delta L' = \sqrt{(\Delta L)^2 + (\Delta L)^2} \qquad \text{(D.4b)}$$

By inspecting Eq.(D.3) we first note that for output powers with close values we obtain a P_2/P_1 ratio close to one, which yields a logarithm near zero and thus a very large relative uncertainty $(\Delta\alpha/\alpha)$. The latter situation was obtained for the suspended small solid core fiber [see Chapter 3.2.6] where for some frequencies the losses were so low that the ratio of output powers were close to unity. Another interesting case that we encountered was for the suspended large porous core fibers in which the absorption is strong so that the measured output powers (P_1 and P_2) were

small, and consequently, the relative uncertainty in Eq.(D.4a) became large due to the large ratios $(\Delta P/P_1)$ and $(\Delta P/P_2)$. The latter situation can also be described as a case of low signal-to-noise ratio. Finally, we note that the relative uncertainty $(\Delta\alpha/\alpha)$ in Eq.(D.3) also depends on the contrast of fiber lengths used $L_1 - L_2$. The larger this contrast, the better the loss measurement's accuracy. Therefore it is advised to use long fiber lengths in the cutback technique in order to accumulate enough propagation losses so that the ratio P_2/P_1 becomes far from unity, and in order to have a small $\Delta L'/(L_1 - L_2)$ ratio in Eq.(D.3).